DEVELOPMENT OF A PROTOTYPE MANUFACTURING PROCESS FOR RELIABLE OPTICAL-FIBER BASED NEURAL PROBES

A Dissertation

Presented to

The Faculty of the Department of Electrical and Computer Engineering

University of Houston

In Partial Fulfillment

of the Requirements for the Degree

Doctor of Philosophy

in Electrical Engineering

by

Apeksha Awale

December 2015

DEVELOPMENT OF A PROTOTYPE MANUFACTURING PROCESS FOR RELIABLE OPTICAL-FIBER BASED NEURAL PROBES

Apeksha Awale

Approved:

Chair of the Committee
John C. Wolfe, Professor,
Electrical and Computer Engineering

Committee Members:

Wei-Chuan Shih, Associate Professor,
Electrical and Computer Engineering

John Miller, Professor,
Department of Physics

Wanda Zagozdzon-Wosik, Associate Professor,
Electrical and Computer Engineering

Valentin Dragoi, Professor,
Neurobiology and Anatomy, UT Medical School

Suresh K. Khator, Associate Dean,
Cullen College of Engineering

Badrinath Roysam, Professor and Chair,
Electrical and Computer Engineering

Acknowledgements

I am grateful to my advisor, Dr. John Wolfe for his continuous motivation and generous support at every stage of the degree program. His exemplary enthusiasm and dedication towards research is admirable. I would like to thank Dr. Shih for being an excellent and inspirational guide, and Dr. Purushothaman for his successful efforts and time during in vivo experiments. I would like to thank the members on my dissertation committee – Dr. Wosik, Dr. Miller and Dr. Dragoi for providing valuable insights throughout this dissertation. I am thankful to Michael Young at the ECE machine for providing all the machined parts for tool and process development. I would also like to thank Dr. Mauger at Nanostructures Inc. for providing us with the stencil masks used in probe fabrication. The advancements in the project would not have been possible without the funding sources – NIH, ANH, TcSUH and Cullen Foundation.

I have gained a fascinating amount of knowledge at every step from my lab and life mentors and friends – Pratik Motwani, Mufaddal Gheewala, Sumit Abhichandani and Shreyasee Das, and outstanding support from my colleagues – Rebecca Kusko and Tamanna Afrin Tisa. This journey was made enjoyable by my highly tolerant roommates/friends – Shweta Kakad, Amrita Dhar and Titiksha Vats, Houston family of friends – Pratik Motwani, Rohan Matkari, Mutiara Sari Ayu, Anil Dak, Arun Iyer, and many more to pen down. I dedicate this dissertation to my most loving parents, Santosh Awale and Suvarna Awale, my little brother, Atharva Awale and Almighty God – I would not have completed this experience without either of them.

DEVELOPMENT OF A PROTOTYPE MANUFACTURING PROCESS FOR RELIABLE OPTICAL-FIBER BASED NEURAL PROBES

An Abstract

of a

Dissertation

Presented to

The Faculty of the Department of Electrical and Computer Engineering

University of Houston

In Partial Fulfillment

of the Requirements for the Degree

Doctor of Philosophy

in Electrical Engineering

by

Apeksha Awale

December 2015

Abstract

The function of a neuron depends on its microcircuitry – the inputs it receives from local and long-range connections and the outputs it sends to other neurons. Mapping these connections is typically done by stimulating a population of neurons chemically, electrically, or optically, and recording the induced extracellular action potentials with implanted metallic probes. The probes may be cylindrical needles or thin planar blades. The needles have an advantage for deep structures since their circular cross-section minimizes friction, hence insertion force, while planar probes provide much greater design flexibility at low cost by leveraging semiconductor manufacturing technology. In this thesis, we explore the possibility of manufacturing cylindrical probes with dense thin film electrode patterns on fine optical fibers, thus, providing the design flexibility of planar probes in the cylindrical format required for deep brain applications.

Our group reported the fabrication of cylindrical probes with 4-integrated electrodes on 60 μm optical fibers at EIPBN-2013. These proof-of-concept *optrodes* were used to detect photo-simulated electrical activity of neurons in the primary visual cortex of *Olemur garnettii*, a non-prosimian primate. However, processing times were unacceptably long, about 1 month for a batch of 4 probes, and all experienced short-term electrode failure in cerebro-spinal fluid through insulator delamination, which remains a major obstacle to long-term viability of many state-of-the-art probe technologies.

In this thesis we report optimized processes that reduce the time and increase batch size for fabricating 4-channel optrodes that result in a projected processing time of 80 minutes for a batch of 16 probes-about 5 minutes/probe. Our most important achievement was the development of a rugged, pin-hole free dielectric coating with stable

impedance in phosphate-buffered saline over a period of 10 days under moderate ($6mA/cm^2$) electrical stimulation at frequencies from 200-10,000 Hz. Electrode impedance on a 60 µm fiber was unchanged after 6 repeated insertions to a depth of 3.8 cm in agar gel (Landor Trading Company), which simulates the consistency of brain tissue. Scanning electron microscopy showed that scratching was absent on probes that had been inserted to a depth of 3.8 cm in 75 µm and 438 µm stainless steel *canulae*.

TABLE OF CONTENTS

List of Figures

List of Tables

Chapter 1 - Introduction

1.1 – Motivation

What we call the mind is a set of operations carried out by the brain, from simple motor behaviors to complex cognitive actions. The mammalian brain is beyond compare in its complexity, given that it is an intricate network of millions of interconnected neurons carrying out these operations. The brain integrates information generated by sensory organs with the help of these neurons, cells that process the inputs they receive from local and long-range connections and send outputs to other neurons. The task of neural science is to explain how the brain marshals its millions of individual nerve cells (neurons) to produce behavior influenced by the environment. Understanding exactly how the brain enables the human body to record, process, store and retrieve vast quantities of information[1], requires mapping of these neural circuits which is typically done by stimulating a population of neurons chemically, electrically or optically. Such stimulation of neurons produces a functional response by depolarizing the cell's membrane potential, which can be recorded using an array of electrical sensors to form a dynamic picture of the brain. This picture shows the interactions between individual cells in both time and space.

Consider, for example one of the most complex neural circuits – the limbic system which is a cortical representation of feeling. Fig. 1-1 from ref. 2 shows the limbic lobe and the deep lying structures. Since the hypothalamus communicated reciprocally with areas of the cerebral cortex, information about the conscious and peripheral aspects

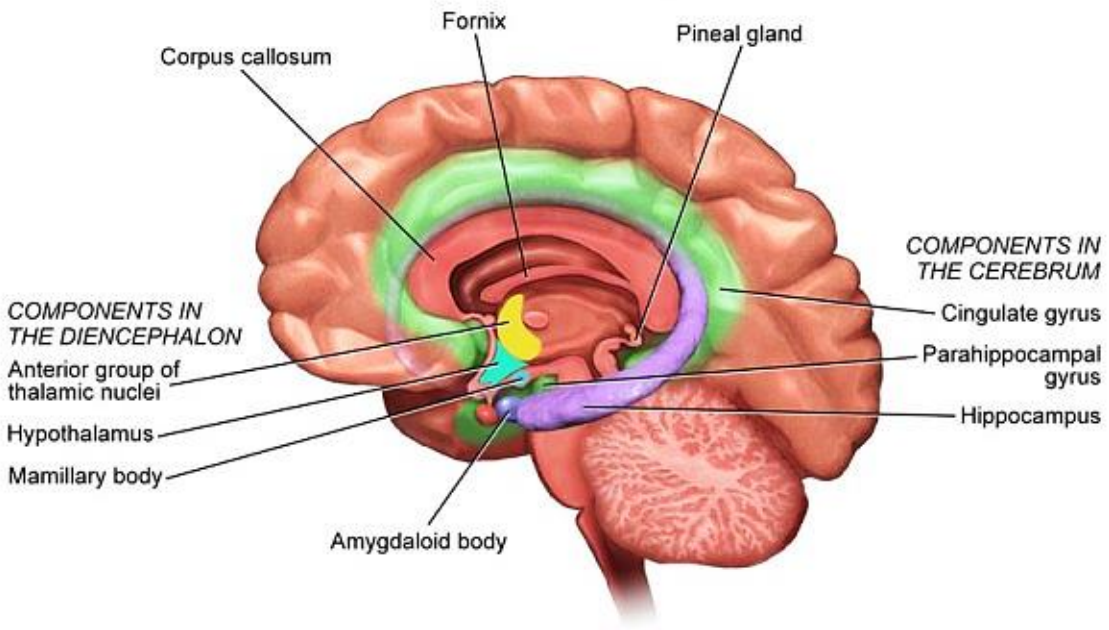

Fig. 1-1: Complex circuitry of the limbic system

of emotion affect each other[3]. The neocortex – the part of the cerebral cortex concerned with sight and hearing in animals – influences the hypothalamus by means of connections to the cingulate gyrus and from the cingulate gyrus to the hippocampal formation. Information from the cingulate gyrus is carried by the fornix – the fiber bundle responsible for carrying the outflow of the hippocampus – to the mammillary bodies of the hypothalamus. In turn, the hypothalamus provides information to the cingulate gyrus by a pathway from the mammillary bodies to the anterior thalamic nuclei. It was discovered further[4], that stimulation of the amygdala produced a major dramatic syndrome in animals and that the amygdaloid body is partly responsible for coordinating the activity of the hypothalamus. Thus, emotionally significant stimuli activate sensory pathways that trigger the hypothalamus to modulate parameters like heart rate, blood pressure, and anxiety.

To understand a circuit this complex, the existence of synaptic connections between neurons needs to be inferred. This connectivity is often interpreted using *in vivo* experiments by electrically or chemically stimulating a cluster of neurons and observing the effect on potential target neurons. Moreover, neurons receive inputs from the same source region via multiple pathways. Going back to the limbic system,[5] the hypothalamus receives inputs from the cortex via hippocampal formation and the amygdala along with a feedback from the cingulate gyrus, as seen in Fig. 1-2. To determine the direct influence

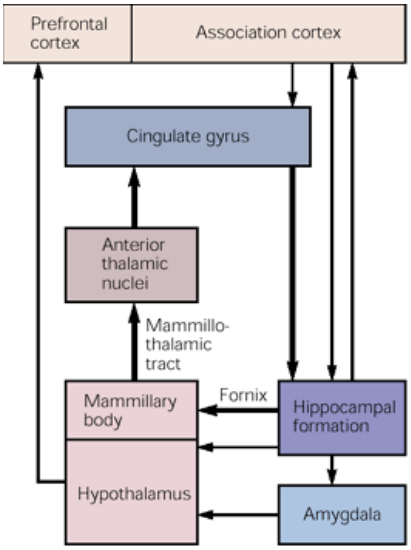

Fig. 1-2. Block diagram of one circuit in the limbic system.

exerted by the hippocampus on hypothalamus, one cannot simply electrically or chemically stimulate the hippocampus and measure the effect on the hypothalamus as this would include both the direct as well as the indirect influence via the cingulate gyrus. Thus, a technique to achieve cellular specificity is required in order to study these individual neural pathways.

Connectivity is often inferred during *in vivo* experiments by electrically or chemically stimulating a set of neurons and observing the effect on potential target neurons. However, as seen from Fig. 1-3 from ref. 6, electrical stimulation does not provide the required selectively given that it affects all nearby neurons and passing axons indiscriminately. Thus, it is not useful for interpreting individual neural circuits. However, a new technique, optogenetics,[6,7] combines genetics and optics in order to seamlessly stimulate or silence specific nerve cells, as shown in Fig. 1-3.

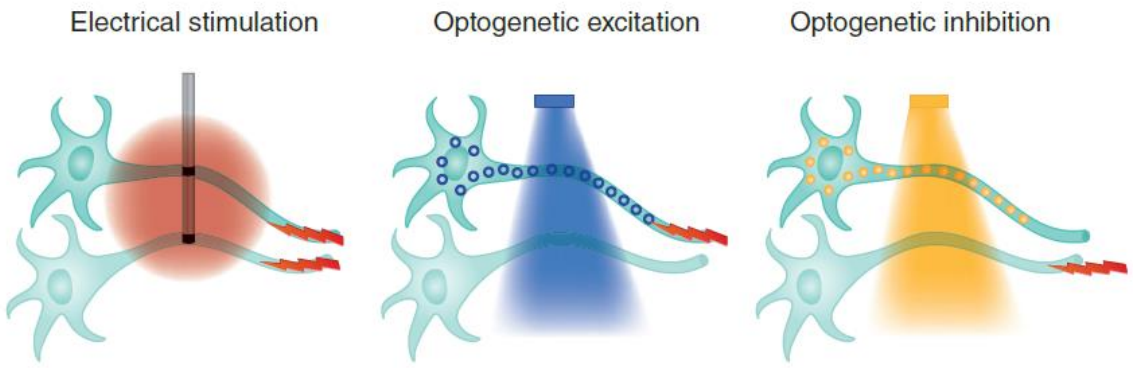

Fig. 1-3: Principle of optogenetics in neuroscience. Targeted excitation (blue) or inhibition (yellow), conferring cellular specificity.

It enables probing of specific cells which have been genetically sensitized to light, while leaving all other cells unaffected. Information in the brain flows via excitatory neurons that have properties depending on their anatomical location. Since this excitation cannot go on forever, the brain has a mechanism to keep this excitation in check and make sure it stops when required. This is known an inhibition performed by inhibitory neurons. If, by using gene therapy,[7] light sensory molecules can be selectively inserted into just the excitatory, then illuminating that portion of the brain with light causes only excitatory neurons to spike. Since the inhibitory neurons are not stimulated at all, the

activity controlled by those excitatory neurons continues till the end of the light pulse. Thus in the case of the limbic system, the undesired indirect path could be blocked when the hippocampus is stimulated *optically*. Along with decoding the brain circuitry, this approach can be extended to reduce the symptoms of a number of neurological diseases ranging from the involuntary muscle movement seen in Parkinson's disease, essential tremor, dystopia and chronic pain.

Intracellular recordings include whole-cell, patch recording techniques or *in vivo*, wherein the latter is very challenging and impractical, especially when recording from freely moving animals. Extracellular recordings carried out with the help of microelectrodes implanted in close proximity to the target neurons identify the activity from a single neuron (single-unit) or a set of multiple neurons (multi-unit). Such neural recordings hold promise in research of brain-machine interfaces where raw neuronal signals can be translated into motor commands to reproduce arm reaching or fist grasping movements in paralyzed subjects.[8, 9]

Electrophysiology has traditionally been the standard for neuronal recordings and the preferred electric probe are the twisted wire tetrodes formed by twisting 4 wires together, fusing the insulation and clipping off the ends. They allow us to record unit activity by sorting spikes from different neurons depending on their position with respect to the electrode. In order to maintain a reasonable signal-to-noise ratio, the tetrode technology requires electroplating the ends of the cut wires with gold as shown in Fig. 1-4. These ends, however, are extremely fragile and the plated gold can be easily broken off by merely touching it with a paper towel. This highly compromises the reliability of the tetrodes during insertion or withdrawal while using a guide tube. The technology cannot

accommodate multi-sensing tetrode sites or an optical channel for optical stimulation. Thus, the TWTs exhibit fundamental shortcomings in terms of reliability and manufacturing repeatability that one would expect an advanced probe with added functionality to possess.

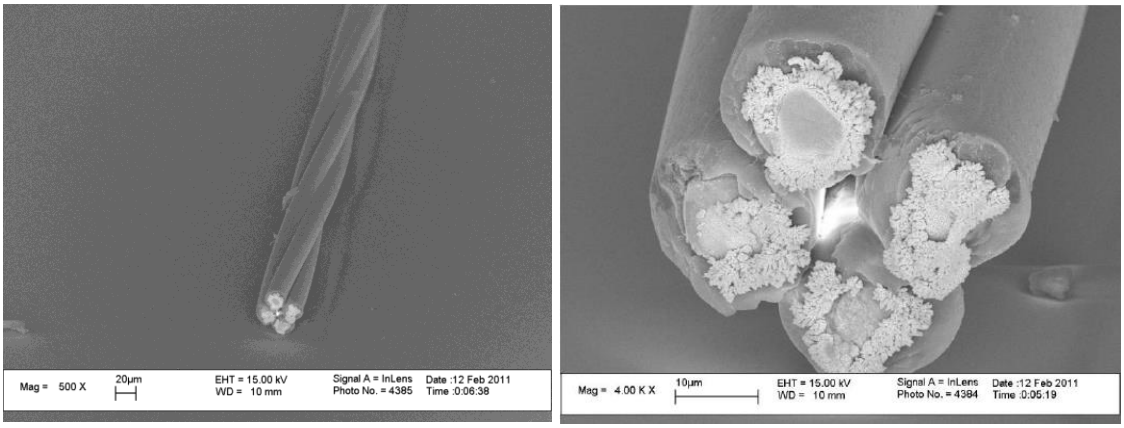

Fig. 1-4: Four wired twisted to form a tetrode with electroplated gold contacts at the tip.

In 2011, Mechler and Victor[10] established the design specifications of a probe that allows high precision 3-D mapping and accurate localization of neuronal dipoles. They demonstrated that by advancing a tetrode with ~40µm contact separation in steps on 5-10 µm through cortical layers, a single neuron's location could be estimated within a sphere of radius ~50µm. Thus, it will require 6 tiers of 4-channel integrated sensors (tetrodes) with overlapping recording fields and each tier is just 10µm away from the adjacent one to provide this overlap with electrode sites less than 5µm.[11] "Lead fields" play a very important role in understanding probe performance at a conceptual level. Dipole optimization comprises of a linear component which can be framed in terms of a "lead field matrix" that summarizes the geometry and electrical properties of the tissue and

probe.[11] While this lead field gets distorted due to the wide variations in size, shape and separation of contacts in terms of the twisted wire tetrodes, this new conceptual design utilizes the lead matrix to solve localization problems.

We demonstrate an advanced probe technology with thin film electrical sensors integrated on optical fiber substrates. The fiber provides an integrated optical channel and the electrode geometry can be extended to multi-tiered configurations. By means of promising techniques and manufacturing reliability, it addresses the weaknesses of the twisted wire tetrodes.

1.2 – Objectives

The aim of this dissertation is to develop a reliable family of implantable probes that will give neuroscientists the power to record from a given set of neurons, accurately estimate the location and spiking activity with that volume and, when combined with optogenetics, safely manipulate the activity of a subset of these neurons in time and space. Electrode impedance will be used as a measure of electrode reliability. Sanchez[12] has characterized electrode failure in terms of abiotic and biotic processes and failure modes. Examples of abiotic processes are corrosion and insulation delamination which do not involve the foreign body encapsulation of the probe by the brain. Somewhat surprisingly *abiotic* mechanisms remain the problem in state-of-the-art probe technologies. One of the objectives of this dissertation is to develop a probe that has no *abiotic* failures.

Optical fibers as substrates provide the required flexibility for implantation and serve as a channel for multi-spectral lossless light delivery. The electrode geometry does

not significantly contribute to the probe diameter and high resolution processes make it possible to accommodate a higher electrode count on thin fibers. Our proof of concept electrodes were used to demonstrate the possibility of detecting photo-stimulated electrical activity of neurons in the primary visual cortex of *Otolemur Garnettii,* a non-prosimian primate. Inspite of these successful advancements, our probes were faced with two major weaknesses. One was the throughput because processing times were unacceptably long, about one month for a batch of four probes, and the other one was reliability where all the probes experienced short-term electrode failure in cerebro-spinal fluid through insulator delamination. This thesis aims at addressing these two concerns by developing optimized processes to speed up the process, and carrying out comprehensive analysis of *abiotic* failure mechanisms to eliminate them. Study of biotic is beyond the scope of this thesis. Higher reliability will, in turn increase the yield for the probes.

A high brightness lithography tool that is capable of handling large area exposures and the development of a more efficient etching tool will dramatically reduce the processing time. Design of innovative holders and probe-handling fixtures enables hassle-free and clean transport of probes. These improvements promise an increase in the number of probes that can be manufactured by the hour.

A number of methods for achieving the desired impedance value have been proposed – electrodeposition of microporous conducting polymers[13,14,15] and formation of nanoporous gold films using an alloying/de-alloying process,[16,17] instead of a smooth gold contact. We aim at carrying out some baseline, measurements in saline to create an initial characterization of our probe. As much as the initial characterized impedance is

crucial, maintaining the integrity of the probe while implantation and post implantation is important for the microelectrodes to be able to stimulate and sense neural activity reliably, over a period of week or two.[18] Abiotic-biotic characterization of microelectrode arrays have been reported[18,19] to study site changes and damage to the insulation layer. We intend to perform similar abiotic characterization – (1) Characterization using Scanning Electron Microscopy (SEM) images of probes to study any delamination or cracking effects during implantation in agar gel and *cannula*, (2) Effect of the implantation experiments on the impedance, and (3) Study the sustainability of the electrode impedance during and after extended periods of implantation in both saline and phosphate buffered saline maintained at normal body-temperature (37ºC).

Furthermore, our probes can accommodate dense electrode arrays at a very low cost by leveraging semiconductor manufacturing industry. They can be implanted in cortical surfaces as well as in deep brain regions, for which micro machined silicon probes are too short or buckle for implant depths greater than only 6-8 mm.

Chapter 2 – Neuroscience

2.1 – Nerve Cells and Behavior

The nervous system did not gain so much of a special attention until the late 1800s, when the first detailed descriptions of nerve cells were undertaken by Camillo Golgi and Santiago Ramón y Cajal. Using Golgi's staining technique they discovered that nervous tissue is a network of discrete cells and established much of the early evidence for the *neuron doctrine* – the principle that individual neurons are the elementary signaling elements of the nervous system. The human brain is estimated to be composed of an extraordinary number of these cells (of the order of 10^{11}), which can be classified into at least a thousand different types.[20]

A typical neuron is divided into four morphological regions (Fig. 2-1 from ref. 21): the cell body (*soma*), dendrites (input terminals), the axon (conducting unit) and the presynaptic (output) terminals. The *soma* contains the nucleus that stores the genes of the cell and synthesizes the proteins of the cell. Several short *dendrites* branch out in a tree-like fashion from one end of the cell body and receive incoming signals from other nerve cells. One, long tubular axon extends away from the cell body and is the main conducting unit for carrying signals to other neurons ranging from 0.1 mm to 3 m and 0.2 μm to 20 μm in diameter. The cell's conducting signals, called action potentials are rapid, all-or-none nerve impulses that are triggered when the integrated inputs of the dendrites exceeds a well-defined threshold. Actions potentials typically have amplitudes of 100 mV and durations of about 1 msec. They are initiated at a specialized trigger region at the origin of the axon called *axon hillock;* from there they are regenerated at regularly spaced

Nodes of Ranvier. The axons then branch out and carry the signals to neurons further down the neural pathway. The point of communication of two neurons is called a *synapse*; transmitting cell is called the presynaptic cell and the receiving cell is called the postsynaptic cell.

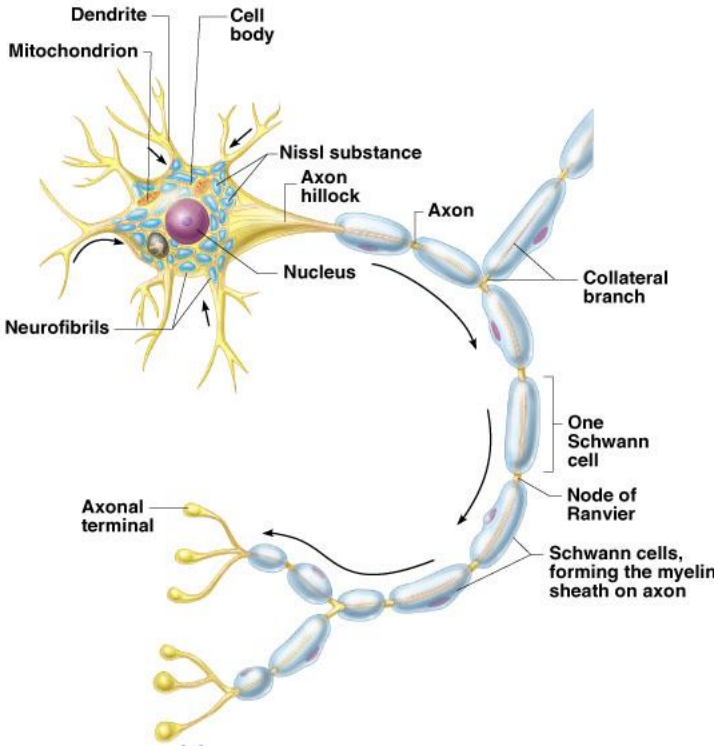

Fig. 2-1: Anatomy of a neuron.

At rest, a neuron maintains a difference in the electric potential on either side of the plasma membrane, knows as the *resting* membrane potential and typically ranges from -60 mV to -70 mV. This electrostatic potential inside the cell relative to the extracellular fluid, results from two factors: first is the out-diffusion of K^+ ions down their chemical concentration gradient. Due to this slight excess of K^+, the outside of the membrane accumulates a positive charge leaving a negative charge on the inside. This negative charge builds up until the outward movement of K^+ (driven by its concentration

gradient) is equal to the inward movement (driven by the electrical potential difference) [Fig. 2-2 from ref. 20]. This potential is the potassium equilibrium potential and for a cell only permeable to K^+, it is the resting membrane potential. The second mechanism is the Na^+ - K^+ pump, a large-membrane spanning protein that moves Na^+ and K^+ *against* their net electrochemical gradients: in each pumping cycle 3 Na^+ ions are pumped out of the cell and 2 K^+ ions are pumped into the cell. The energy for this transfer is provided by Adenosine triphosphate (ATP).

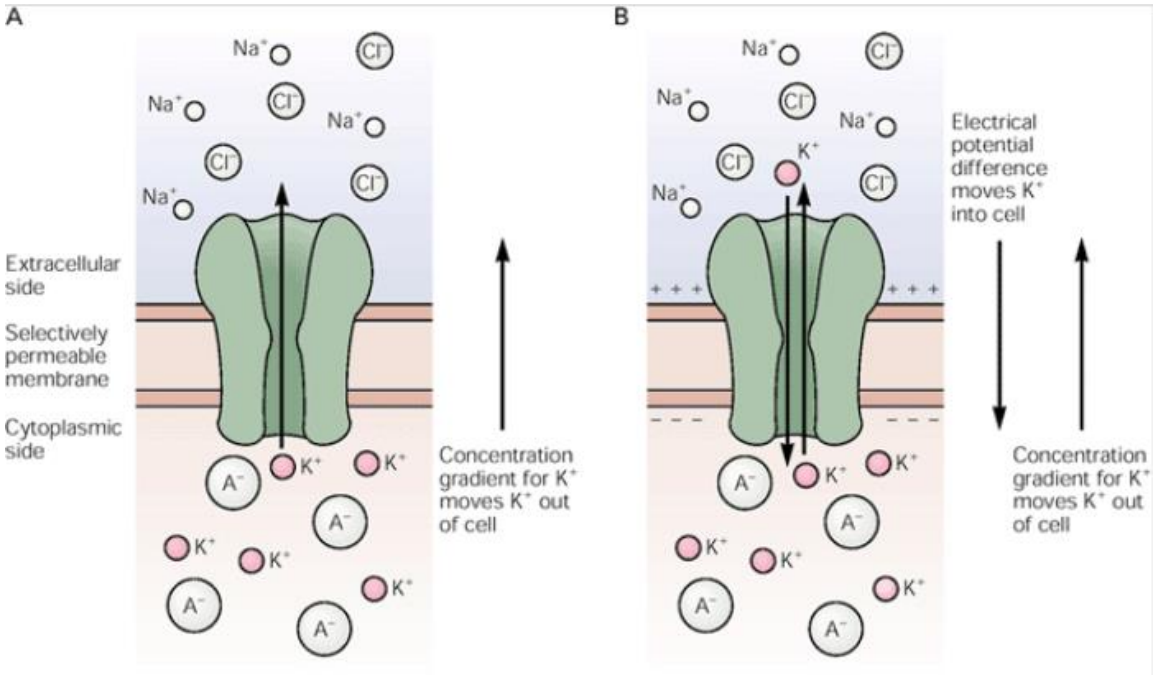

Fig. 2-2: The flux of K^+ across the membrane is determined by both the K^+ concentration gradient and electrical potential across the membrane.

Since there is current flow by both positively and negatively charged ions, essentially the direction of the flow is defined as the direction of *net* movement of *positive* charge. This net flow of cations and anions into and out of the cell disturbs the charge separation across the membrane. This change in the charge separation causes

depolarization (less negative membrane potential) or *hyperpolarization* (a more negative membrane potential). Hyperpolarizing responses and small depolarization events are passive responses, but when some depolarization events approach a critical value, called the *threshold*, the cell responds with an *action potential* or *spike*. Cole and Curtis[22] provided the first early evidence that action potential results from changes in the flux of ions through the ion gated channels in the membrane and this was further highlighted by Hodgkin and Katz[23] whose data proved that the rising phase of the action potential indicated Na^+ influx whereas the falling phase is due to later increase in K^+ permeability.

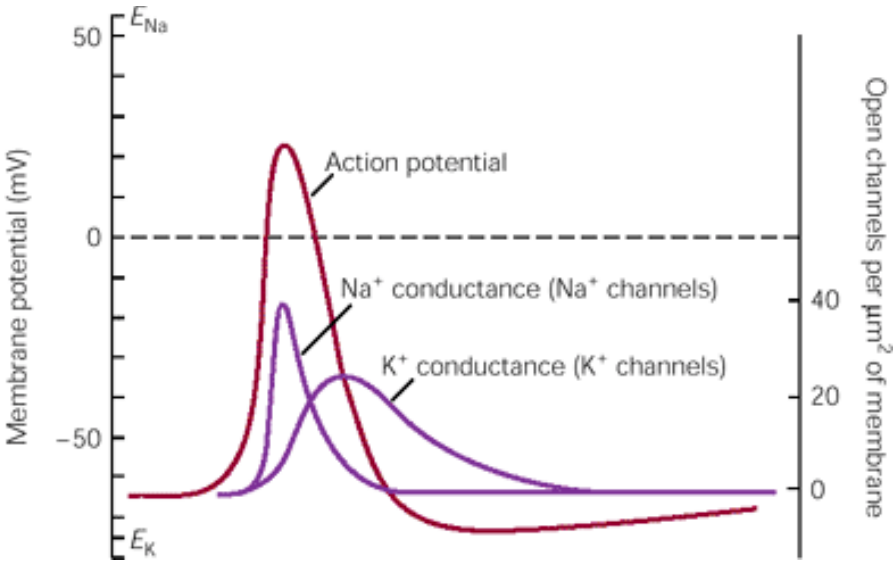

Fig. 2-3: The sequential opening of voltage-gates Na^+ and K^+ channels generate the action potential.

Later, Hodgkin-Huxley[24] proposed a model showing how the action potential (Fig. 2-3 from ref. 20) is generated by sequential opening of voltage-gated Na^+ and K^+ channels and the effect of the ionic components of the underlying conductance changes: A depolarization of the membrane causes Na^+ conductance to increase rapidly. This leads to

positive feedback thereby increasing the influx of Na^+ which eventually drives the membrane potential to the peak of the action potential. Subsequent opening of the K^+ channels causes an outward K^+ current that tends to re-polarize the membrane causes the falling phase of the action potential. The negative portion (*after-potential*) occurs because the K^+ channels that open during the later phase of the action potential close some time

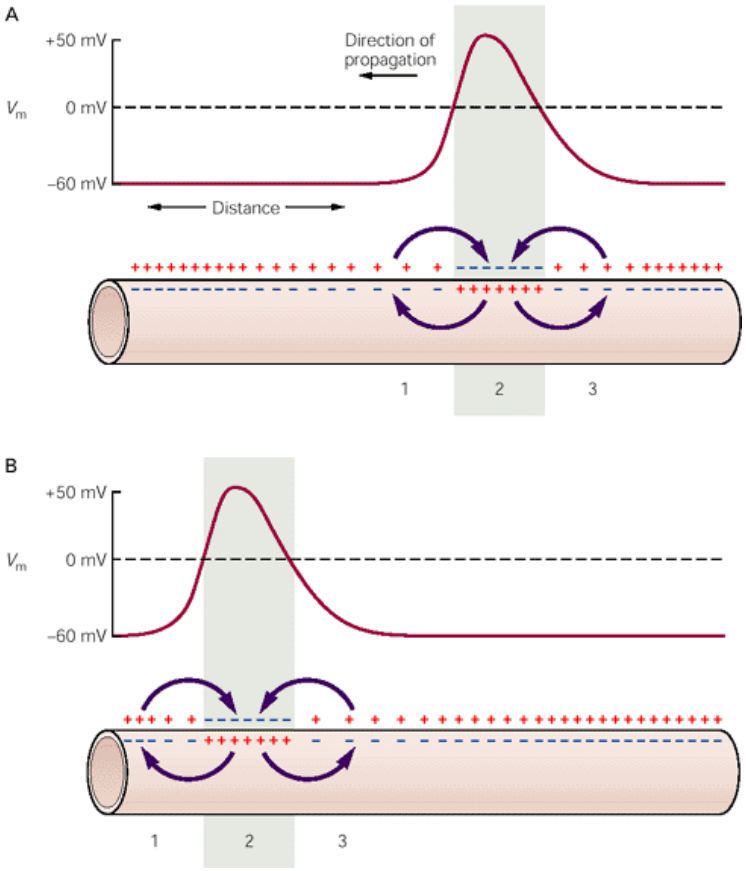

Fig. 2-4: Passive conduction of depolarization along the axon contributes to the propagation of the action potential.

after the membrane potential has returned to its resting value. The depolarization at any point along the axon causes a local imbalance in the ionic concentration gradients as shown in Fig 2-4 from ref. 20. This localized depolarization spreads passively by Na^+ diffusion along the axon in the region ahead as well as behind the action potential.

However, the region behind the action potential repolarizes due to the efflux of K^+ and thus the action potential can propagate in the forward direction only.

2.2 – Electrochemistry at the Electrode – Electrolyte Interface

The recording sites on a microelectrode come in contact with the cerebrospinal fluid during surgical implantation forming an electrode – electrolyte interface. This gives rise to a contact impedance at the interface which has a direct relationship with the total surface area of the interface. This impedance is an integral part of the recording mechanism and hence, it is important for us to understand the electrochemical phenomena occurring at this interface.

The average net charge in the lamina of an electrolyte is always zero according to the principle of electro neutrality, given that the positive and negative ion concentrations are equal. The time-averaged force vectors in all directions and at every point in the bulk of the electrolyte are the same. When a metal is placed inside an electrolyte, a potential is generated at the interface since the electrolyte is now terminated at a metallic surface as shown in Fig. 2-5. Helmholtz suggested that the potential difference lies between two layers of electrical charge of opposite polarity.[25] One layer is due to specific adsorption of ions at the metal interface, the locus of the centers of which is called the Inner Helmholtz plane (IHP). Just beyond this, inside the electrolyte is a layer of solvated ions which are attracted by the excess charge on the metal. The locus of the centers of these ions is called the outer Helmholtz plane (OHP). It is therefore believed that a 'double layer' of charge exists at the interface which essentially behaves as a parallel plate capacitor with an interface capacitance termed as C_{DL} given by

$$\frac{1}{C_{DL}} = \frac{1}{C_H} + \frac{1}{C_G}, \tag{1}$$

where C_H is the Helmholtz capacitance and C_G represents the Guoy-Chapman[57] capacitance.

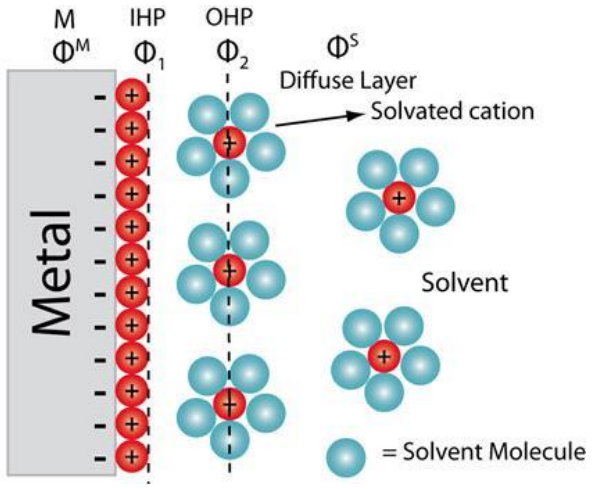

Fig. 2-5: Electrochemistry at the Electrode-Electrolyte interface.

However, this capacitance alone does not define the interface completely since like any other electrochemical layer some charge does manage to leak across the double layer. A resistive path is provided by a 'charge transfer' resistance for this leakage parallel to the interfacial capacitance, and is given by

$$R_{CT} = \frac{RT}{nFi_o}, \tag{2}$$

where R is the gas constant, T is the temperature, F is the Faraday constant, n is the number of electrons involved in the electrode reaction and i_o is the current density which defines the rate of electric charge flow. At high values of this exchange current density, the reactants from the solution are not able to diffuse as fast to the interface. This gives rise to diffusion impedance sending the reaction into what is called the diffusion

controlled regime. This diffusion, or 'Warburg' (named after Warburg, who in 1899, described this phenomenon) impedance is in series with the charge transfer resistance and both are generally considered to be in parallel with the double layer capacitance. The Warburg impedance is given by

$$|Z_W| = \frac{RT}{2zF^2c\sqrt{D}} \frac{1}{\sqrt{\omega}} , \tag{3}$$

where z is the valency of the ions, F is the Faraday's constant, c is the concentration of the ions, D is the diffusion coefficient from Fick's first law, R is the gas constant, T is the temperature and ω is the frequency of the electric field. The final component is the spreading resistance (R_{SP}) which is the resistance from the solution to the flow of charge from the localized electrode to a distant counter electrode. It is given by

$$R = \frac{\rho L}{A} , \tag{4}$$

where ρ is the specific resistance of the electrolyte, L is the length and A is the cross-section area of the electrolyte through which the current passes. So, from all this discussion, an equivalent circuit as shown in Fig. 2-6 can be deduced indicating the different elements of the impedance.

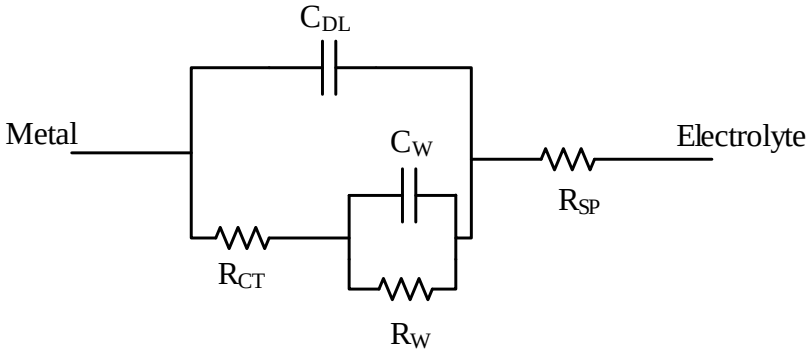

Fig. 2-6: Equivalent circuit for different components of impedance at the electrode-electrolyte interface.

2.3 – *In Vivo* Neural Stimulation and Recording

The foundations of experimental electrophysiology were laid in the 17th century represented by early findings of Jan Swammerdam who developed a neuromuscular preparation using needles attached to a frog's isolated leg muscles. He found that stimulation of the nerve caused contraction which could be monitored via the movement of needles, where in principle these needles could be used for contraction recording. The story of ion channels began in 1791, when Luigi Galvani published his fundamental work[26] identifying the relationship between the stimulus intensity and muscle contraction. These works were followed by many other brain implant experiments by Richard Carton, Gustav Fritsch and Eduard Hitzig. Thus began the study of electrophysiology of the nervous system and the neuroscience community realized the potential of electrically stimulating different areas of the brain and recording the induced electrical activity. Since neurons communicate with each other and the muscles through such electrical activity, an understanding of basic electrophysiology is fundamental to appreciating the functions and dysfunctions of neural systems.

Communication between neurons takes place through neurotransmitters released as a response to certain changes in the membrane potential. *In vivo* electrophysiology is a technique that involves the study of this communication by monitoring and controlling the change in the membrane potential with the help of electrical stimulation and recording electrodes. Electrical stimulation is carried out using monophasic capacitor-coupled or biphasic current pulses with zero net charge. Each pulse consists of an anodic phase and a cathodic phase, where the latter is reducing at the electrode where the current flows from the electrode to the tissue. Electrode corrosion and water electrolysis are

among common breakdowns which cause neural damage. To avoid these shortcomings, the stimulating electrode is required to have a scaled down geometry with high current density pulses.

We can see that electrical stimulation methods are the most common ways to stimulate neurons and record their activity, but the concern with these methods is lack of cellular specificity. What this implies is that some *distant* cells may be stimulated by an electrode merely by the influence of a stimulated axon in the vicinity of the electrode, whereas cells closer to the electrode may remain unaffected. Thus, it is difficult to target and control the functionality of distinct neuronal classes. An efficient technique that promises targeted control of particular cells without affecting others in the vicinity, has been discussed in the Section 2.3.

Intracellular recordings are carried out by inserting an electrode through the cell membrane to record from within the cell and they are much more efficient in single unit recordings. However, intracellular recordings require constant and direct contact with the cell, which is difficult to maintain *in vivo*. Also, it is difficult to record from small neurons and the information is limited to single neuron activity. Extracellular recordings, on the other hand, provide a global view of the neuronal environment and involve the electrode being placed close to an isolated neuron for longer periods of time without any damage to the cell. The action potential travelling down a myelinated axon slows down at bare patches of axon membrane every 1-2 mm along the length of the sheath. This regeneration of the action potential at regular intervals boosts the amplitude, preventing it from dying out. Consequently, as shown in Fig. 2-7 from ref. 21, the action potential jumps quickly from node to node and is said to move by *salutatory conduction*.

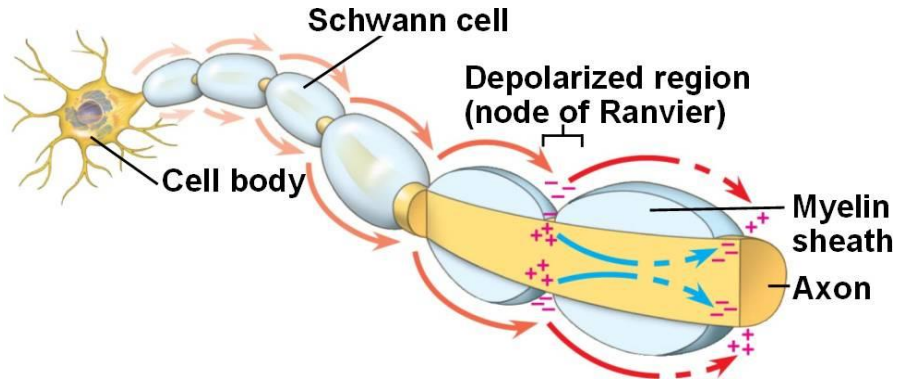

Fig. 2-7: Action potentials in myelinated nerves are regenerated at the nodes of Ranvier.

Cortical gray matter can be thought of as a volume conductor with well-defined boundaries, its material properties characterized by its conductivity, σ. Embedded in this volume conductor is a multi-contact probe, whose electrode wires are exposed to the volume conductor at the position of the contacts.[10] The multipole expansion of the Coulomb potential, V(r) at a distance r away from a charge distribution, ρ(r') is given as

$$V(r) = \frac{1}{4\Pi\sigma} \int_{V'}^{0} \frac{\rho(r')}{|r-r'|} dV' \qquad (5)$$

assuming $r > r'$. Binomial expansion of $1/|r-r'|$ gives a power function dependence of the potential on the distance r as, $V \sim r^{-k}$ where k is characteristic of the multipole: k =1 for monopole; k =2 for dipole; k =3 for the quadrupole; etc. Thus, any change in a charge distribution, $\rho(r')$ would change the Coulomb potential $V(r)$ at a distant point, r. When an action potential is fired, the flow of ions across the cell membrane causes a change in the Coulomb potential measured on the electrode. This is characteristic to the distance of the soma from the electrode and the amplitude of the extracellular potential decreases as we go away from the soma. This minimal distance, r_0 is comparable with the effective size of the current distribution that contributes to that dipole. A rule of thumb is that r_o is about 4

times the soma radius, hence it is much larger for larger neurons. The spatial decay has been analyzed and documented[27,28,29] from which the following conclusions can be drawn:

(a) Within the immediate neighborhood of the soma ($r \leq r_0$), the Coulomb potential at the electrode site is only affected by the charges at the soma and not by the charges at the dendrites. Spatial attenuation is slower than predicted by the dipole model and the EAP falls off proportional to r^{-1}.

(b) When the recording electrode is placed within the range $r_0 \leq r \leq 200$ μm, the charge distribution at both, soma and dendritic arbor affect the Coulomb potential. This data can be fitted with an electric dipole model where the EAP falls off proportional to r^{-2}.

(c) At distances beyond 200 μm, the EAP amplitude would fall off proportional to higher orders of the multipole expansion of the Coulomb potential and hence the amplitude is too small to be sensed by the electrode.

2.4 – Optogenetics

Along with being unable to monitor specific cells, electrical and chemical stimulation are also detrimental to the patient's health. The solution is optogenetic technology, where flashes of light can be used to trigger firing of neurons whose genes are specifically modified to express light-activated opsin proteins – an idea emerged from microorganisms that rely on light-responsive "opsin" genes to survive.[6,7] Optogenetic stimulation can provide millisecond-precision control over the cells' patterns of firing of action potentials. This ability of optogenetic control depends on a number of factors including animal species, brain region and architecture, intrinsic physiological properties

of the cell, opsin response to light stimulation, efficiency of light delivery, and quantity of opsin protein present in the cell membrane.

Basic genetic research on microorganisms that produce proteins that directly regulate the flow of electric charge across their membranes in response to visible light, laid the foundation for the optogenetic approach. In 1971, Walther Stoeckenius and Dieter Oesterhelt[30] discovered one such protein, bacteriorhodopsin that acts as a single-component ion pump that can be briefly activated by photons of green light. Later identification continued with Matsuno-Yagi and Mukohata[31] discovering a member of this family – halo rhodopsin in 1977, that in a special environment participates in ATP synthesis. In 1986, a second halo rhodopsin (NpHR)[32] was described which shows similar function and acts as a direct light-switched chloride ion channel. More recently, in 2002, Hegemann and Nagel[33] reported their findings of a single-protein membrane channel from green alga *Chlamydomonasreinhardtii*. This protein, called Channelrhodopsin-1 (ChR1) is responsive to blue light: when hit by blue photons, it conducts significant amount of Na^+, K^+ and Ca_2^+. Following this, they encoded another sequence of the protein called Channelrhodopsin-2 (ChR2) which acts as direct light-switched cation-selective ion channel.

Viral transduction is used to infuse the opsin-related proteins into mammalian cells, as shown in Fig. 2-8. The light sensory molecules obtained from an alga, are first encoded in a gene and a promoter and are added to a virus. The virus is then injected in the brain, which infects a set of neurons and delivers the gene. A set of neurons will be

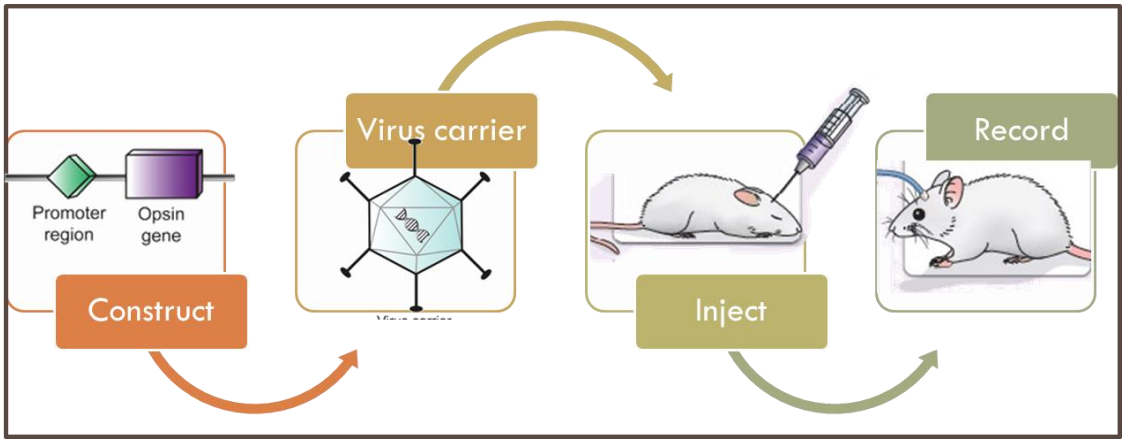

Fig. 2-8: Schematic diagram showing the working principle of optogenetics.

able to activate the promoter and *in only those cells* the gene is expressed in the cell membrane. These cells can then be selectively excited using a fiber optic cable to deliver light. Blue light activated ChR2, acts as an inwardly rectifying cation channel, thus depolarizing the cells. On the other hand, NpHR which is sensitive to yellow light, is a chloride pump, thus hyperpolarizing the cell. These two channels together form an ideal pair for the activation and deactivation of neurons at distinct wavelengths.

Chapter 3 – Neural Probe Design Concept

3.1 – History of neural probes

3.1.1 – Probe functionality

Extracellular recordings were first performed by inserting wires in the leg muscle of a frog back in the 18th century, as explained in Section 2.3. Wires provide the stiffness required to penetrate to deep brain structures, and at the same time are flexible to the natural of the extracellular space due to mundane activities in freely moving animals. Electrical recordings from neurons are invasive, and thin wires do fulfill the desire to minimize inflicted tissue damage. Recording activity from an individual neuron from its extracellular spikes requires the electrode to be substantially closer to that neuron than to the neighboring neurons. Twisting 2 or 4 wires together permits the dissociation of spike signals from two or four different nearby neurons. However, there is a size limitation to this technology for simultaneous recording from multiple layers. Micro-Electro-Mechanical System (MEMS) – based recording devices can reduce these technical limitations because with the same amount of tissue displacement, the number of monitoring sites can be substantially increased.[33] The cost, however, is a device that is too short to probe deep brain structures, has a much larger cross-sectional area, and lacks the ability to map neural activity in 3-D. We have attempted to accommodate the best of both worlds by preserving the advanced functionality of MEMS probes on a thin wire substrate. Section 4.4 describes the design of our probe with the process development in Chapter 4 that follows.

3.1.2 – Probes for Electrical Recording

Electrophysiology has traditionally been the standard for neuronal recordings and stimulation and handcrafted "tetrodes", as shown in Fig. 3-1(a), are preferred for monitoring unit activity in freely moving rodents. These are formed by twisting four wires together, fusing the insulation and clipping off the end. They allow us to sort spikes from different neurons depending on the position of the neuron with respect to the electrode. For example, as shown in Fig. 3-1(b), the pink and grey cell are substantially closer to channel 2 and 4 respectively, and hence produce isolated clusters in amplitude space that enables each spike to be associated with appropriate cell within a population of ~100 cells near the probe tip. Although the tetrodes provide a 3-dimensional map of local neural activity around them, they are fragile and suffer from high contact resistance at the electrode-body interface.

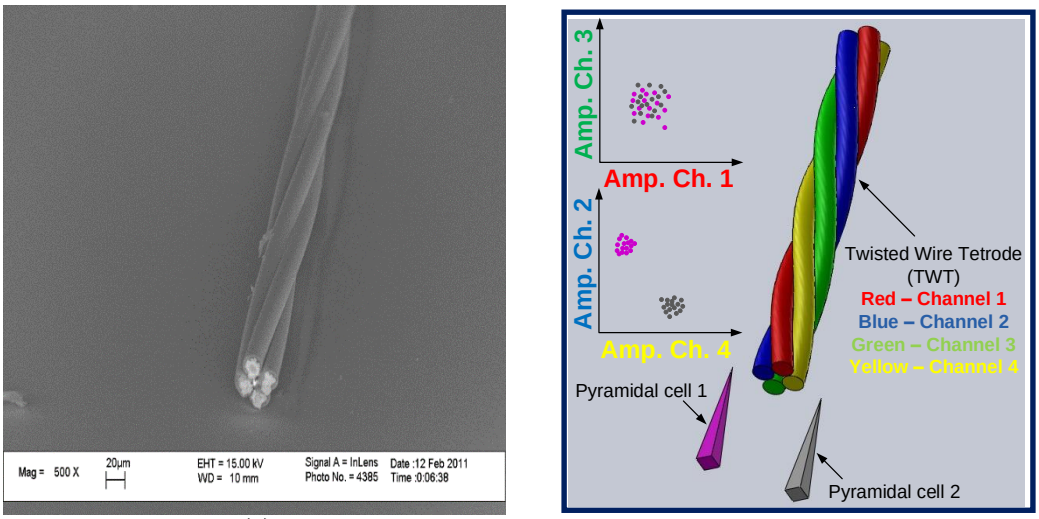

(a) (b)

Fig. 3-1: (a) Tetrodes formed by twisting four insulated wires and clipping off the end (b) An example in which clustering of amplitudes enables the separation of signals from the pink and grey pyramidal cell.

On the path towards adopting the MEMS technology, silicon has been the primary, obvious choice of substrate material due to widespread advancements in thin-film and silicon micromachining techniques. Also, it provides the stiffness that is required for implantation into neural organs. The Hopkins team[34] used Molybdenum as the structure and developed multisite microprobes that allow simultaneous recording from different depths in the brain. The Vienna probe[35] was made of a rigid glass substrate and targeted different aspects of neurophysiological research. This trend was followed by the Michigan probes[36] made on a silicon substrate with an arbitrary shape featuring on-board, integrated electronics and a combination of SiO_2/Si_3N_4 as insulating layers. Eichenbaum and Kuperstein[37] developed a new version of 24-channel microelectrode made on polyimide, which is strong yet flexible and will not fracture as in the case of glass and silicon. The Utah Intracortical electrode array[38] is built from a single 0.2 mm thick silicon substrate One hundred conductive, electrically isolated silicon needles, sharpened at the tip for ease of cortical penetration, arranged in a 10 by 10 grid project out from the base. Each needle is 1.5 mm long and 0.09 mm thick.

Though planar silicon probes boast of ease of manufacturing, they have a large surface area and their thin cross-section causes them to buckle for larger implant depths, thus rendering them unsuitable for chronic neural recordings. To solve this problem, recent advances in MEMS technology have encouraged the use of polymeric microprobes that use flexible materials such as polyimide, SU-8, parylene and PDMS as substrates. With integrated electrodes on one or both sides of the shank, they provide the design flexibility of the planar probes, can be fabricated using simple micro-scale technologies

and are flexible enough to avoid any fracturing or physical damage during implantation experiments.

3.2.3 – Probes for Optogenetics

In-vivo neural stimulation by following the principle of optogenetics requires an optical channel for light delivery which is clearly a drawback in the tetrodes and other planar probes. Deisseroth[39] introduced a solution to this problem by performing simultaneous optical stimulation and electrical recording, an *optrode*, made by simply gluing an extracellular tungsten electrode to an optical fiber with an outer diameter of ~200 μm in a way that is shown in Fig. 3-2, from ref. 40. Though this was an excellent idea, the large diameter of the probes leads to large displacement damage to nerve tissue during surgery. The same approach has been used to study individual neural pathways in the vision system,[41,42] but they offer only single channel recording. Thus, the immediate solution was to glue a tetrode to an optical fiber (Fig. 3-3 from ref. 43). The optrodes are available commercially from Thomas Recording GmbH which were followed by another variation where four tetrodes bundles were rigidly attached together to an optical fiber.

Fig. 3-2: Extracellular tungsten electrode (1MΩ, 125 μm outer diameter) glued to an optical fiber (~200 μm outer diameter).

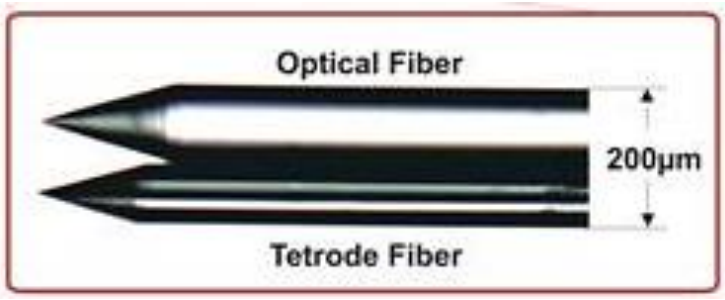

Fig. 3-3: A tetrode fiber glued to an optical fiber reducing the overall diameter to 200 µm.

The total diameter of these probes is >250 µm. There is a version of the planar Michigan probe that integrates SU-8 waveguide on the shank and uses a coupled optical fiber for light delivery (Fig. 3-4, from ref. 44). These probes suffer from high coupling and transmission losses. The previously discussed Utah array can also be used for optogenetic

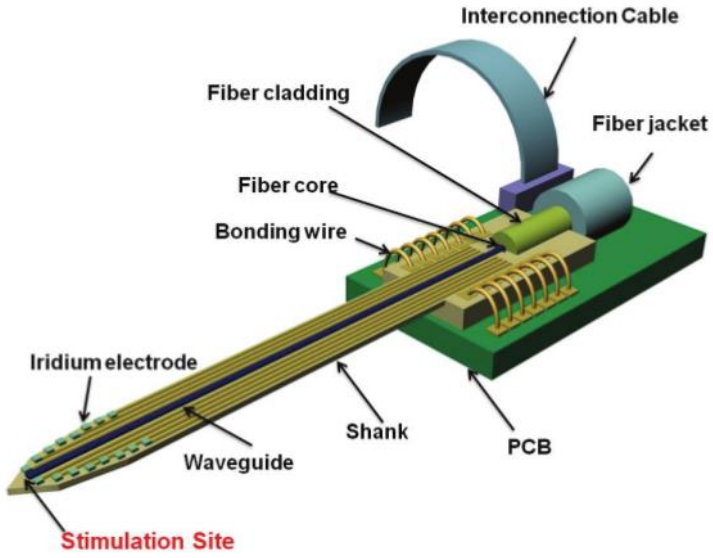

Fig. 3-4: Planar silicon probes with integrated conductor wiring and an SU-8 waveguide for light delivery.

studies by merely replacing one of the silicon microneedles by an optical fiber for simultaneous recordings from multiple sites. Latest advancements in this regard have

been the integration of microscale inorganic light-emitting diodes (μ-ILEDs), with high precision optical, thermal and electrophysiological sensors and actuators, together on a flexible substrate as shown in Fig. 3-5, from ref. 45.

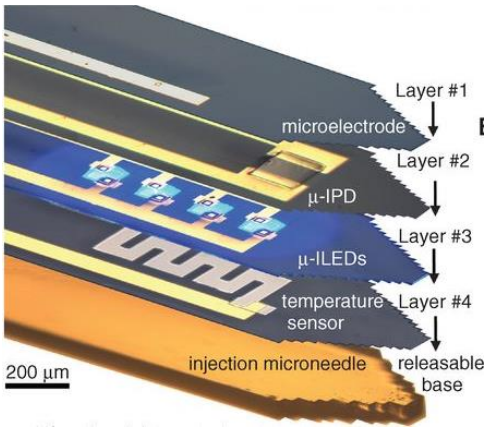

Fig. 3-5: A multifunctional, implantable optoelectronic device.

3.3 – Design Challenges

Implantable neural probes are generally preferred to have a minimum footprint as possible to facilitate easy movement through the brain tissue without damage and increase spatial resolution in neural recording. This also improves the signal-to-noise ratio of the recorded activity. Further, there is growing interest to insert a large number of accurately spaced recording sites into small volumes and this is promoting the application of advanced thin-film and integrated circuit microfabrication techniques to the microelectrode production. Our probe is aimed at showing that a 55 μm fiber (used as the substrate) can be manufactured using conventional IC and MEMS technology.

From the processing standpoint, extending readily available planar technology to non-planar substrates is extremely challenging. Key roadblocks include lack of uniform

coating and misalignment during patterning of thin fibers. Conventional methods like spin and spray coating cannot provide the conformity of coating thickness on the fibers. An alternate plasma coating approach has been explored to achieve the desired uniformity and a novel reliable resist material has been studied. The second roadblock concerns the lithography exposures for defining conductor lines, the most critical step in the processing of these fibers. An innovative alignment technique has been adopted to address this concern. From the electrical point of view, contact impedance between the exposed contact of the probe and the cerebrospinal fluid plays an important role in defining the quality of the signal and ability for accurate data analysis. High impedance in an electrode causes attenuation and results in a filtering effect on the measured signal. To optimize the electrode, the impedance per unit of geometric surface area on the substrate must be decreased.

For the recording experiments, it is essential that the neurons' lifetime not respond to the implanted probe. In addition, for chronic implants, biocompatibility of neural probes is critical to minimize the foreign-body immune response. The materials used for the fabrication of the electrode must satisfy these two conditions.

Above considerations, with the reliable reproducibility of these tetrodes and high throughput manufacturability is the key to successful use of such probes in neuroscience.

3.4 – Visionary probe design for in-vivo neuronal unit recording

The design consideration require the probes to be flexible enough in response to the natural movements of the brain in freely moving animals, yet stiff enough to penetrate at least 2 inches into the brain without buckling as in the case with silicon probes. These

considerations are believed to also minimize the foreign body response which leads to encapsulation of the probe in scar tissue and the death of nearby neurons.

Inability to selectively stimulate certain portions of the brain is a major drawback of electrophysiology. This can be achieved using recent advances in optogenetics where one can causally manipulate selective cell types. Thus, a protocol combining electrophysiology and optogenetics describes a technique for optically stimulating specific populations of excitatory and inhibitory interneurons *in vivo*.[6]

Apart from electrophysiology, selective stimulation of the nervous system at different levels can be now achieved based on recent advances in optogenetics. High molecular specificity, i.e., activation of only the targeted cells within a multitude of neurons can be accomplished with an optogenetic stimulation approach. Furthermore, absence of electrochemical reactions at the electrode/tissue interface minimizes the electrode dissolution or tissue damage. Therefore, many potential complications and side effects may be avoided compared to the current deep brain electrostimulation technology that affects all neurons indiscriminately.

The use of optical fibers as substrates provides high intensity, multi-spectral light delivery, as well as the strength and stiffness required implantation. Also, to achieve a high-precision 3-D map and precise localization of neuronal dipoles requires multiple tiers of 4-channel integrated sensors, with recording sites at the tip that transmit the signal along the shank of the probe. The extracellular action potential (EAP) is hypothesized to indirectly reflect the amount of damage inflicted by an implanted device on neurons in its vicinity;[46] smaller the device size, smaller will be the damaged perimeter of surrounding

neurons and higher will be the amplitude of the extracellular spikes. Based on all these ideas, Fig. 3-6 shows a conceptual drawing of a 55 micron tiered-optrode with an array of thin film electrical sensors at specific intervals along its length. This design also

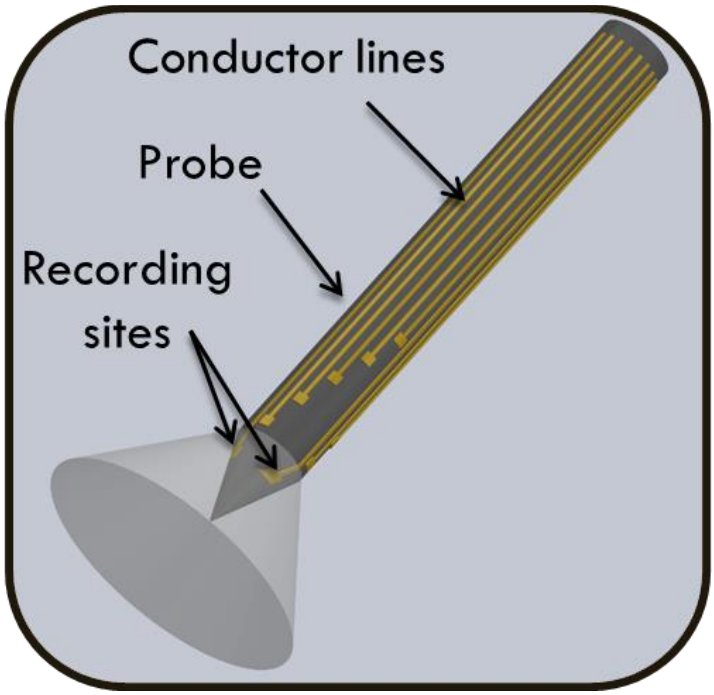

Fig. 3-6: Conceptual design of a neural probe with tiered-tetrode and a tip design which allows optical stimulation and collection.

eliminates the need to gradually advance the probe through the cell body layers in search of a neuron. Owing to the small diameter, it displaces about 90% less tissue than competing electrodes. This dramatically reduces nerve compression damage in dense probe arrays. The optrode also promises to easily deliver 100mW of optical power at the tip and has the stiffness required for stereotaxically targeting transfected regions of the brain.

Chapter 4 – Fabrication Technology

With Moore's law as the driving force, integrated circuit (IC) fabrication technology is rapidly moving toward the integration of 10's of billions of transistors on a single chip with near-atomic scale minimum dimensions. This rapid advance has led to the creation of new technologies with broad applications in other fields, including the micro-and-nanoelectromechanical systems such as air-bag accelerometers, micromotors, gyroscopes, integrated gas sensors, and the bio-chip. Ion beam lithography (IBL) which uses sub-optical wavelength particles to defeat diffraction is an example of a technology developed for the ultra-flat surfaces of IC-chips with profound capabilities on non-planar surfaces. The application of IBL to the fabrication of cylindrical neural probes is discussed below.

4.1 – Plasma Polymerization of Styrene

The prerequisite for lithography on non-planar surfaces is the ability to form smooth conformal resist layers. Conventional processes like spin coating and dip coating are incapable of providing required uniformity on small-diameter fibers (e.g. 60 μm). Plasma-enhanced chemical vapor deposition (PECVD) is an approach that can, under optimal conditions, provide outstanding conformality for films with a wide range of physical properties, including index of refraction, stiffness, and stress.. Such films are used as protective coatings or insulating membranes and have proven to have better biocompatibility compared to classically prepared biomaterials.[47] Our group has shown that plasma conditions can be optimized so that plasma polymerized methylmethacrylate and styrene act as negative tone, conformal resists for energetic particle (e.g. electron,

He^+ ion, and neutral He atom) exposure. Optimized styrene, which we use for probe manufacturing has a sensitivity of 25 $\mu C/cm^2$ and a contrast of 2.3 for 50 keV He^+ ion exposures and amyl acetate developer.

The plasma polymerization of styrene is carried out in a plasma reactor as shown in Fig. 4-1. The chamber is initially pumped to a base pressure of less than 1 mtorr with a turbomolecular pump (CIT Alcatel) which is backed by dry pump (Ebara). Vaporized styrene monomers (Sigma Aldrich) are then introduced in the chamber at a pressure of 1.5 mtorr, which corresponds to a flow of 50 sccm. The chamber pressure is then increased to the desired deposition pressure of 31.5 mtorr by adjusting the position of the gate valve. A glow discharge is then initiated in the reactor with RF (13.5 MHz) power source fed to the cathode.

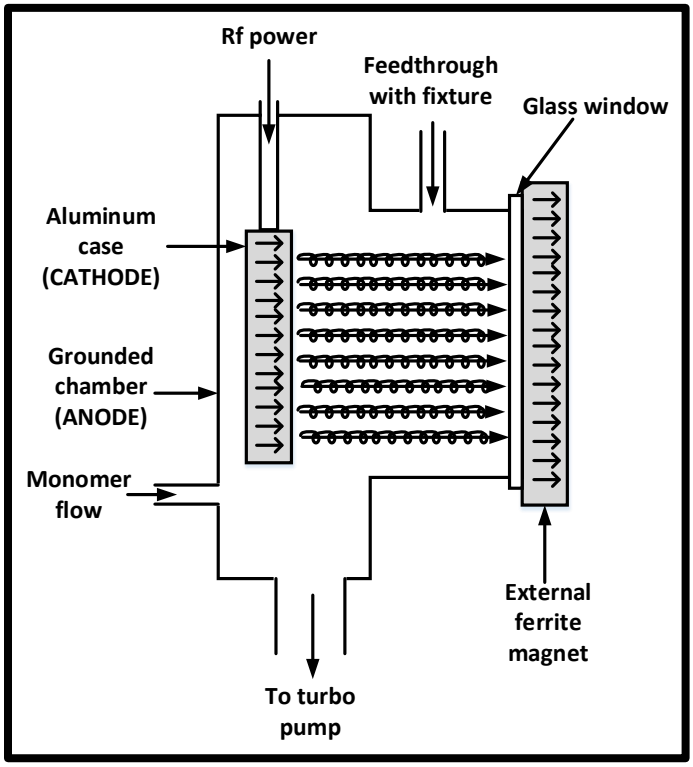

Fig. 4-1: Schematic Diagram of plasma enhanced chemical vapor deposition system.

In this configuration, a magnetic field is created by the perpendicularly polarized ferrite magnet placed inside the cathode casing and an external ferrite magnet placed outside the chamber behind the substrate. The distance between the two magnets is 6.5″. The magnet arrangement is such that the intersection of the magnetic lines is perpendicular to the substrate kept in close proximity to the larger magnet. The motion of the electrons emitted by the cathode can be understood by equating the inward Lorentz force to the outward centripetal force, which yields a circular motion around the magnetic field lines. But due to the E × B fields, the motion of the electrons is a sum of drift and gyration yielding a helical path as shown in the figure.

Plasma polymerization is initiated by the dissociation of the monomer molecules which occurs through either competitive or consecutive reactions.

- Competitive Reaction:

$$M + e^- \rightarrow \begin{matrix} A + B + e^- \\ C + D + e^- \end{matrix}$$

- Consecutive Reaction:

$$M + e^- \rightarrow A + B + e^- \rightarrow A + C + D + e^-$$

Styrene, also known as phenylethene, with the chemical formula $C_6H_5CH{=}CH_2$, can be viewed as a monomer that combines the effects of a double bond and an aromatic structure.[48] In a continuous discharge a large number of radicals are contributed by the phenyl group ($-C_6H_5$) , but in a pulsed rf discharge the dissociation of the phenyl group ceases in the "off" period and a large concentration of free radicals is due to the vinyl

double bond ($CH=CH_2$). These free radicals each with an unpaired electron stabilize themselves mostly by one or more of the three mechanisms – (i) *propagation* – formation of straight long chain polymer chains by breaking carbon-carbon double bonds, (ii) *coupling* – two unpaired electron from different radicals bond together, joining their respective chains and (iii) *disproportionation* – a hydrogen atom is abstracted from a random carbon-hydrogen bond from an adjacent chain while the free carbon radical forms a carbon-carbon double bond in the second chain. The hydrogen can also be taken out from along the backbone of another chain, thus forming a branched polymer (referred to as chain transfer to polymer).

The first mechanism is responsible for the formation of the long polymer chains which is then followed by the either of the next two mechanisms to terminate the polymerization of that chain. The termination mechanism is very critical to the molecular weight of the resulting polymer and its solubility properties in solvents. Styrene monomers undergo free radical polymerization to give a plasma polymerized film on the substrate which is made up of soluble and insoluble fractions. The soluble fraction is believed to be terminated by coupling mechanism, whereas the insoluble fraction is believed to be terminated by disproportionation mechanism. The insoluble fraction is highly cross-linked and hence, is not desired for resist purposes. From our experiments, we observed that this transition from soluble to insoluble polystyrene can be attributed to the RF power supplied to the cathode. Polystyrene deposited at higher power than 15W was found to be insoluble. This is because at high RF power, the electrons temperature and hence electron energy increases. This energy is sufficient to break the C-H bonds at the backbone of polymer chains creating branching sites and enhancing the rate of

termination of polymerization by the disproportionation mechanism. At low RF power, electrons have only the energy required to create free radicals which engage in the coupling mechanism for polymerization.

4.2 – Ion and neutral particle proximity lithography

Lithography is the technology for patterning integrated circuits on semiconductor ICs and MEMS chips. Typically, the pattern is first transferred to a photosensitive material (resist) by selective exposure to a radiation source, and then to the substrate. One type of techniques is helium ion proximity lithography as shown in Fig. 4-2, where a broad beam of energetic helium ions floods a stencil mask, a thin membrane with fine open windows, and the transmitted beamlets transfer the mask pattern onto the resist on a substrate.

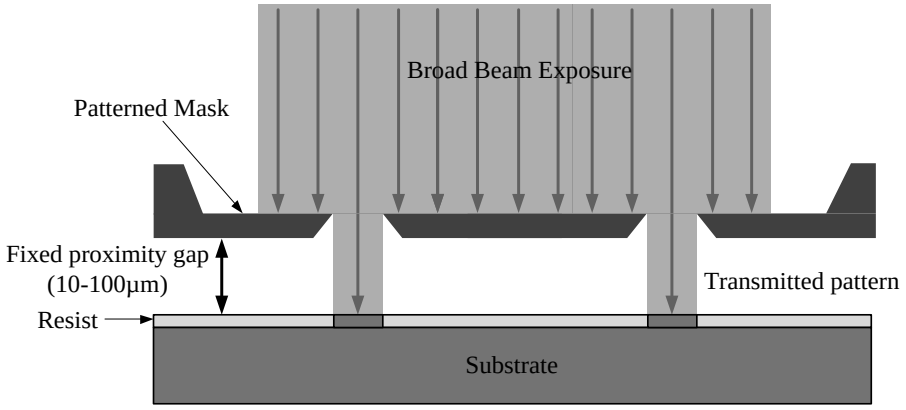

Fig. 4-2: Proximity lithography concept

This is a parallel printing technique with the following advantages: (1) high resolution without the use of expensive hardware, (2) nanoscale resist scattering and negligible diffraction needed for nanometer-scale printing, (3) large depth of focus, which is well suited for patterning nonplanar surfaces and (4) potential for relatively high

throughput for prototyping. The energetic particles can either be photons, electrons, ions or neutral atoms. For photon (x-ray) bombardment, the mask is typically formed by an absorber pattern on a transparent substrate, whereas for all other particles a stencil mask is used.

Reducing the cost and achieving high resolution are the key requirements of a successful process. A limiting factor for resolution in lithography is Fresnel or near-field diffraction. A dimensionless quantity, the Fresnel number is used to classify different proximity lithography tools on the basis of their diffraction conditions. It is defined as $F=a^2/\lambda g$, where a is the feature size, λ is the wavelength of the radiation source and g is the mask-to-wafer proximity gap. Fig. 4-3 shows the Fresnel diffraction pattern for a 100nm wide aperture (ideal case in blue) and 1 mm gap patterned with (a) 50keV He ions (6.63×10^{-5} nm) and (b) 200 nm UV light. It can be clearly seen that while the intensity profile of helium ions is in good agreement with the ideal mask image, the intensity at UV wavelengths is negligible. Hence, the UV light will not be able to pattern a100nm wide line over a 1 mm gap. Penumbral blur is another limiting factor for resolution. As can be seen in Fig. 4-4, for a true point source the shadow cast by the mask has a perfectly sharp edge independent of the distance L from the source or the gap G between the mask and the substrate. For a source of finite extent, however, the edges of the region of full shadow, the umbra is bound by a region of partial shadow, penumbra.

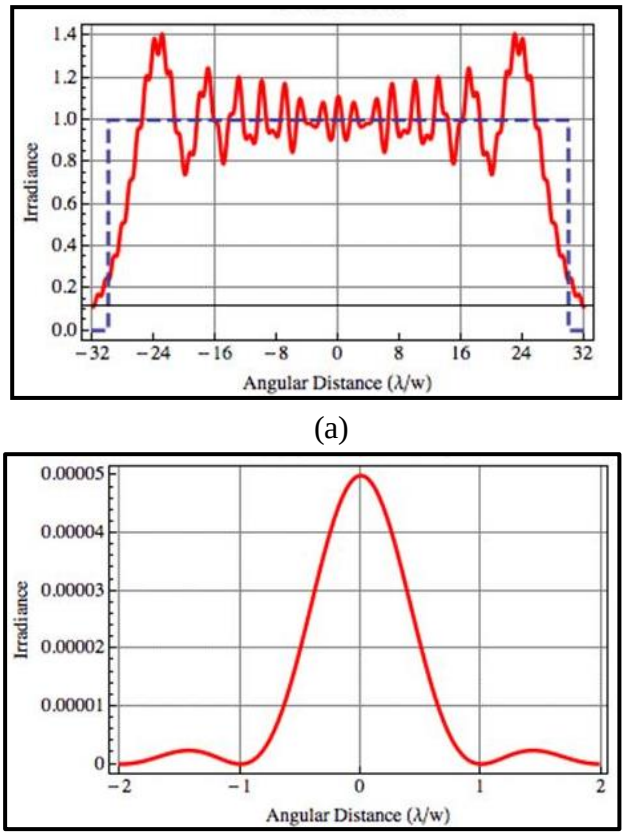

Fig. 4-3: Fresnel diffraction pattern for a 100nm wide aperture (ideal case in blue) patterned with (a) 50keV He ions and (b) 200 nm UV light.

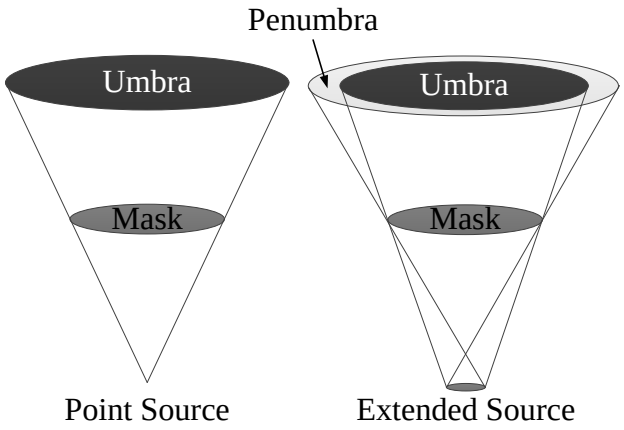

Fig. 4-4: (Left) Perfect shadow cast by a point source. (Right) Penumbral region surrounding the umbra for an extended source.

The relationship between the standard deviation σ_P of the penumbra and standard deviation σ_S of the source is given by $\sigma_P = \sigma_S \times G/L$. Clearly, to reduce the penumbral blur, one or more of the following need to be achieved: 1) reduce the standard deviation σ_S of the source, 2) increase the source-to-substrate distance L or 3) reduce the mask-to-wafer gap. The drawback of adopting the first two ways drastically reduces the current density at the wafer, thus increasing the exposure time by a proportionate amount. The third option can lead to damage to the mask of the substrate if they are in very close proximity. We have developed a high brightness source in order to overcome the current reductions due to a small source or long beamline. This will be discussed in chapter 5 with the rest of the results.

In conventional diffraction-limited photolithography, the minimum resolved feature size d is given as

$$d = k_1 \frac{\lambda}{NA} \quad , \tag{6}$$

where λ is the wavelength of light used is, NA is the numerical aperture of the focusing lens and k_1 is the k-factor or resolution factor for a given process. The semiconductor industry is advancing towards smaller linewidths in ICs, yet it is relying on same wavelength to achieve these linewidths for the same. It started with 436 nm (g-line output of mercury lamp) to 365 nm (i-line output of mercury lamp) to 248 nm (KrF excimer laser) to 193 nm (ArF excimer laser) to 157 nm (F_2 excimer laser) and finally, more recently, 13 nm (Extreme Ultraviolet – EUV laser). However, the use of ions, neutrals and electrons can significantly reduce the smallest feature size. These particles have effective wavelengths given by the de Broglie equation

$$\lambda = \frac{h}{\sqrt{2Em}}\ , \tag{7}$$

where λ is the de Broglie wavelength, h is the Planck's constant, E is the energy of the particles and m is the mass of the particles. The De Broglie wavelength of helium ions at 50 keV is 6.63×10^{-5} nm which is clearly much smaller than the wavelengths of the comparable light sources.

4.3 – Sputtering

The formation of thin films is a critical process that applies to defining the conductor lines along the length of the probes. A large variety of materials, from metals to semiconductors and insulators can be deposited by different mechanisms, namely oxidation, nitridation, chemical vapor deposition, and physical vapor deposition. Among these, physical vapor deposition is a process wherein the atoms that form the thin film are physically ejected from the source before condensing on the substrate as a thin film. These atoms can be ejected by simply heating the source with a hot filament or by the impact of high energy bombardment non-reactive ions. The latter process, known as sputtering, is preferred due to good step coverage and the ability to deposit alloys, compounds, and high-vapor pressure elements. Thus, sputtering is the physical ejection of the target atoms as an effect of energetic ion impact. Since the atomic species are basically removed from the target material, this can be thought of as an etching mechanism, referred to as "sputter etching" and is commonly used to etch noble metals such as gold, silver, etc. Subsequent ejection of the target atoms gives rise to a vapor that

can ultimately condense onto the substrate forming a thin film. This process is termed as sputter deposition.

4.3.1 – DC Magnetron sputter deposition of Au

Sputter deposition is widely used to deposit different kinds of materials such as metals, alloys and barrier layers (TiN, SiO_2). The different types of sputter deposition process include (a) DC/RF Diode sputtering, (b) Reactive sputtering, (c) Magnetron sputtering, (d) Ion beam sputtering and (e) Ion assisted sputtering.

Diode sputtering exhibits efficient use of the target material, since the electric field is quite uniform as in a large parallel-plate capacitor. However, it requires higher operating pressure to sustain the plasma which reduces the deposition rate. On the other hand, magnetron sputtering works on the principle of using a toroidal magnetic field near the cathode for secondary electron confinement, enabling sputter deposition at low pressures and ensuring high quality of continuous and uniform films. Thus, DC magnetron sputtering has proven to be the most useful configuration in this regard.

This process is carried out in a reactor as shown in Fig. 4-5. The target material to be bombarded is placed on the cathode while the grounded anode is where the sample is loaded. This is done so that all the sputtered atoms are collected from the target. In our process, the chamber is initially pumped to a base pressure of 5 μtorr with a turbomolecular pump (CIT Alcatel) which is backed by dry pump (Ebara). High purity Argon gas is then introduced in the chamber at a flow of 7.5 sccm and the pressure is throttled to 5mtorr using a manual gate valve. A glow discharge is then initiated by applying DC power to the cathode.

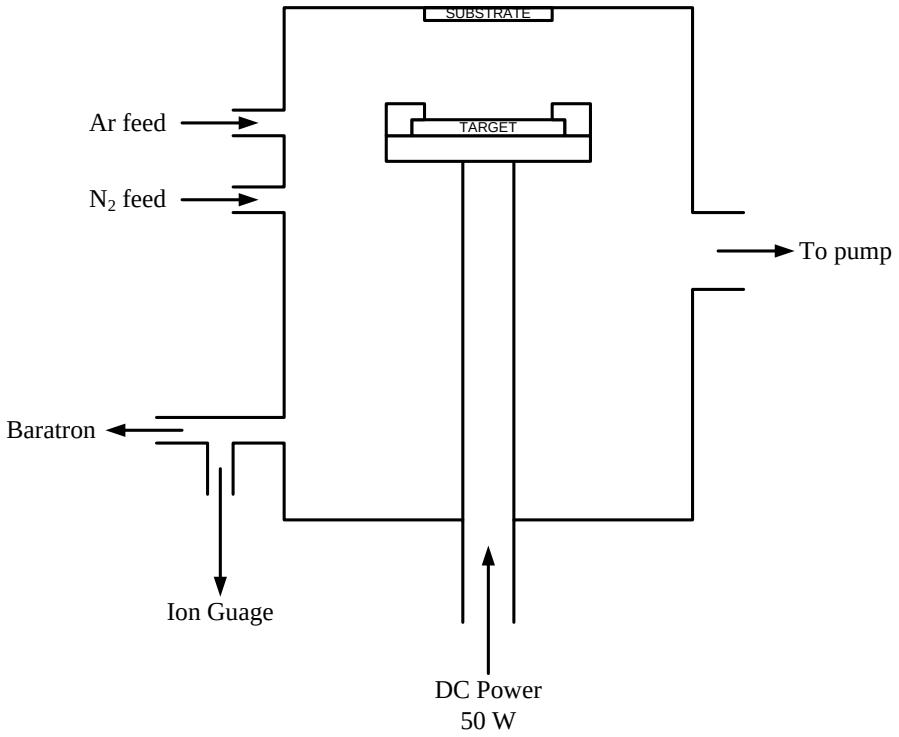

Fig. 4-5: Schematic of DC magnetron sputter deposition system.

4.4 – Fabrication Process Flow

The above techniques were modified and combined with some other techniques to fabricate probes with repeatability and high throughput. The substrate is an optical fiber from Polymicro Technologies with 65µm O.D. optical waveguide having 50µm core, 2.5µm cladding, and 5µm protective polyimide jacket (Fig. 4-6a). The fiber enables efficient light delivery for optical stimulation and provides the stiffness and flexibility for targeting depths of at least 1 cm. A taper is formed at the tip of the probe by using the tube etching technique,[7] where buffered HF is used as the etchant and is topped with a film of an organic solvent (Fig. 4-6b). We then strip the protective jacket which is full of embedded particulates and has been observed to adhere poorly to the fiber substrate (Fig. 4-6c). A new, 320 nm thick, protective buffer layer of a reliable polymer material

(styrene) is then plasma deposited (Fig. 4-6d). The next step is the deposition of the metal layer (Au) for the conductor lines (Fig. 4-6e). This is carried out using a DC Magnetron sputter deposition system. Argon pressure is adjusted to 5mtorr at 75 sccm flow and 50W DC power is applied to the target. To achieve coating uniformity, we use a rotary feedthrough to rotate the fibers at 1rpm during the deposition. This metal deposition is followed by resist deposition using plasma deposition techniques previously discussed in Section 4.3.1. This provides nanoscale conformity over steep topography, that, when coupled with the high depth-of-field and parallel exposure potential of ion beam proximity lithography, enables high-throughput nanoscale patterning on cylindrical surfaces. Plasma deposition of the resist is done in the PECVD tool, as explained in Section 4.1 with RF power of 15W and styrene pressure of 31.5 mtorr (Fig. 4-6f). In the next step, ion beam proximity lithography is used to define the conductor lines by exposing the resist using beam energy of 50keV through a stencil mask for 70 seconds (Fig. 4-6g). This technique simultaneously provides the required depth-of-field and high resolution. Depth-of-field is the maximum distance over which a particular feature size can be defined and its value can exceed the feature size by more than four orders of magnitude. As seen above in Fig. 4-3, 100nm features can be defined over a 1 mm gap. The conductor line pattern is then transferred into the metal layer via sputter etching in an Argon plasma at 2mtorr pressure and 75W RF power (Fig. 4-6h). A second resist layer of Styrene via PECVD is then deposited and a second lithography step using a different set of stencil masks defines the vias and back contacts (Fig. 4-6j). This coating also insulates the conductor lines from the cerebro-spinal fluids. Fig. 4-7a shows the enlarged view of the finished 4-channel probe.

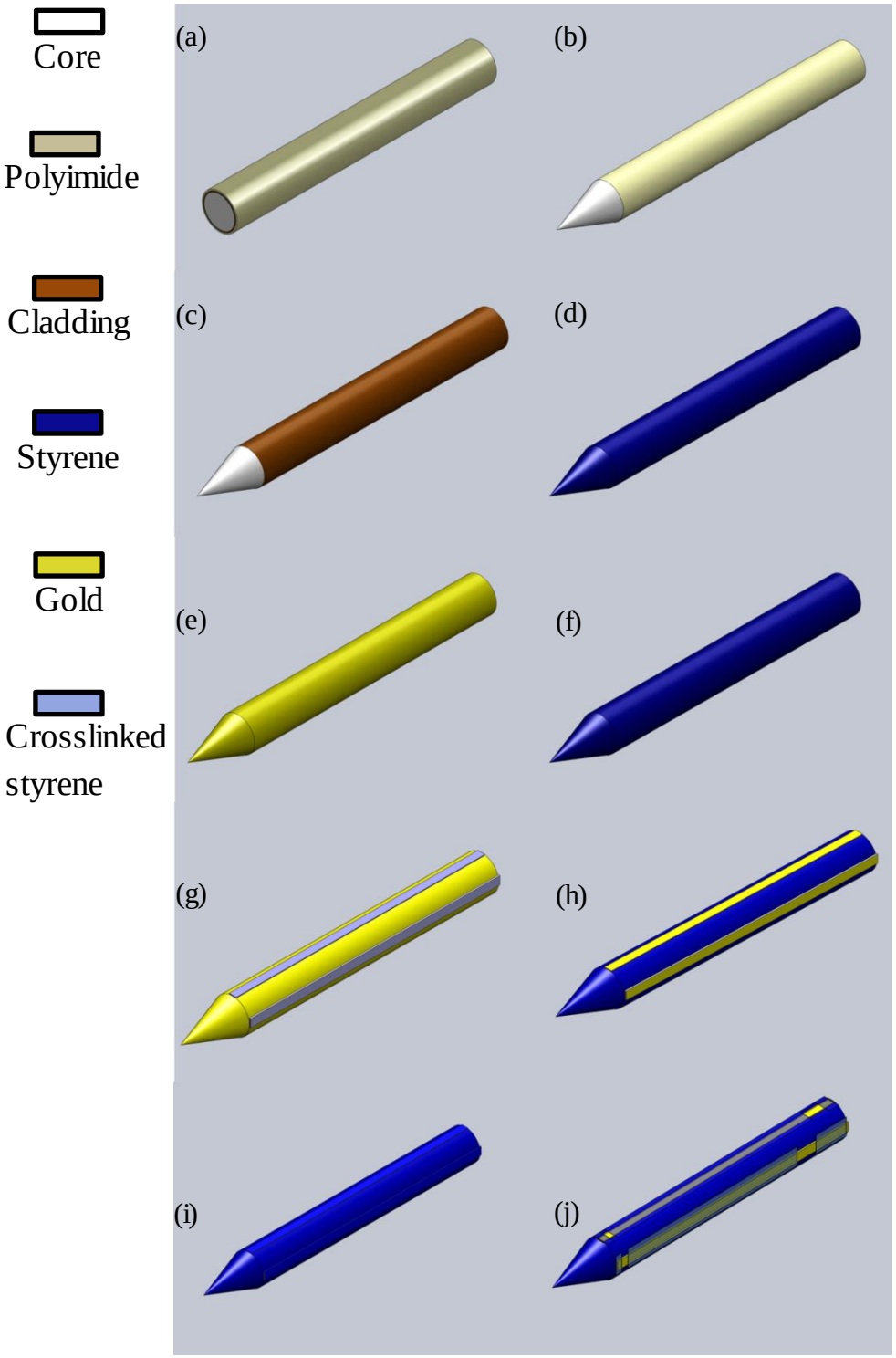

Fig. 4-6: Process flow diagram for the fabrication of single tier optrodes.

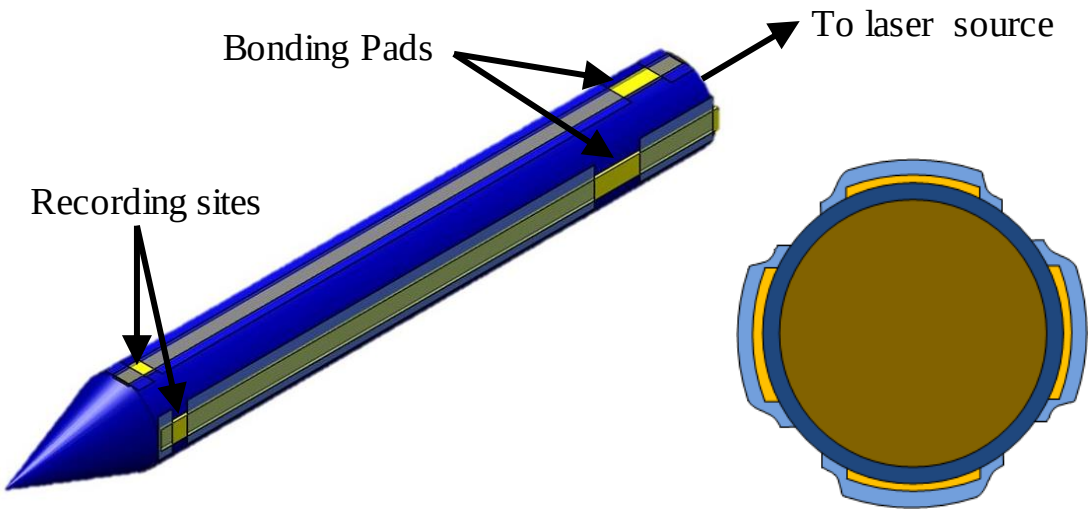

(a)

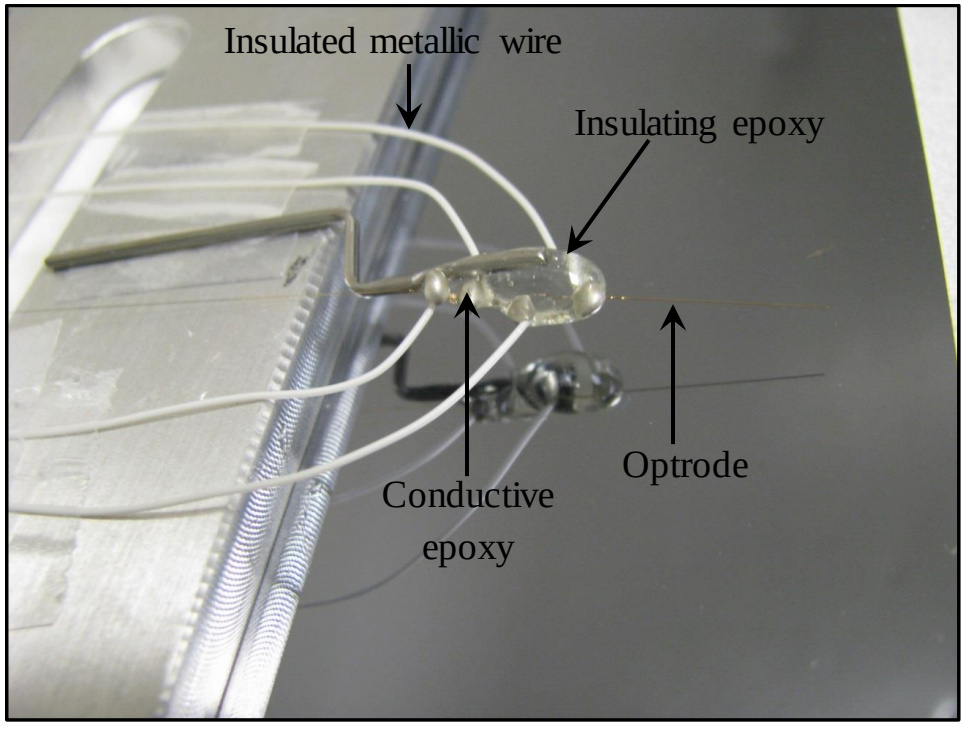

(b)

Fig. 4-7: (a) Finished single tier 4-channel optrode. (b) Optrode with electrical leads for the four tetrode channels.

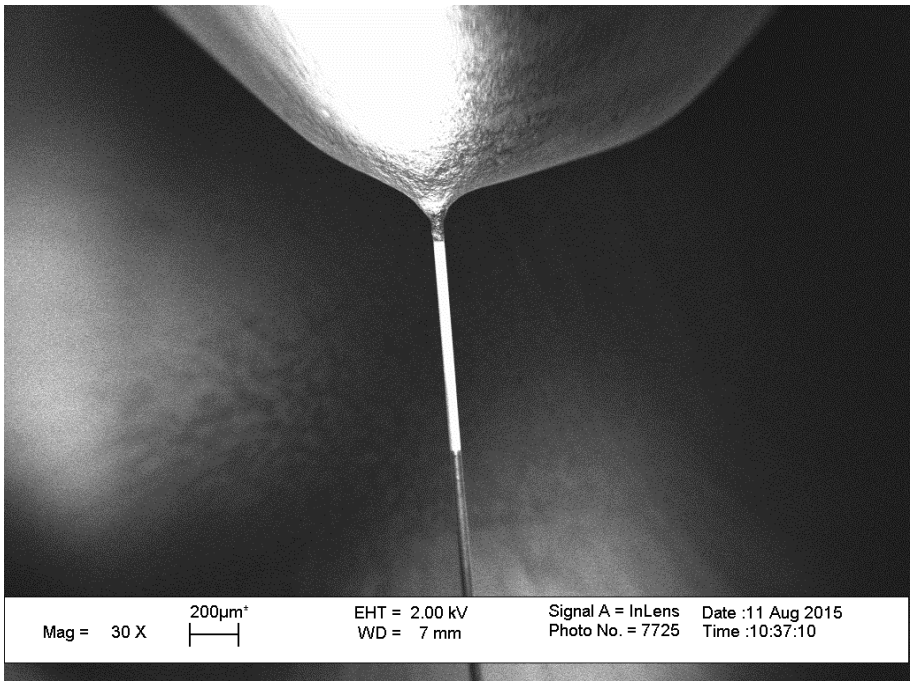

(a)

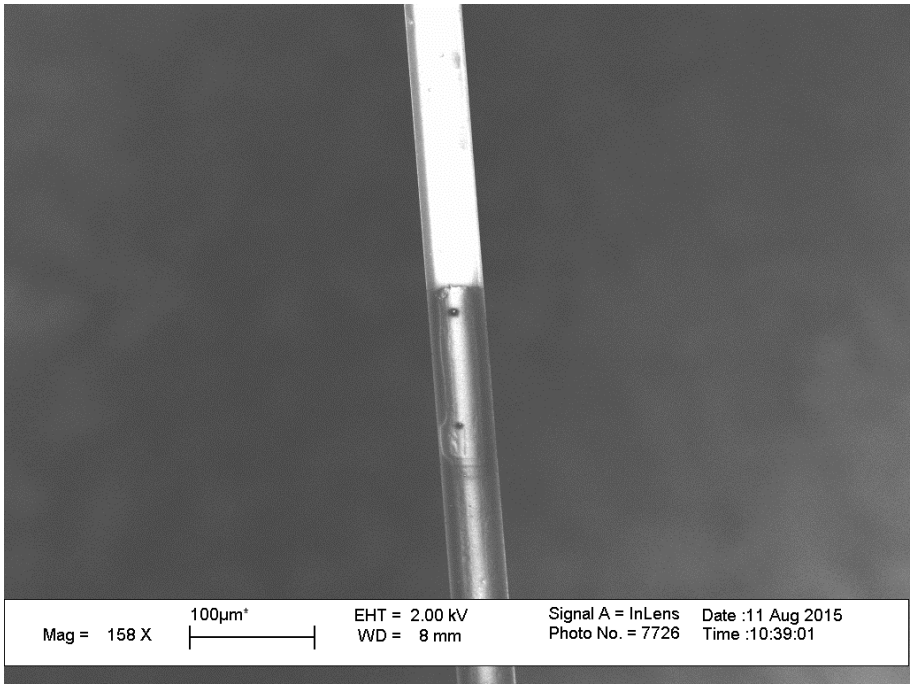

(b)

Fig. 4-8: (a) Glued silver epoxy to one of the bonding pads. (b) Bonding pad.

The final stage is to make electrical and optical connections for communicating with the data acquisition system and laser source. Electrical connection is made using an insulated 30 gauge wire (250 μm OD) to the bonding pad with conducting silver epoxy and the silver epoxy is then insulated using a clear epoxy overcoat (Fig. 4-7b). The micrographs in Fig. 4-8 show one of the bonding pads and the glued silver epoxy. An L-shaped stainless steel tube is then glued near the epoxy bead for handling when it is inserted in the brain. For optical connection to the laser source, the proximal end of the fiber is first inserted into a glass capillary tube with 75 μm ID and then into a stainless steel ferrule with a 160 μm bore. The ferrule then mates with another ferrule on the patch cable and is connected to the laser source using a sleeve.

Chapter 5 – Results

In previous chapters, an overview of the probe concept, design challenges and developed fabrication flow has been presented. As a part of the results section, we further elaborate on resist process optimization, lithography tool development and alignment strategies, high throughput achievement in numbers and *in-vivo* recordings obtained with our probes.

5.1 – Resist process development

Polystyrene serves two purposes in the fabrication of our probes; as a buffer layer and as a resist layer. For each of these purposes, the film was characterized for conformity, ion beam sensitivity and reliability. Not only has the polymer provided excellent stability as the above mentioned layers, it has allowed us to solve one of the greatest challenges facing neural electrodes, which is impedance reliability. We carried out physical and chemical characterization of styrene from the reliability and process capability point of view. The tests and results have been highlighted in the following sections.

5.1.1 – Styrene as the buffer layer

With the polyimide jacket stripped away, the buffer layer serves as a protective layer which needs to be reliable and free of any de-laminations. As-deposited styrene film is soft and cannot provide the required protection; hence it was cross-linked using bombardment with energetic 50keV helium ions. The film was checked for delamination by bending it by a 1” inch radius and it can be seen in Fig. 5-1(a) and (b), no peeling off or damage was observed. The buffer layer thickness was estimated to be 320 nm, which

is thick enough to serve as a protective layer and thin enough to be within the cross-linking range. The SRIM simulation as shown in Fig. 5-1(c) for 50 keV He ion bombardment on styrene, was used for to estimate this thickness.

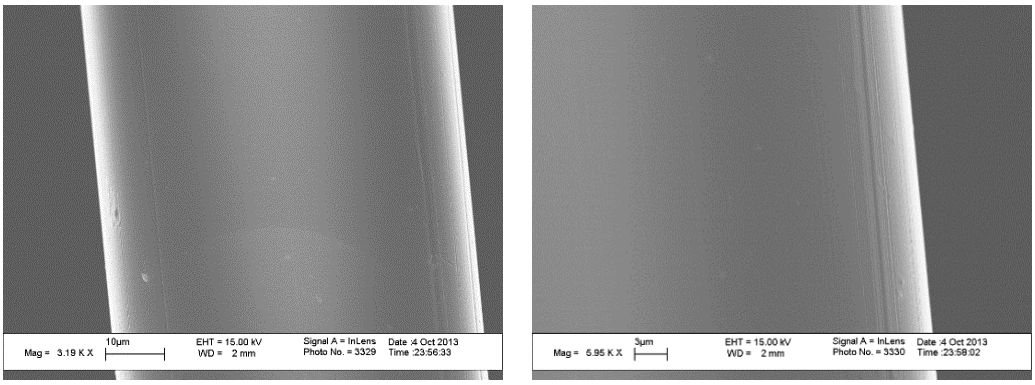

(a) (b)

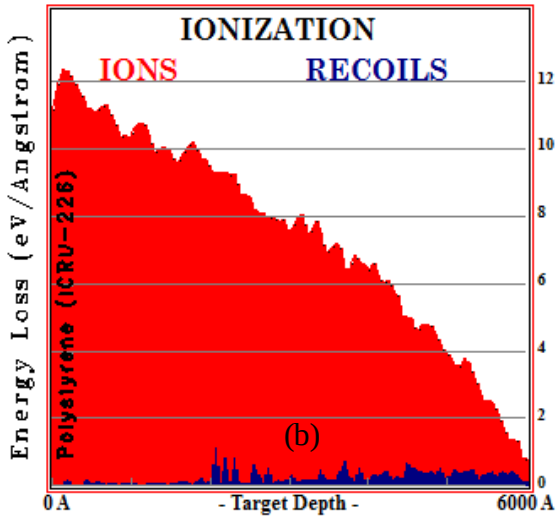

(b)

(c)

Fig. 5-1: (a-b) Styrene deposited probe bent by a 1" radius to check for delamination. (c) SRIM simulation of ion energy loss by 50keV He ions on 6000nm-thick polystyrene.

5.1.2 – Styrene as the resist layer

In order to complement the lithography process for successful patterning on irregular surfaces, it is crucial for the as-deposited resist layer to be conformal and

soluble in particular solvents on development. In 1988, Fong et al showed that high quality electron beam lithography can be carried out in silicon V grooves using plasma deposited styrene as a resist and that reactor power influenced both the exposure and mechanical properties of the resist. Fig. 5-2 shows a micrograph of 0.2μm wide lines showing apparent resist flow and conformal coverage. We explored this property of the

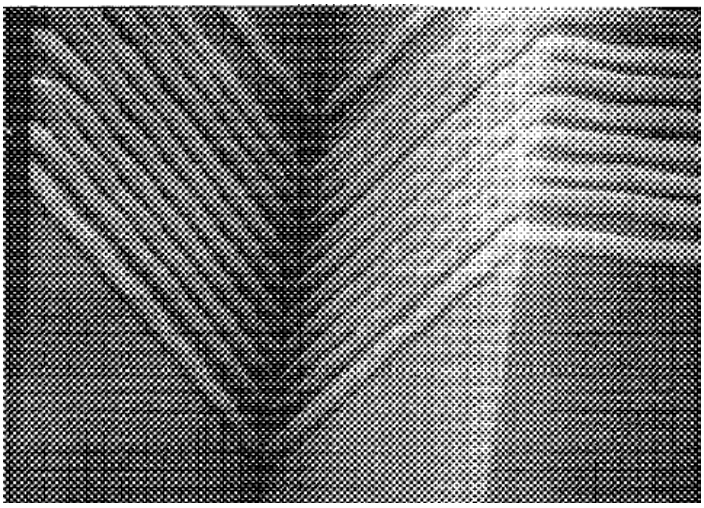

Fig. 5-2: Micrographs of 0.2 μm wide lines traversing the edge of the V-grooves.

polymer for ion beam exposures. The styrene film was deposited at various powers and even though the deposition rate increased, the solubility decreased and the film was rendered insoluble at powers greater than 15W. The conformity of this film was verified from cross section micrographs as can be seen in Fig. 5-3. The thickness of the resist remaining after development to the thickness of the fully exposed resist is shown in Fig. 5-4(a), as a function of ln (dose) obtained by a series of exposures on a 170-nm-thick styrene film with 50 keV helium ions. A linear fit in the transition region yields contrast and sensitivity values of 2.3 and 25 $\mu C/cm^2$ respectively. The application of styrene to nonplanar substrates, where it could bridge the gap between fragile membranes and

planar silicon microelectronics, was explored by patterning a 0.5-µm line/space pattern on a 1.0-µm-thick membrane at the bottom of a 500-µm-deep anisotropically etched well

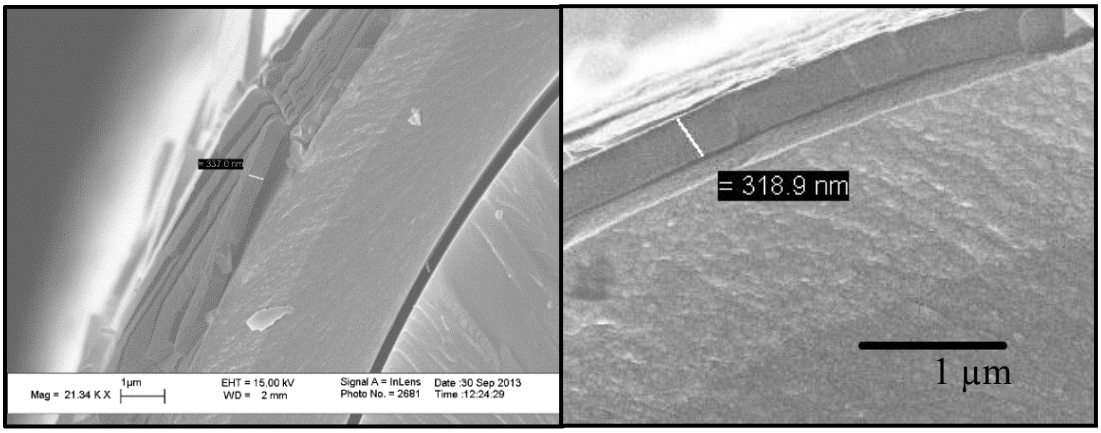

(a) (b)

Fig. 5-3: Cross-section images of as-deposited polystyrene film.

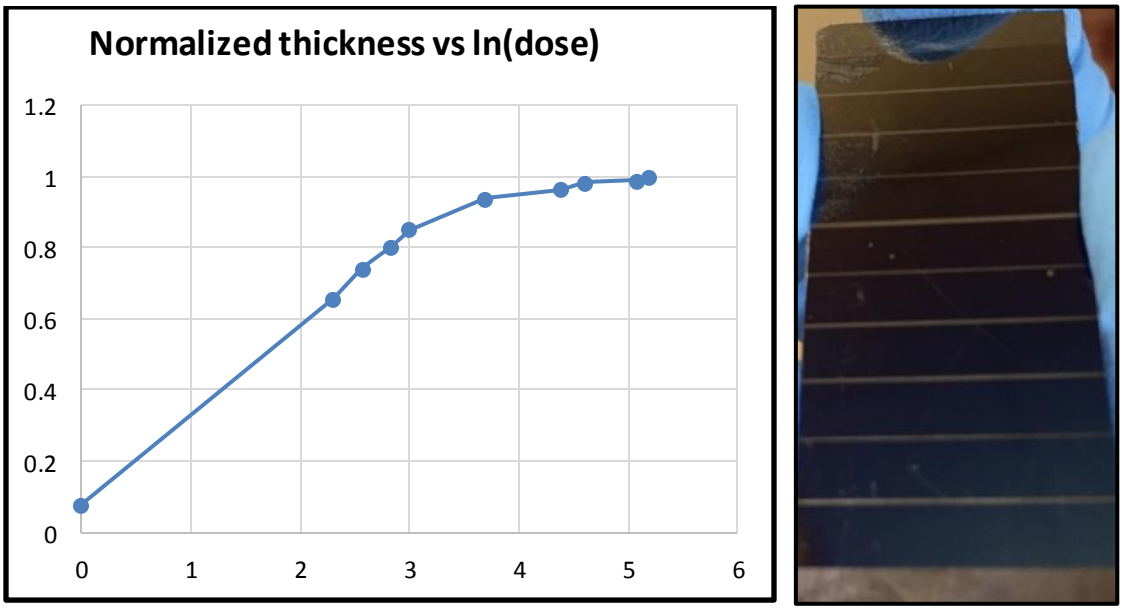

(a) (b)

Fig. 5-4: (a) Plot of normalized thickness remaining as a function of dose. (b) Exposure series performed on a 170-nm-thick polystyrene film.

in silicon substrate. It can be seen from SEM images in Fig. 5-5, that the prints seen on the lighter sidewalls extend all the way up to the top of the well and over onto the surface of the silicon substrate. This experiment was also a good evidence of the high depth of

field capability of the high brightness ion beam proximity lithography tool, which will be discussed in the following section.

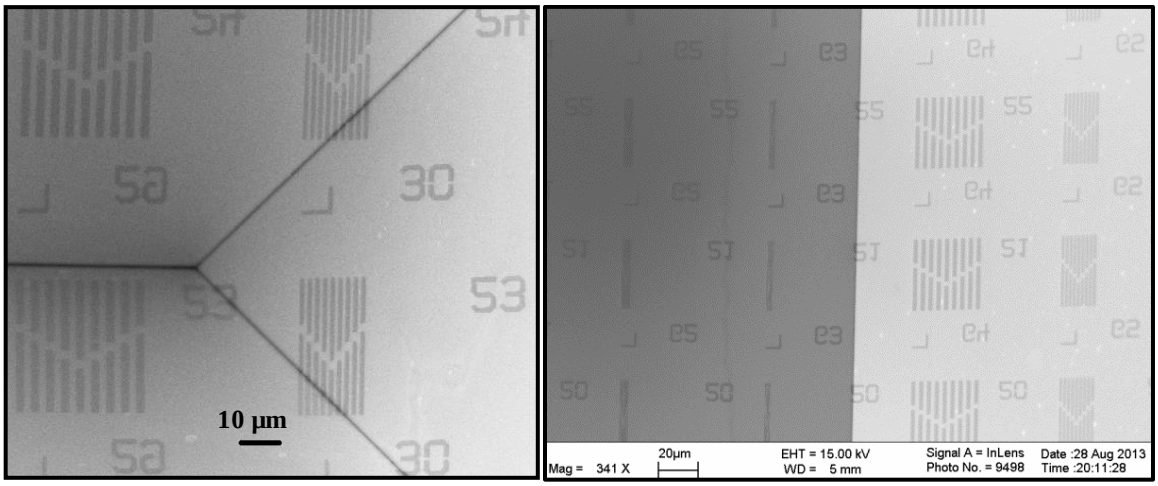

(a) (b)

Fig. 5-5: Mask prints on anisotropically etched well in silicon substrate (a) continuous prints on the sidewalls (b) prints extending all the way up to the top of the well (dark areas).

5.2 – High brightness ion beam lithography tool development

We have established the fact that penumbral blur and diffraction are both detrimental to achieving high resolution, the solution to which is a robust high brightness (large current, small source size) ion source. The lithography tool housing the Hughes multi-cusp ion source was developed at Nanosystem Manufacturing Center in order to circumvent this problem. As seen in Fig. 5-6, from ref. 49, the filament is mounted on a pair of high current, high voltage feedthroughs. The potential of the endplate opposite to the cathode is typically -140V and the cathode can be operated at any negative voltage greater than the endplate voltage. This enables the endplate to reflect cathode electrons back into the plasma this maintaining high ionization efficiency. The cylindrical tube extending into the plasma from the endplate confines the plasma to a region on the axis of

the tube from which ions are extracted through a 1 mm aperture using a suitable extractor voltage. A set of eight permanent magnets of alternating polarity is arranged longitudinally around the circumference of the source producing the magnetic field

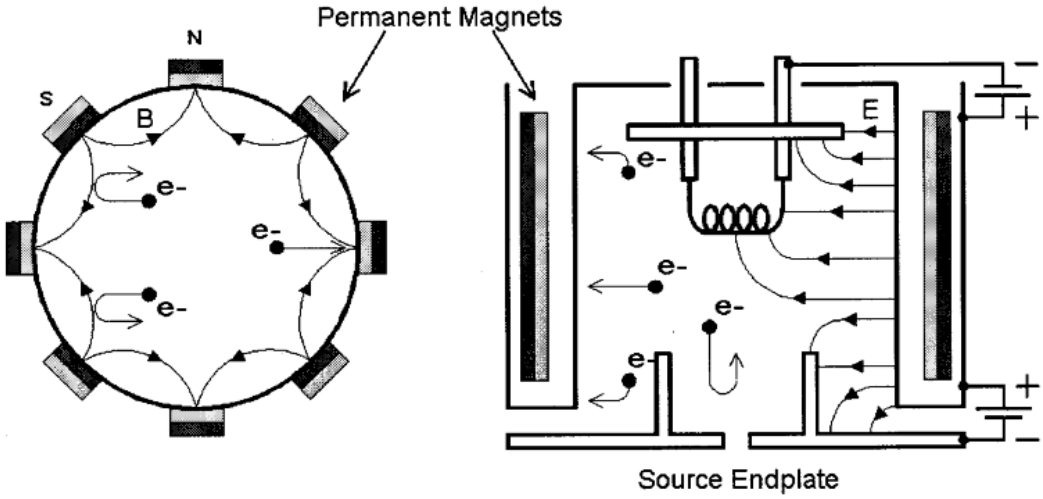

Fig. 5-6: A cross-sectional view of the multi-cusp ion source.

configuration as shown in Fig. 5-6. This overall design ensures high ionization efficiency, uniform distribution of the cathode electrons throughout the source volume and brightness capability of 100 A/m^2-Sr-V at a source size of less than 50μm. Ions extracted from this multi cusp source with energies between 1 and 3 keV for the beam that is then accelerated to up to 50 keV in a 3-electrode lens down a 10m long beamline before they are incident on the substrate. A physical picture of the current tool is shown in Fig. 5-7.

5.2.1 – Beam characterization

A faraday cup was used to measure the total current density for beam energies of 7.5 keV, 15 keV, 30 keV and 50 keV. The beam profile as shown in Fig. 5-8(a) gives a

measure of the beam size which in this case is 3.5 inches. The maximum current was obtained in the case of the 50 keV beam energy as can be seen from the graph of the beam current as a function of the beam energy in Fig. 5-8(b).

(a)

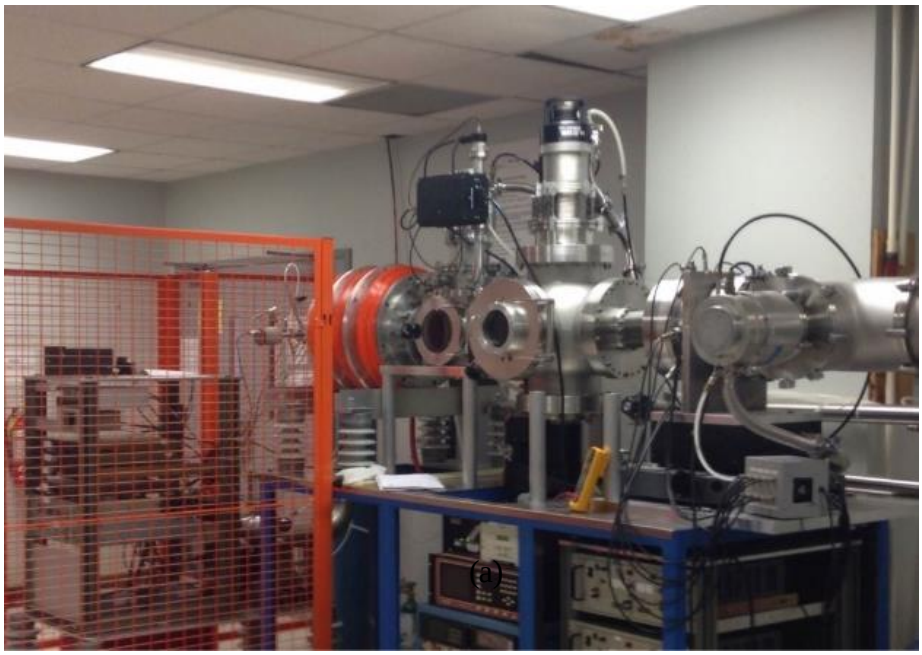

(b)

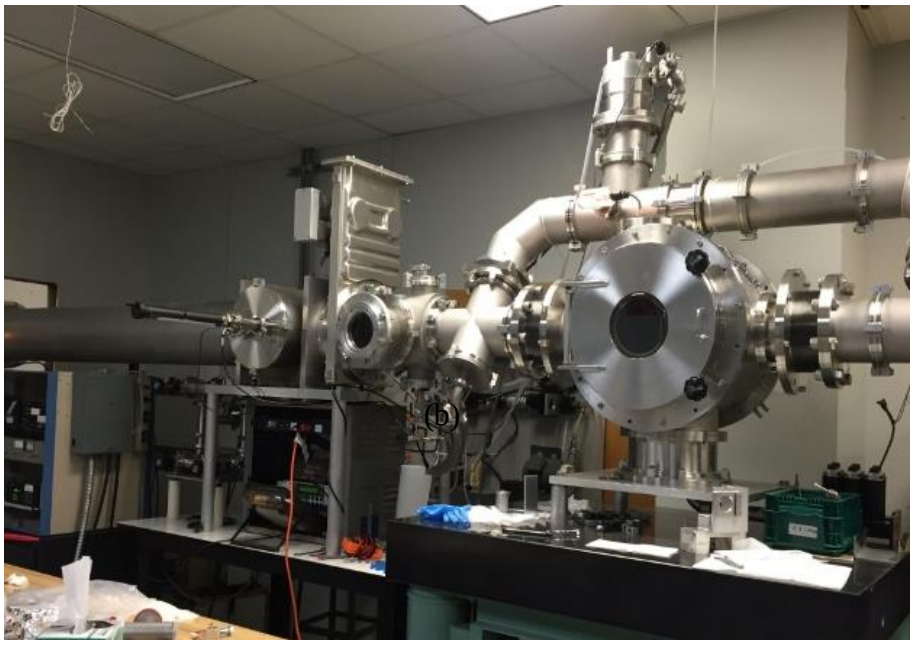

Fig. 5-7: Helium ion beam lithography tool (a) source chamber (b) exposure chamber.

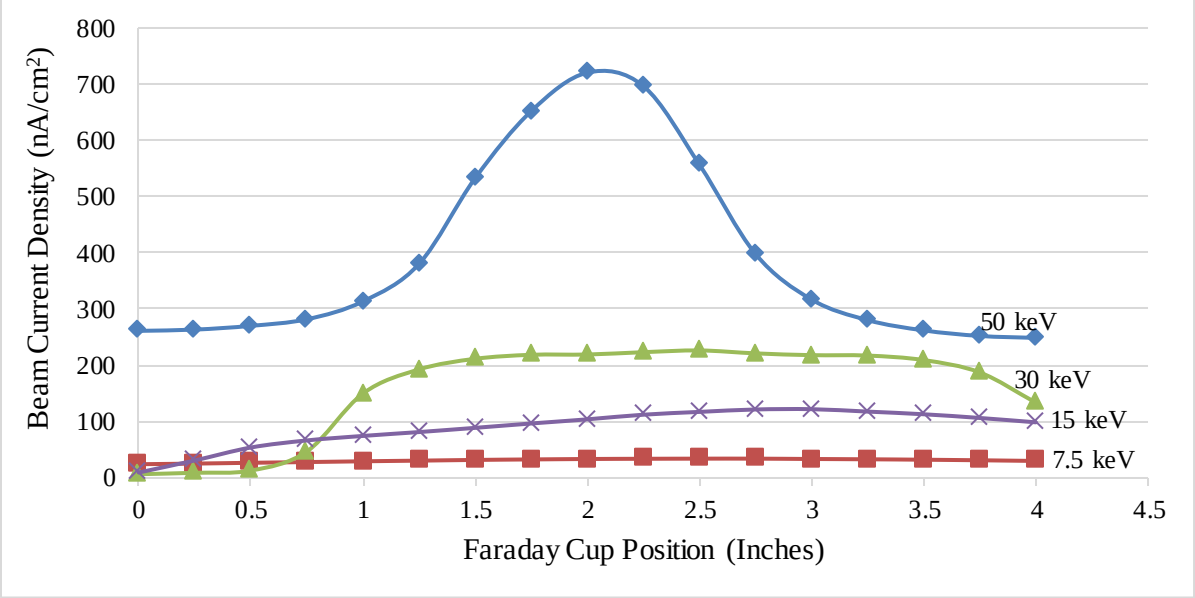

(a)

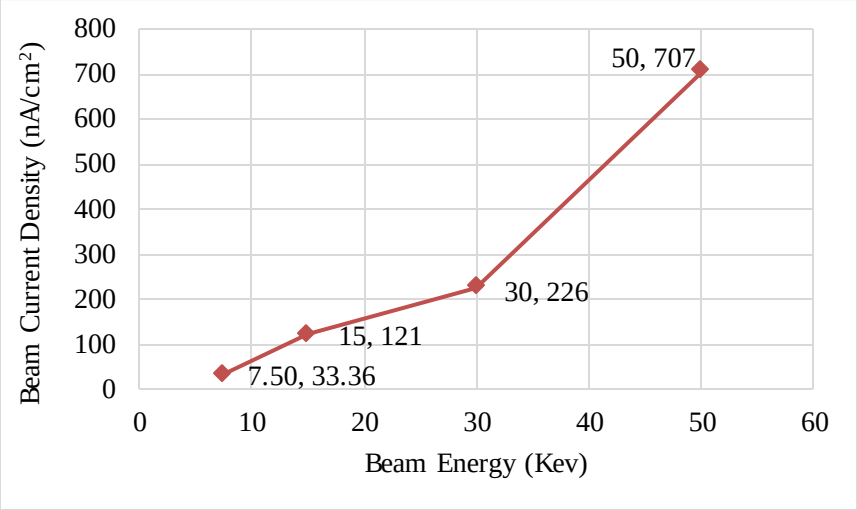

(b)

Fig. 5-8: (a) Beam profiles for beam energies ranging from 7.5 keV to 50 keV. (b) Beam current density as a function of increasing beam energy.

Though the current was higher, the beam was uniform over a larger area in the case of 30 keV. Thus, another parameter affecting the shape of the beam was explored; extraction voltage. This is the voltage applied to the extractor, in immediate vicinity of

the end plate, and is used to extract the ions from the plasma. The beam profile in Fig. 5-9 shows the normalized beam current density at various values of extractor voltages ranging from 2.3 kV to 3.1 kV. The beam was found to be totally flat over a 3.5 inch exposure field and the maximum current density obtained, with focus voltage adjusted to 0 keV, was 700 nA/cm^2. The effect of the focus voltage can be attributed to the presence of the space charge effect which causes the mutual-repulsion between charged particles in a region of high charge density. The dependence of the spread of the current density on the extractor voltage is due to differences in the plasma density. There are 3 cases of ion

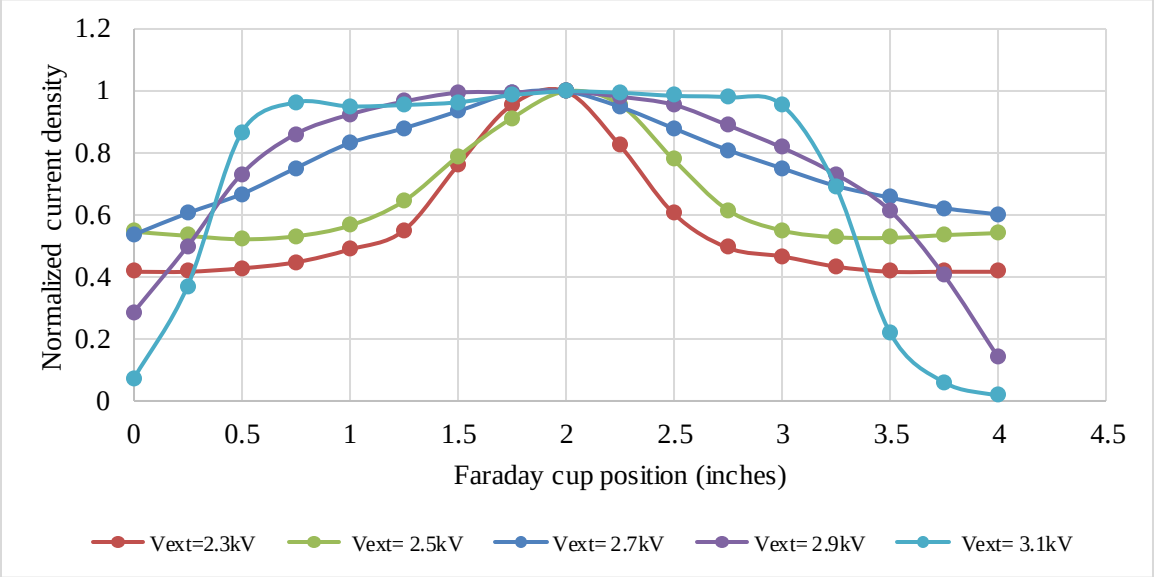

Fig. 5-9: Beam profile at 50 keV beam energy at different extractor voltages.

extraction from plasma source as seen from Fig. 5-10: (a) over dense plasma (plasma density is high, meniscus will be approximately spherical with its center of curvature inside the plasma. (b) Intermediate plasma (planar plasma and meniscus) (c) under dense (plasma density is low, meniscus is spherical with center of curvature outside the

plasma.[50] The shape of the meniscus and thus, the beam can be changed by adjusting the voltage of the extraction lens.

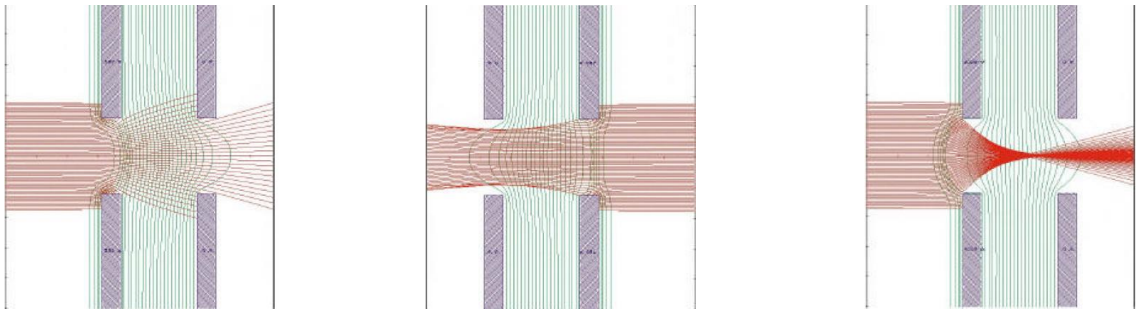

(a) (b) (c)

Fig. 5-10: Plasma extraction: (a) over dense plasma, (b) intermediate density plasma, (c) under dense plasma.

Based on the above mentioned considerations, the best case operating conditions of the ion source that result in a high brightness uniform beam have been identified as shown in Table 1.

Table 1: Best operating conditions for ion beam lithography source.

Beam energy	Discharge current/voltage	Source pressure
50 keV	4A/55V	8mTorr
Focus voltage	Extraction voltage	Filament current/voltage
0 keV	3.1 kV	10A/12V

5.2.2 – Alignment for lithography

With the use of nonplanar substrates, the transfer of mask pattern in a stencil mask on to a perfectly aligned fiber is difficult to achieve. There is bound to be linear or angular misalignment of the fiber with respect to the incoming beam as shown in Fig. 5-11, from ref. 51. A micro machined alignment jig was designed at UH as a solution to

this problem. It enables self-alignment of the mask to the fiber and also provides a small proximity gap between the mask and the fiber.

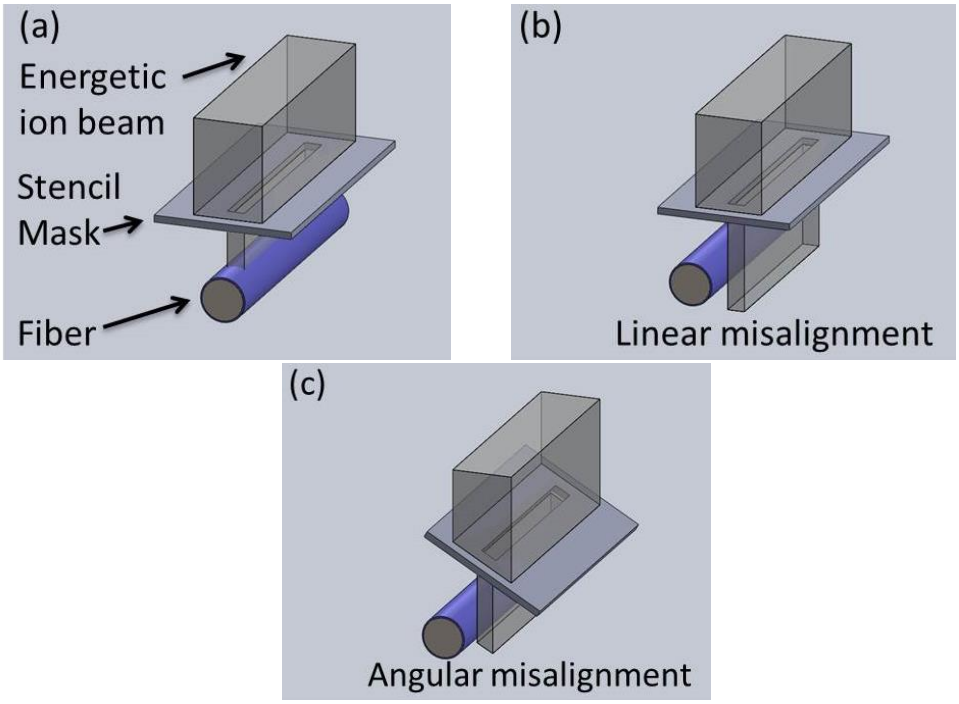

Fig. 5-11: Alignment issues with patterning. (a) Transfer of mask pattern in a stencil mask on to a perfectly aligned fiber, (b) Linear misalignment of the fiber with respect to the incoming incoming ion beamlets, (c) angular misalignment of the mask-fiber arrangement with respect to the incoming beam.

The jig [Fig. 5-12(a)] has one set each for 5, 10 and 15 micron lines with 4 openings per set. These openings are formed by vertically aligned v-grooves and the fiber is positioned in the groove in such a way that it protrudes above the plane of the wafer [Fig. 5-12(b) and 5-12(c)] so that it can be held down with the help of springs. Exposing the jig from the other side with energetic helium ions [Fig. 5-12(c)] creates a negative tone image on the resist which protects the conductor layer during the etching step thus forming gold conductor lines. Fig. 5-13(a) shows a set of 4 probes set in the grooves ready for exposure

and a 50 µm wire placed across them in order to secure them in the groove. The probes are also supported by additional springs that run from the top plate, thus securing the fiber in place [Fig. 5-13(b)]. Corresponding micrographs in Fig. 5-13(c) show the 50 µm wire and Fig. 5-13(d) and (e) shows the alignment provided by the groove when the fiber is placed in it.

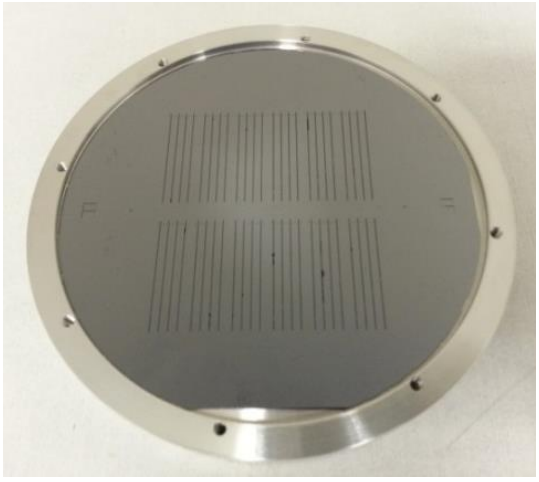

(a)

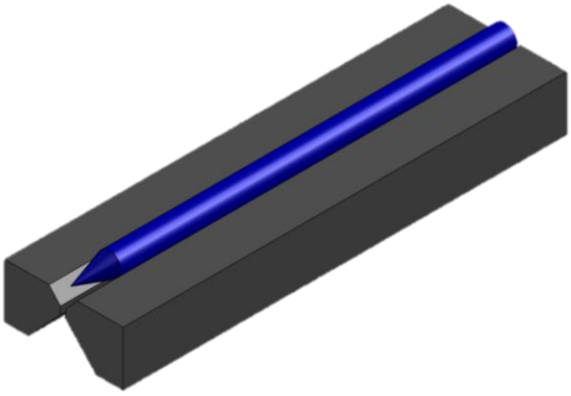

(b)

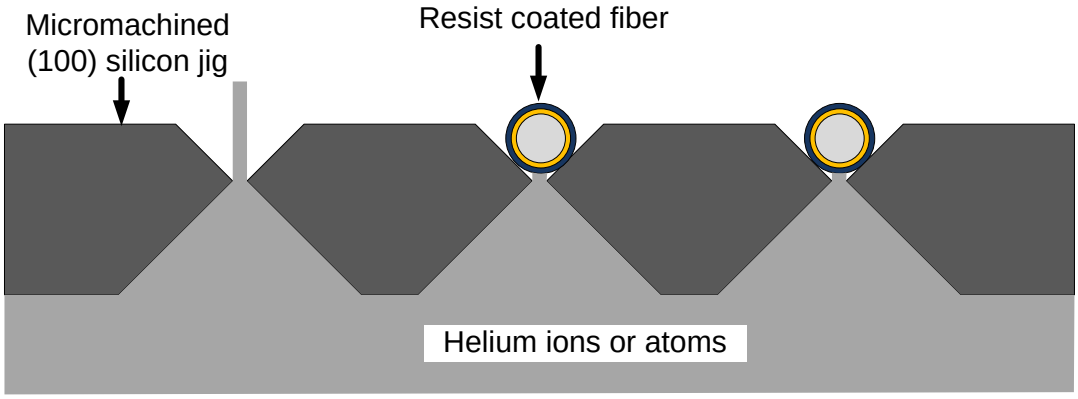

(c)

Fig. 5-12: Micro machined alignment jig: (a) Sets of V-grooves with different linewidths, (b) Positioning of the fiber for perfect alignment, (c) Back side exposure creates a negative tone image on the resist coated fiber.

Fig. 5-14 shows micrographs of a wide strip of styrene on three different probes exposed with 50 keV He ions using the 5 μm and 10 μm line mask. There is perfect alignment between the fiber and the strip over the entire length 1.5″ of the active area.

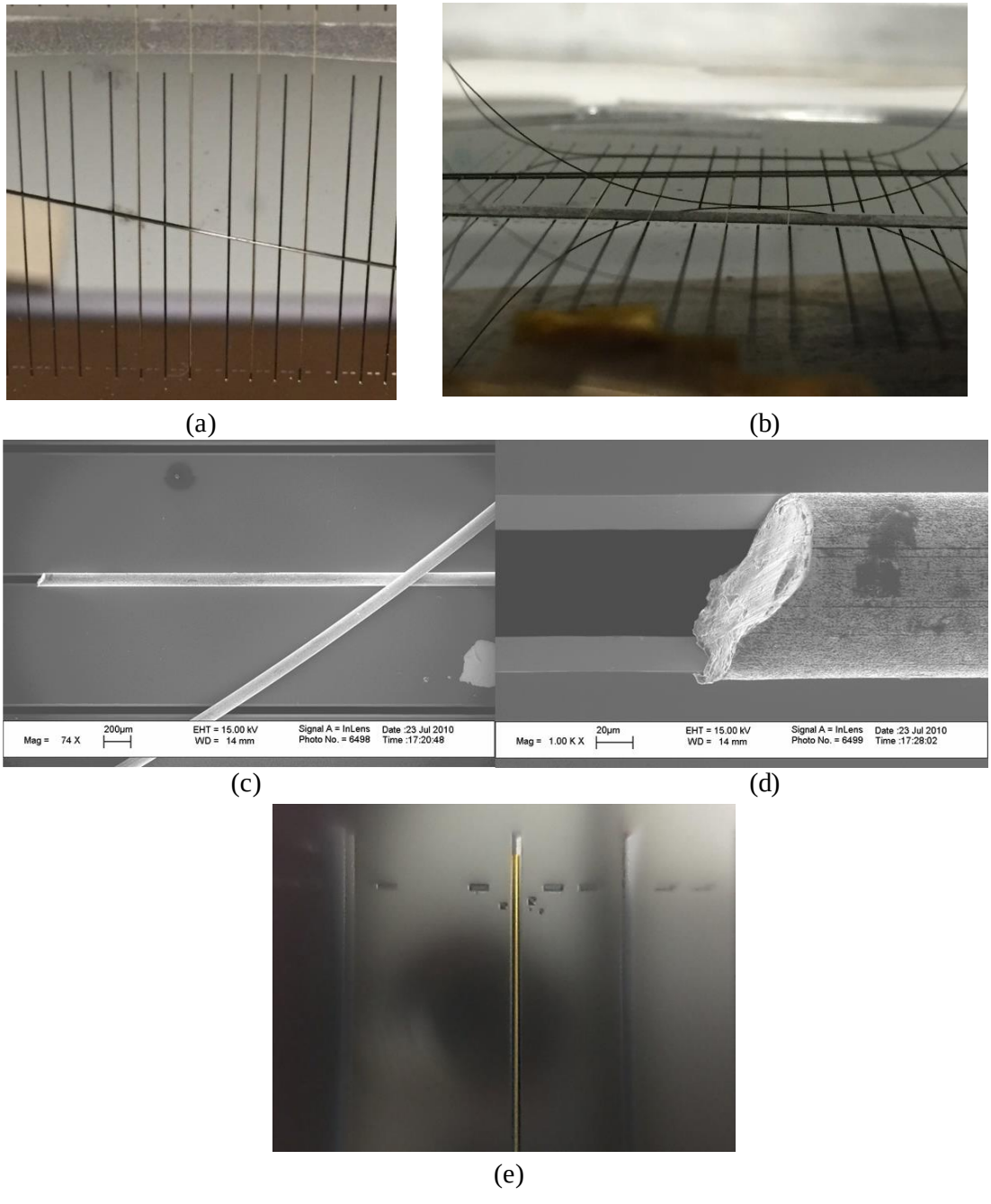

(a) (b)

(c) (d)

(e)

Fig. 5-13: Micro machined alignment jig. (a) Four fibers placed in the grooves with a wire across them, (b) Extra springs to clamp the fibers in the grooves. (c) SEM image showing a a fiber and a wire running across it. (d) SEM image showing alignment of the fiber when placed in the groove. (e) placement of a probe in the groove.

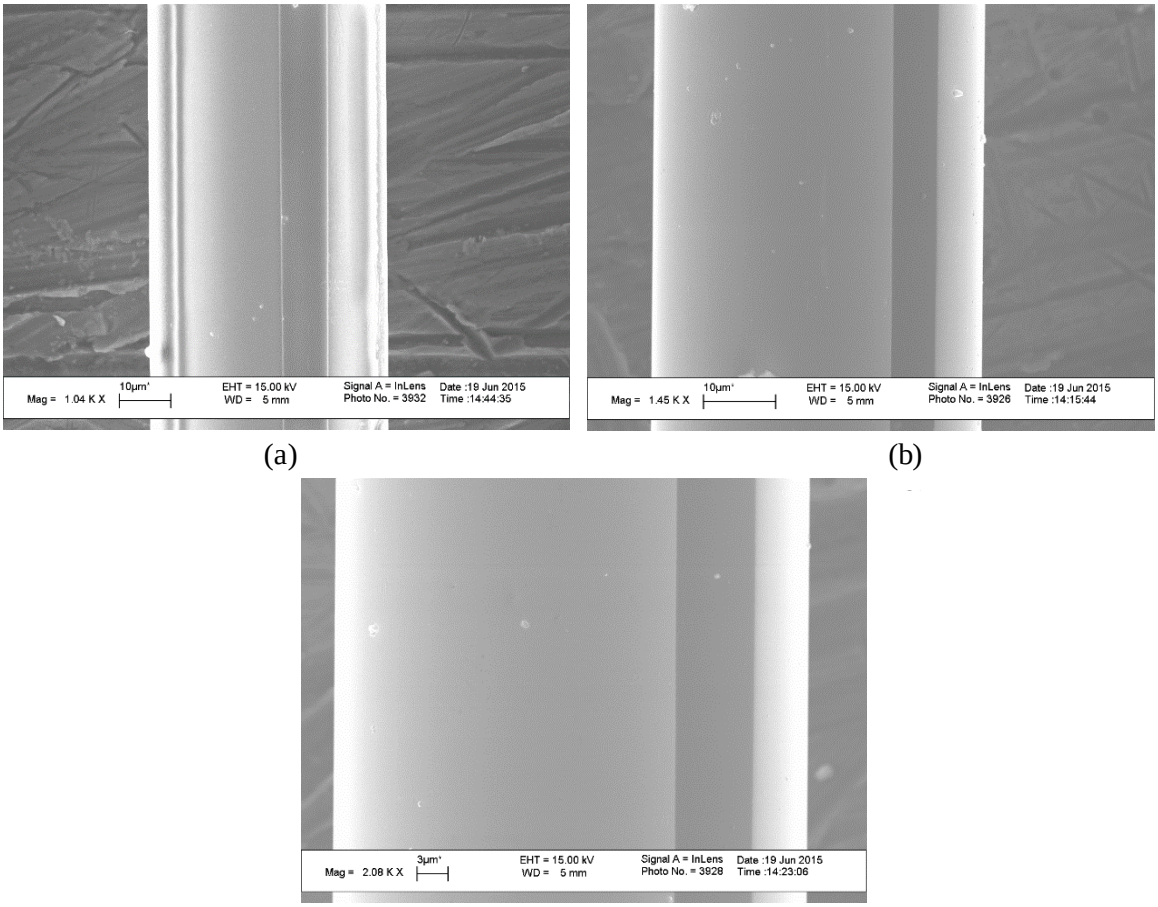

Fig. 5-14: SEM images of a wide strip of styrene exposed using 50 keV helium ions (a) Probe 1: 10 µm. (b) Probe 2: 5 µm and (c) Probe 3: 5 µm.

Fig. 5-15 is the result of the etching steps; (1) gold etching where the polystyrene strip from the previous figure protects the gold line underneath and (2) the remaining polystyrene is etched away leaving behind the gold conductor line. The final patterning step for contacts also takes advantage of the sophisticated alignment, laterally and longitudinally. Micrographs in Fig. 5-15 show two such contacts obtained by aligning the fiber with a contact mask. The yellow labels mark the boundary of the lightly visible contact in one of the probes.

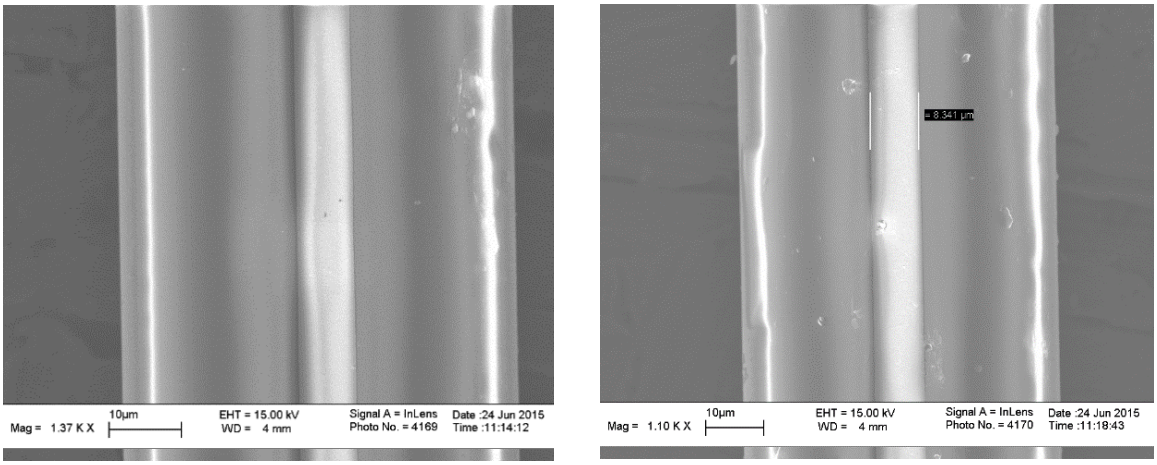

(a) (b)

Fig. 5-15: Post-etching images of the gold conductor line (a) Probe 1: 10 µm (b) Probe 2: 10µm.

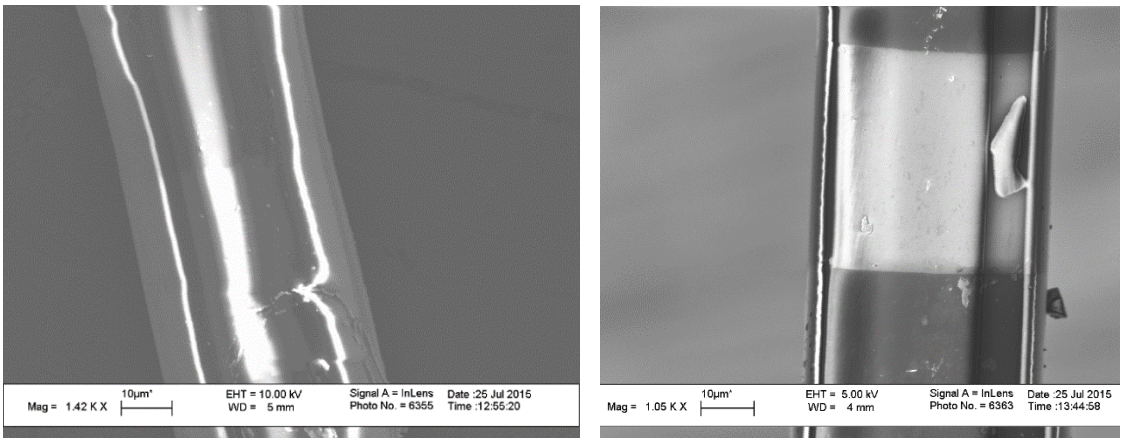

(a) (b)

Fig. 5-16: SEM images of well-aligned gold contacts (a) Probe 1. (b) Probe 2.

5.3 – Throughput improvements

The degree of parallel processing in any manufacturing environment is a direct measure of the product throughput. In order to facilitate simultaneous processing, a special fixture [Fig. 5-17(a)] was designed at Nanosystem Manufacturing Center which is capable of processing 6 probes in any given process run. A 4mm Swarovski crystal acts a

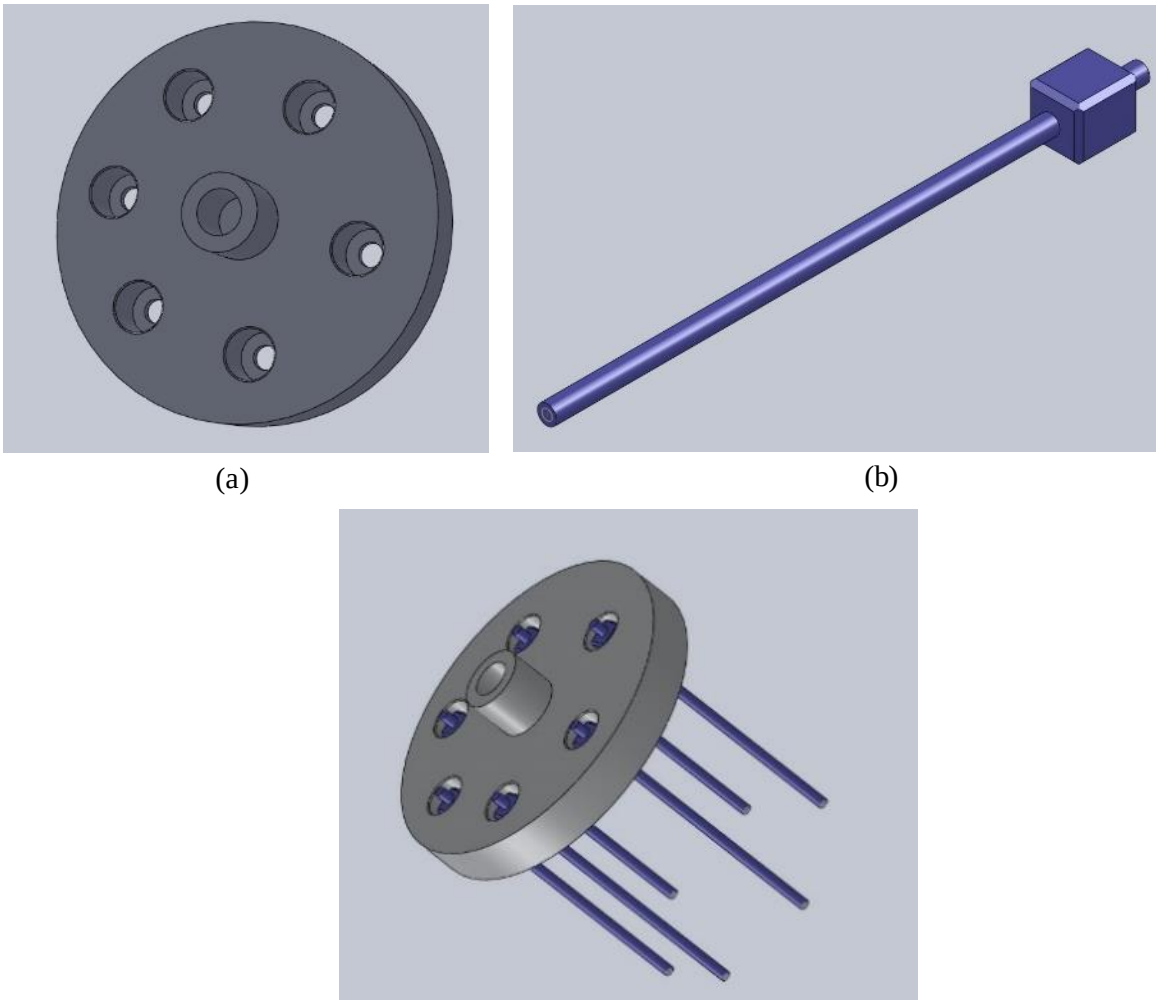

Fig. 5-17: (a) Fixture for increasing processing efficiency, (b) A Swarovski crystal acts as the handle for the probes, (c) The fixture can be integrated with any processing equipment and rotated according to process conditions.

handle for the probes to be loaded in the fixture [Fig. 5-17(b)], which is integrated with every processing equipment. The fixture is rotated stepwise, thus compensating for any shadowing effects and provides 3-dimensional uniformity as an added advantage [Fig. 5-17(c)].

With the advancements in process conditions, materials and equipment optimization, the throughput was dramatically increased as shown in Table 2.

Development of an improved lithography source and a plasma resist deposition process reduced the exposure and resist deposition times respectively, by a factor of 20. The increase in the exposure field by a factor of 3 and the complementary fixture has promoted the patterning throughput to 30 seconds/fiber.

Table 2: Throughput improvements

Parameter	Base	Improved
Resist deposition	MMA – 1.6 nm/min	Styrene – 30 nm/min
Exp. current density	50 nA/cm^2	700 nA/cm^2
Exposure time/probe	20 minutes	50 secs
Beam diameter	1 inch	3.5 inches
Probes/run	**1-2**	**12**

5.4 – Optogenetic targeting and electrical recording using probe prototypes in prosimian primates

The *in-vivo* optogenetic experiments were performed by Dr. Gopathy Purushothaman at Vanderbilt University School of Medicine, where three adult male prosimians were used according to protocols approved by The Institutional Animal Care and Use Committee (IACUC) at Vanderbilt University. The animals were anesthetized and artificially respirated while a craniotomy and durotomy were made over the lateral geniculate nucleus (LGN) and the lateral pulvinar (PL) nucleus of the thalamus at Horseley-Clark co-ordinates of A-P 3 and M-L 7. An injectrode filled with a concentrated preparation (109 iu/ml) of the VSVg-psedotyped lentivirus carrying the CHR2-GFP gene behind the α-CAMKII promoter (Addgene plasmid 15814, FCK CHR2-GFP; UNC Vector core, NC) was then inserted into the region of region of PL containing neurons

and 0.8μL of the virus was injected over 30 minutes. More than 6 weeks after the injection, optrodes were implanted in the brain tissue. The distal end of the fiber was connected to a 100mW DPSS 473 nm laser source (Shanghai Laser and Optics Company Limited, Shanghai, China) with ferrules and a ceramic sleeve (Thorlabs Inc, Newton, New Jersey, US). The electrodes on the optrode were connected to a Blackrock multichannel recording system and the probe was inserted into area V1. Surgical microscope photo (Fig. 5-18) shows cortical penetration by our probe about 1.1 mm inside the cortex. No flexing was observed (in comparison with the yellow reference line) and about 1.5 cm thick agarose embeds the probe, to increase stability.

Neural spikes measured *in vivo* by one channel of a 3-channel probe at a depth of 1173 μm from the cortical surface are shown in Fig. 5-19(a). Results show that the probe sampled activity from three distinct neurons on this channel alone. Spikes were of SNR > 6.0, allowing clear discrimination of the 3 neurons. For comparison, a high-impedance single tungsten electrode was inserted to about the same depth in the same cortical area and spikes were collected and sorted using the same equipment and methods [Fig. 5-19(b)]. The results showed the spikes collected by our probes were of greater amplitude (600mV as compared to 130mV), higher SNR, and allowed for better discrimination of neurons.

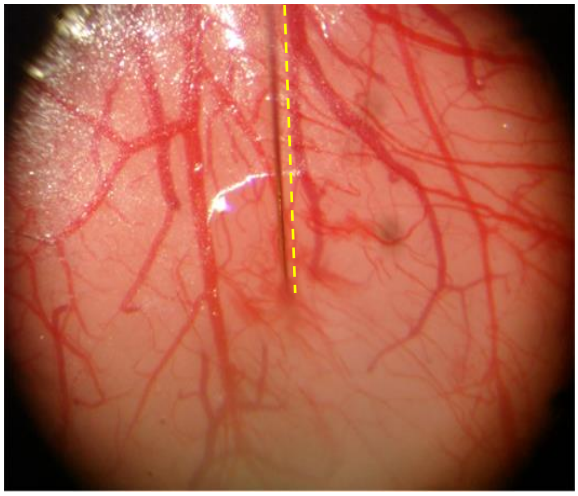

Fig. 5-18: Surgical microscope photo showing cortical penetration.

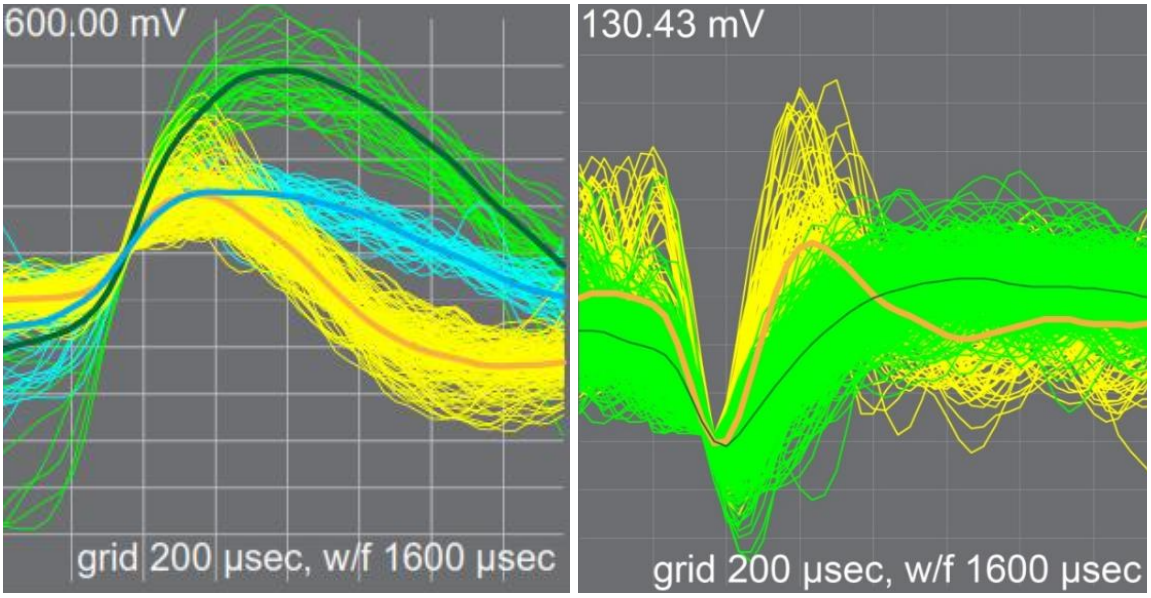

(a) (b)

Fig. 5-19: (a) Spikes collected on 1 channel of a 3-channel probe clearly show 3 distinct neurons. High SNR allowed separation of spike waveforms into 3 units, (b) Spikes collected under similar conditions using a high-impedance commercial tungsten electrode.

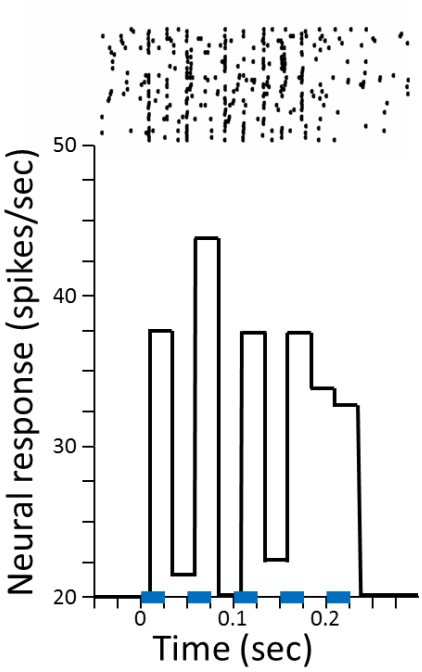

Fig. 5-20: Histogram of the in-vivo neural response to 5 laser pulses.

To test the optogenetic capacity of the probe, the probe was inserted in area V1 of another animal and advanced till layer 5 excitatory cells were found. Fig. 5-20 shows the histogram of the *in vivo* neural response to 5 laser pulses, each 25 msec long, separated by inter-pulse interval of 25 msec and delivered for a total of 250 msec. It can be seen that neurons systematically fired spikes in response to each 25 msec laser pulse, which were time-locked to the laser onset. Blue lines on the time axis correspond to instants when the laser light was switched on.

5.5 – Characterization of Electrode Reliability

Stable, long-term neural interfaces are needed for controlling neuroprosthetics [58]. Recordings of single unit activity within an ensemble of neurons by a silicon multielectrode array enabled a tetraplegic patient to control a robotic arm in 3-dimensions.[58] Over this time, however, the number of recorded neurons (*neuronal yield*)

decreased and overall recording quality declined. Similar failure has been reported for planar silicon probe technology as well.[59] At this time, only the cone electrode[60-65] is capable of producing, stable single unit wave forms in human subjects. Electrode failure can be attributed to abiotic effects, such as corrosion and delamination of insulating films,[67] and biotic effects relating to the response of brain tissue to the implant.[66] Simple electrode impedance measurements have been shown to correlate well with *in-vivo* recording quality, e.g. neuronal yield and signal-to-noise ratio. In a study confirming the functional correlation between large changes in electrode impedance and poor electrode performance, Prasad and Sanchez[12] observed that the overall neuronal yield degraded with very high or very low impedance values. Short-term and long-term factors contribute to changes at the electrode sites. Wear and tear of the electrode interface causes corrosion or delamination that alters the electrochemical properties of the recording surface, and as a result, hampers its sensing and stimulation ability. Thus, in general it is desirable to have stable electrodes that do not corrode, produce stable and repeatable impedance, are robust after repeated implantations with long periods of current delivery, and are reliably reusable. Finding the optimal balance of all these design considerations is both challenging and required for efficient electrode performance.

Our first probes were fabricated directly over the polyimide buffer layer of the optical fiber substrates. We found such extensive delamination of this layer in saline that most of the probes failed during initial impedance testing and, while some did yield high quality *in-vivo* recordings, polyimide delamination caused *all* of the probes to fail as they were retracted from the measurement site. In an effort to solve this problem, we now strip the polyimide jacket, replacing it with the cross-linked plasma deposited styrene

layer discussed above. This section describes the reliability of single channel probes fabricated with the new process.

Initially, a batch of 4 probes was fabricated as described in Chapter 4 Section 4.4. Two of the 4 probes had very low impedance which was traced in incomplete removal of the gold layer by the planar diode etching system then in use. An ion mill was refitted to provide a more reliable etching process for these 3-D structures. Preliminary characterization of the ion mill is discussed later in the Chapter in Section 5.6.

Experiment 1: One of the low impedance (non-functional) probes was inserted a) 6 times to a depth of 1.5″ in agarose gel to simulate implantation in nerve tissue, and b) 5 times into a stainless steel cannula. The probe surface was inspected for physical damage by scanning electron microscopy after each test.

Experiments 2-4 were carried out sequentially on Probe 1. Overall, this probe experienced 21 days in 0.9 % saline or PBS, 11 days of which were carried out at a constant current density of 6.0 mA/cm^2 at 1 kHz.

Experiment 2: The impedance of Probe 1 was measured continuously at 1 kHz frequency and a test current density of 6.0 mA/cm^2 over a period of 11 days. Impedance was measured 9 times as a function of frequency during the experiment. This test studies the effects of the measurement process on the impedance and the impact of mild stimulation on probe lifetime. After testing, the probe was rinsed in DI water and its impedance compared with the initial values at several frequencies.

Experiment 3: Probe 1 was inserted 6 times to a depth of 1.5″ in agarose gel to simulate implantation in nerve tissue. Impedance was measured before and after the experiment.

Experiment 4: Impedance was again measured on Probe 1 as a function of frequency on 10 consecutive days. In this case, the probe was immersed in phosphate buffered saline (PBS) at body temperature (37^{o} C) for the entire time but no test current was applied between measurements. Statistical analysis of the measured impedance was carried out using commercial software.

5.5.1 – Materials and Methods

Agarose gel was prepared[56] using 60g of Agar powder (Landor Trading Co.) in 100 mL of phosphate buffered saline solution (PBS). A 23 gauge, 304 stainless steel hypodermic tube (0.003" ID) was used for the cannula tests. Fibers were inserted into the cut end as supplied by the manufacturer. No additional polishing or deburring was carried out.

Fig. 5-21: Probe inserted in Agar gel 6 times to a depth of 1.5 inches.

A Leo 1525 scanning electron microscope was used to inspect the probe surfaces. Impedance was measured using a Metal Electrode Tester (Model IMP-2) from Bak

Electronics. The test current density was 20 nA. A 30 gauge silver wire was used as the reference electrode. Testing was carried out in 0.9% saline at room temperature in Experiment 2 and in PBS at body temperature (37^{o} C) in Experiments 3 and 4. Figure 5-21 shows the tip of the probe inserted in agar (red line is a reference).

5.5.2 – Results

Experiment 1: Implantation tests in Agar and the steel cannula revealed interesting properties about the insulation. Figures 5-22 shows a probe a) before and after b) the agar implantation and cannula insertion tests. The micrographs do not indicate any physical damage to the probes.

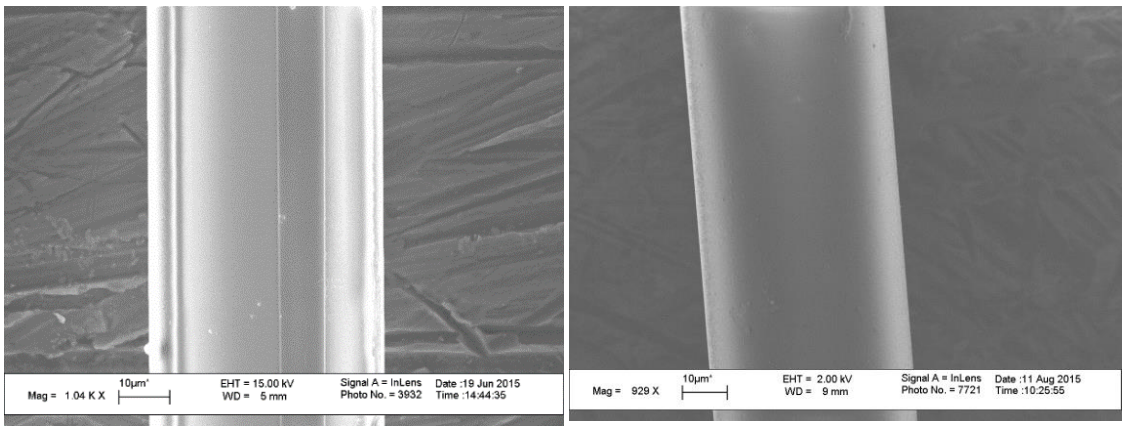

(a) (b)

Fig. 5-22: A probe a) before and after b) the agar implantation and cannula insertion tests.

Figure 5-23 shows impedance vs frequency for contacts from the two functional probes. A third line denoting the standard impedance model[53] for the corresponding contact area is also shown and it can be seen that the experimental plots agree well with the theoretical plot. This shows that electrical leakage through the cross-linked styrene overcoat is

insignificant compared to the 320 μm^2 area of the contact. The initial impedance measurements provided a good reference that was verified at the end of each testing procedure. Figure 5-24 shows impedance trends as a function of measurement time in Experiment 2. Impedance reaches a maximum value after about 4 days and remains constant thereafter.

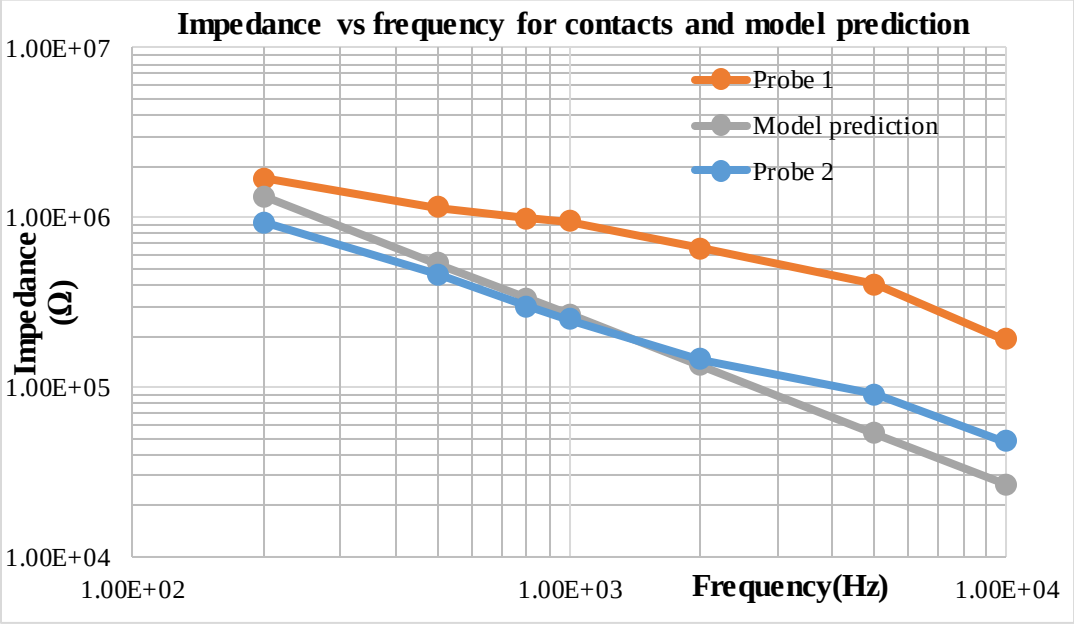

Fig. 5- 23: Impedance vs frequency for two as-manufactured probes and the standard impedance model.53

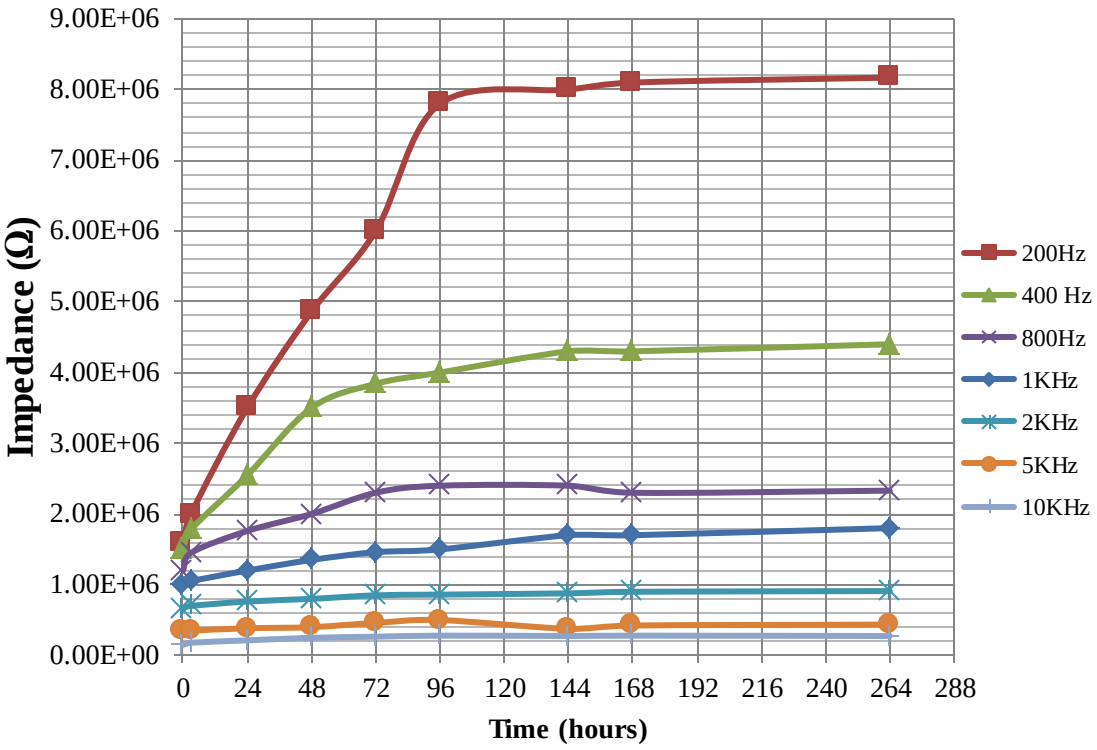

Fig. 5-24: Daily impedance measurements as a function of frequency over a period of 11 days in Experiment 2.

While the increase in impedance at lower frequencies would cause some distortion of recorded spikes, the 1 kHz impedance is relatively stable and would likely produce stable neuronal yield. Fig. 5-25 shows impedance as a function of frequency for the as-manufactured probe, after the DI-rinse at the end of Experiment 2 (11-day spectroscopy), and after the DI-rinse after agar implantation (Experiment 3). The rinsing step in Experiment 4 clearly restores the probe to pristine, original condition. Moreover, there is no electrode or insulator damage after the agar gel insertion.

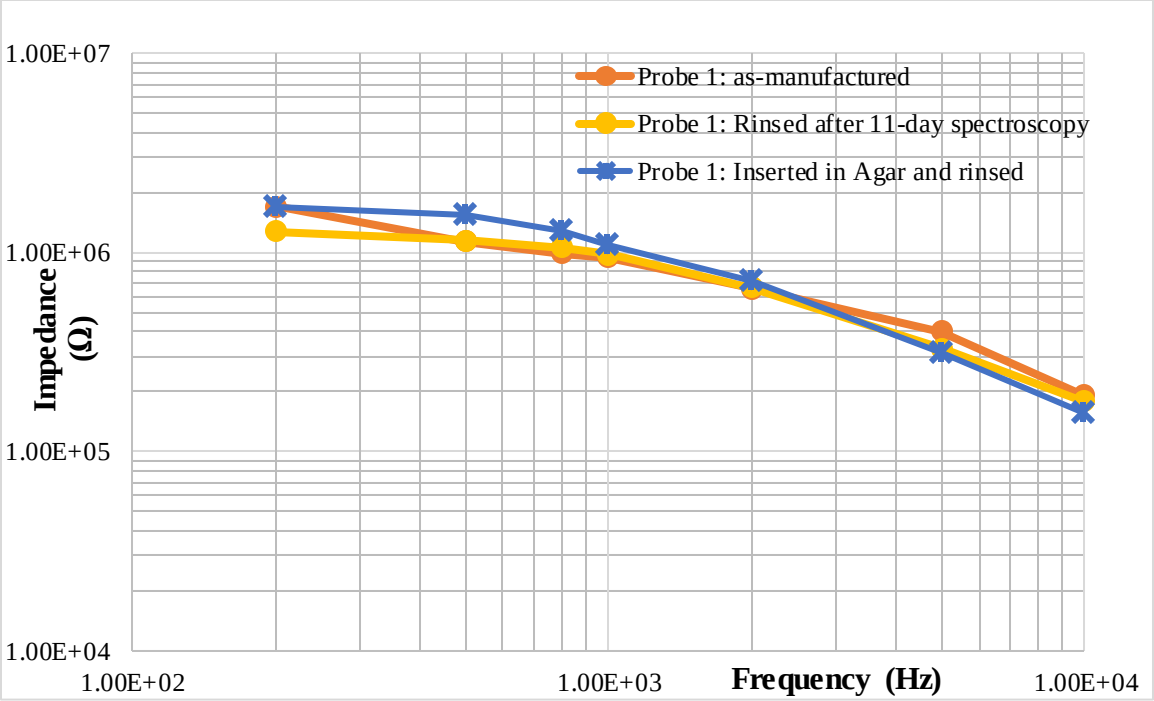

Fig. 5-25: Impedance measurement for as-manufactured probe (orange), after rinsing the probe in de-ionized water following the 11-day implantation experiment (Experiment 2-yellow) and after insertions in Agar gel followed by de-ionized water rinse (Experiment 3-blue).

5.2.3– Statistics of Variation

Electrophysiology statistics show the day-to-day impedance trend which is useful in determining the consistency of measurement. An immersion test in 1X solution of phosphate buffered saline (PBS) was used to study the trend for 10 days (Experiment 4). The solution was maintained at a temperature of 37ºC using a Cole Parmer Thermo Scientific Digital Water Bath that provides $\pm$0.1ºC, to observe the effects of body temperature. Figure 5-30 shows the setup used for this set of measurements. A silver reference wire was immersed in the PBS solution along with the probe, each connected to the respective connector on the Metal Electrode Impedance Tester (Model IMP-2) from Bak Electronics. Impedance was recorded at every frequency eight times daily and was rinsed between every consecutive measurement.

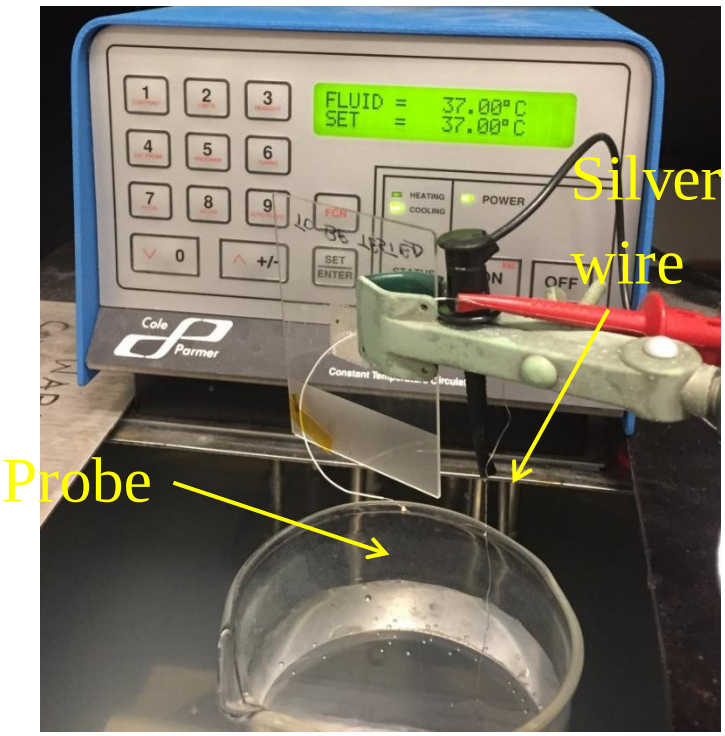

Fig. 5-26: Impedance measurement setup for probe immersed in warm PBS solution maintained at 37ºC using a water bath.

This process was repeated for 10 days and statistical analysis was carried out on readings at each frequency using JMP, a statistical discovery software from the Statistical Analysis System (SAS) company. We obtained variability charts for all the frequencies, which have been highlighted in further sections. As an illustration, the charts for 1 kHz are shown here in order to simplify the overwhelming data and also, since in traditional neurophysiology experiments, magnitude impedance is generally measured at 1 kHz to test for electrode patency.[54] Figure 5-31 (a) shows the variability chart as plotted using JMP showing day-to-day variation and error bars in each set of measurement with the help of box plots.

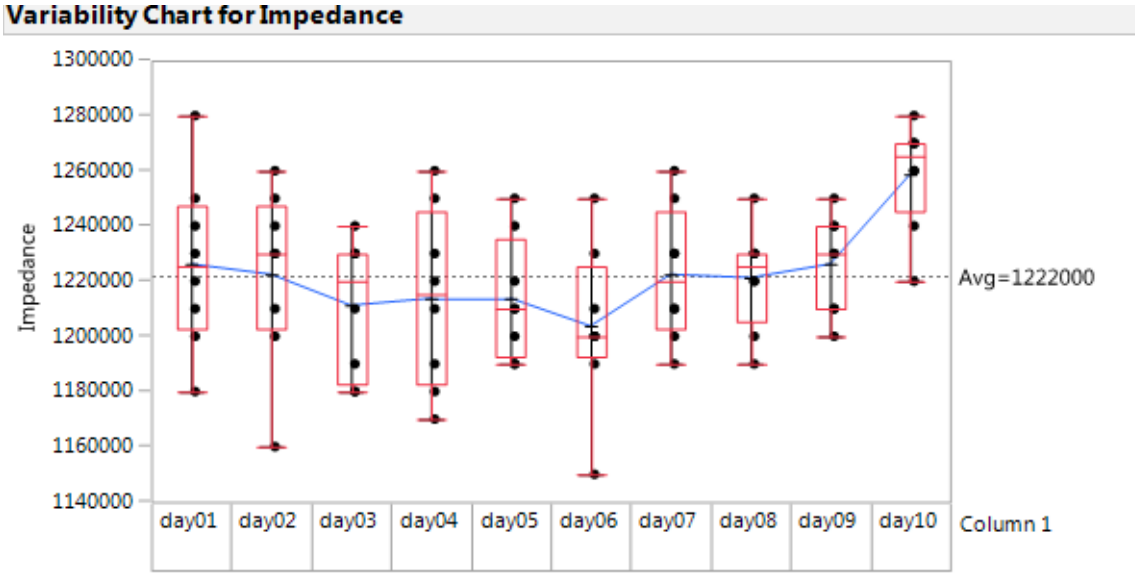

(a)

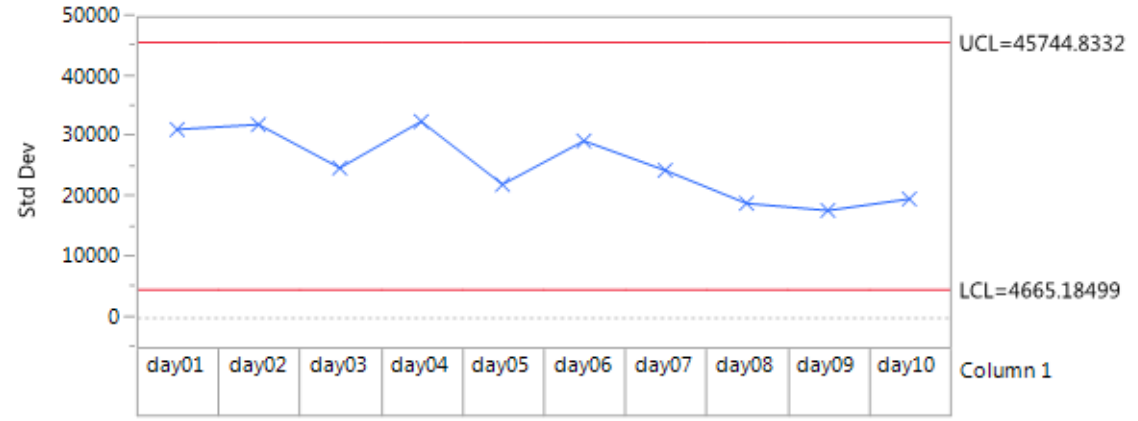

(b)

Fig. 5-27: (a) Variability chart using JMP showing day-to-day variation in impedance (1 kHz). (b) Standard deviation calculation for each day (1 kHz).

Box plots are represented in terms of quantiles, which are boundaries between data sets. 100-quantiles or percentile is defined as the value of a variable below which a certain percent of observations fall. The box plot has four quartiles (each representing a fourth), as shown in Fig. 5-32. The computed average is 1.2 MΩ for the frequency of 1 kHz as

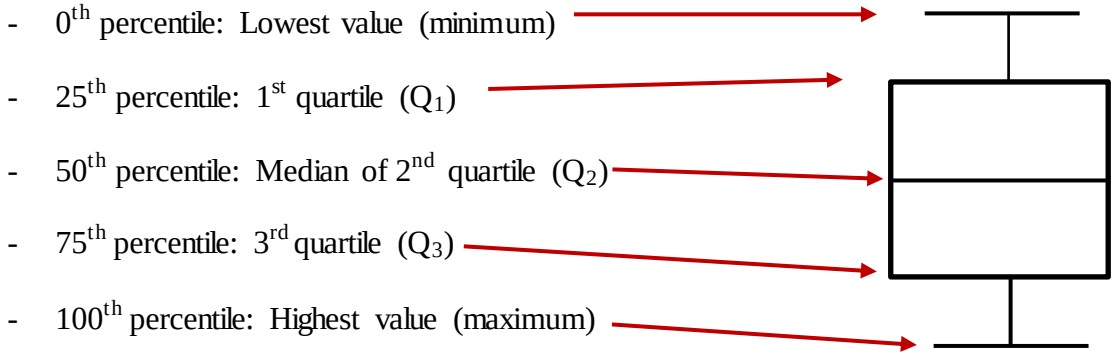

Fig. 5-28: Anatomy of a box plot

shown by the dotted line in Figure 5-31(a). The blue line represents the trend of the means and their respective deviation from the population average. This variability chart is obtained by conducting a Gauge R&R study, which is a standard for addressing repeatability/consistency when an item is measured several times. It quantifies capabilities and limitations of the measurement system by estimating repeatability (variation due to device) and reproducibility (variation due to operator) when conditions of measurement are fixed; in this case temperature, reference material etc. Subtle variations are inherent to any measurement system, but existence of special cause variation is gauged by the absence of a sidewise overlap between any two datasets. As can be seen from Fig. 5-31(a), if any two datasets are selected at random, there would always be an overlap between them. Fig. 5-31(b) denotes the variation in day-to-day standard deviation. The red bars denote the upper and lower specification limits which will be explained in the following section. These are control limits within which the process can be assumed to be stable so long as the data points are within the boundaries.

Statistical process control is a typical measurement based type of control mechanism for monitoring process performance on a sample-by-sample basis. By plotting the quality characteristic as a function of sample number, it helps to determine if the process is "in control" and identify any subtle "out of control" conditions. Since our data is continuous and contains individual measures, we adopted the use of an IR (Individual Range) chart for the process analysis. Figure 5-33 shows the IR chart (impedance vs sample number) along with the previously mentioned upper and lower specification limits. The green line represents the average of the entire population, and the UCL (upper control limit) and

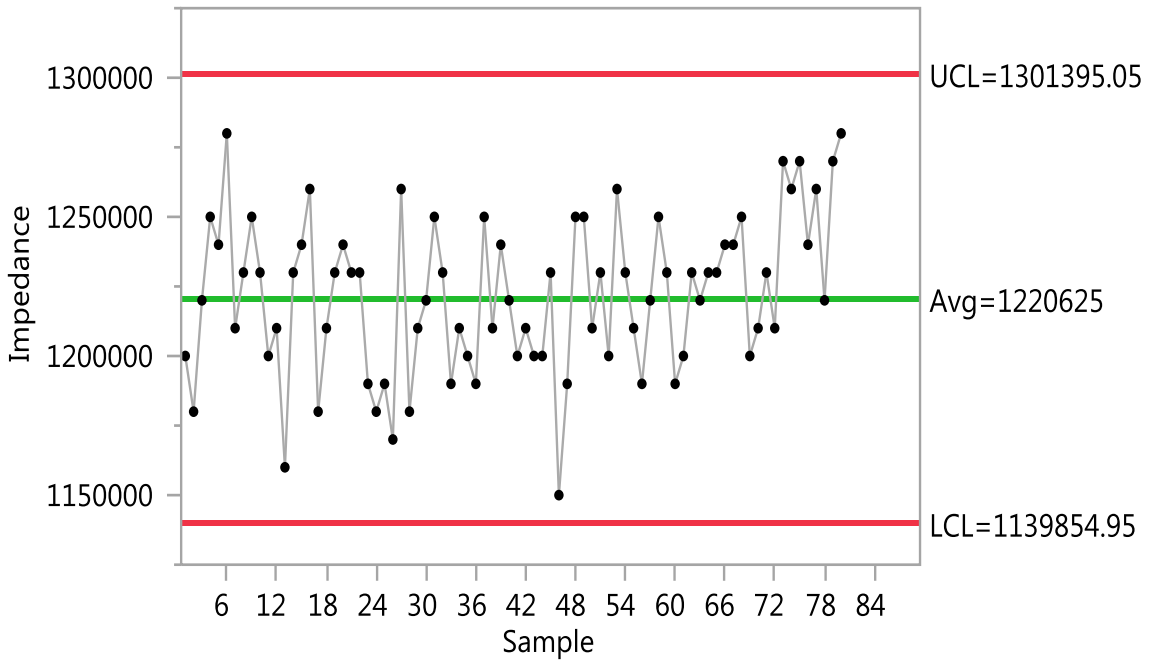

Fig. 5-29: Individual Range (IR) chart for observing sample-by-sample variation (1 kHz).

LCL (lower control limit) denote ±3 standard deviations respectively. For a process that has a normal distribution, 99.7% of the population is captured by the curve at three standard deviations from the mean. There being no measurement value beyond 3 standard deviations in our data graph, indicates that the process is stable and has less variation.

The process is said to be “out of control” when data points exhibit systematic or nonrandom behavior as elaborated in the AIAG Manuals for SPC and Nelson rules[55]. The rules have been universally accepted for drawing conclusions about stability of the process and data. Our data indicates subtle variations in day-to-day values, but no “out of control” or absurd behavior. Subtle variations are thought of as natural variations which, in most cases are inherent to the system of measurement. Statistics data for all other measured frequencies (200 Hz, 400 Hz, 800 Hz, 2 kHz, 5 kHz and 10 kHz) is shown in Figures 34 - 45 for reference.

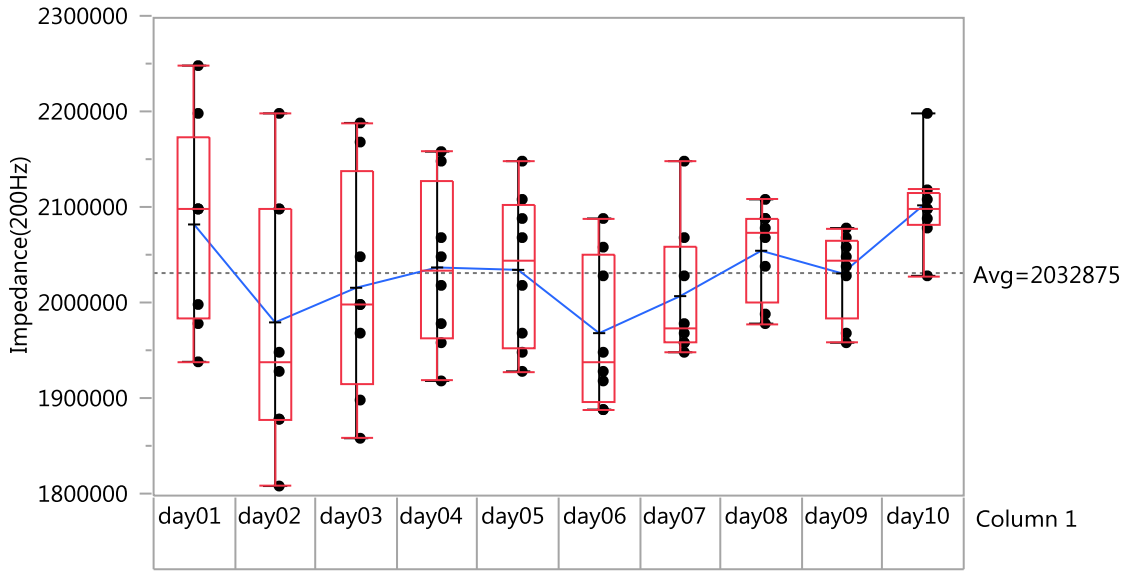

(a)

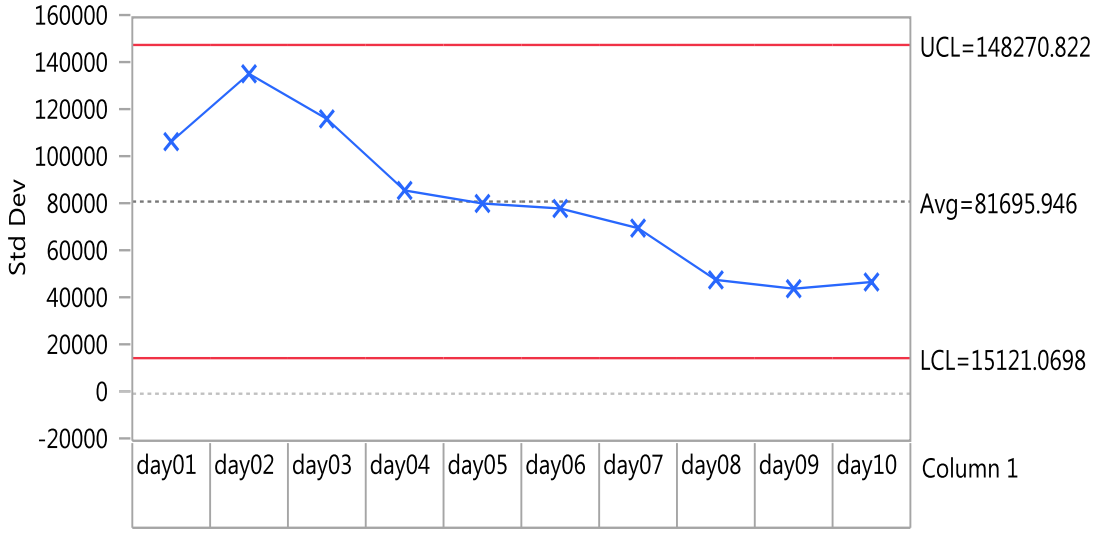

(b)

Fig. 5- 30: (a) Variability chart using JMP showing day-to-day variation in impedance (200 Hz). (b) Standard deviation calculation for each day (200 Hz).

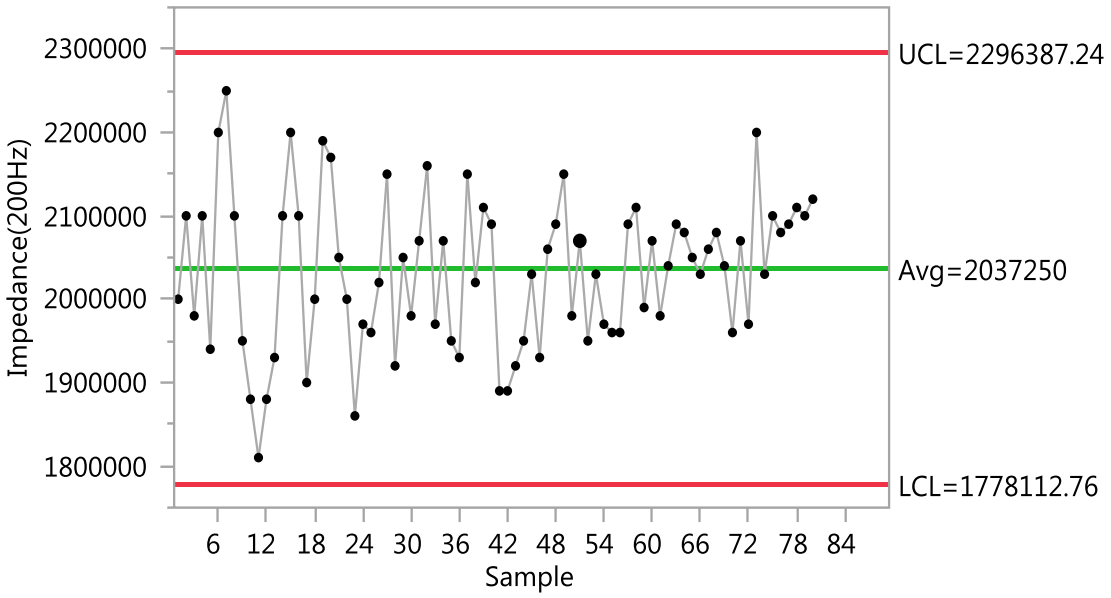

Fig. 5- 31: Individual Range (IR) chart for observing sample-by-sample variation (200 Hz).

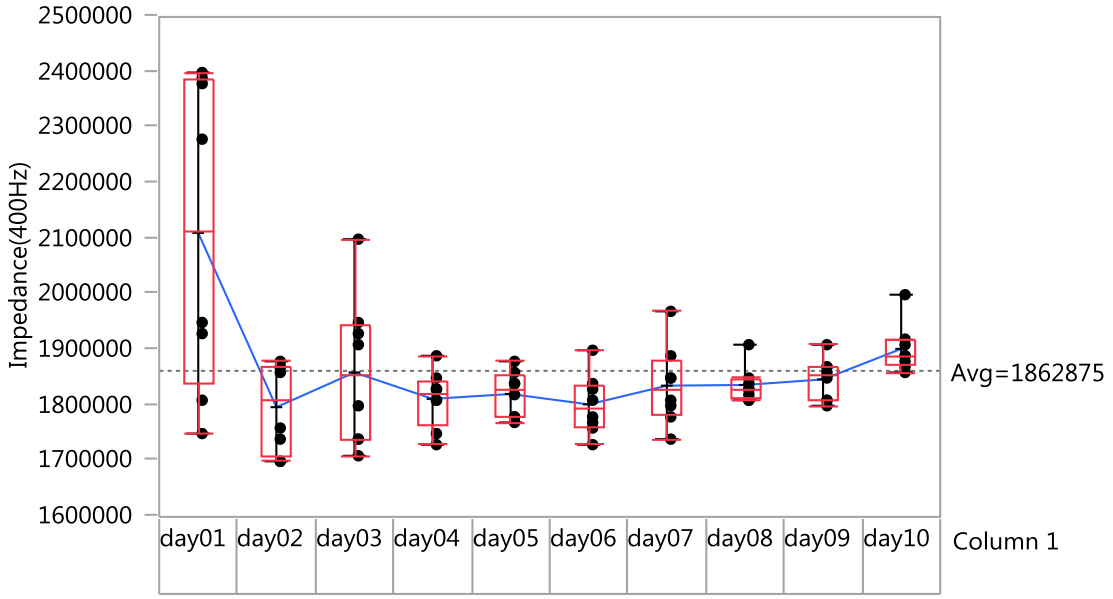

(a)

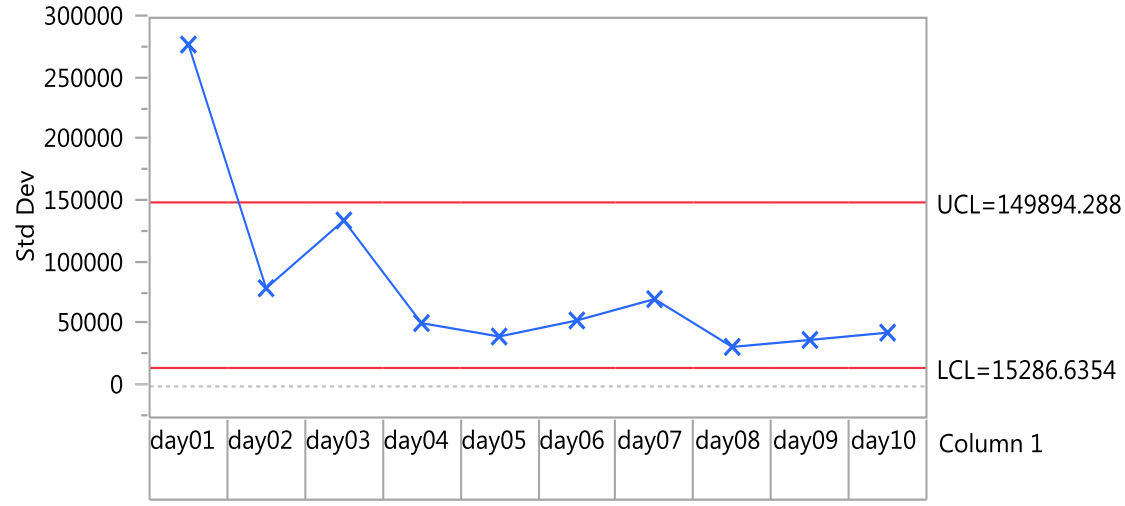

(b)

Fig. 5- 32: (a) Variability chart using JMP showing day-to-day variation in impedance (400 Hz). (b) Standard deviation calculation for each day (400 Hz).

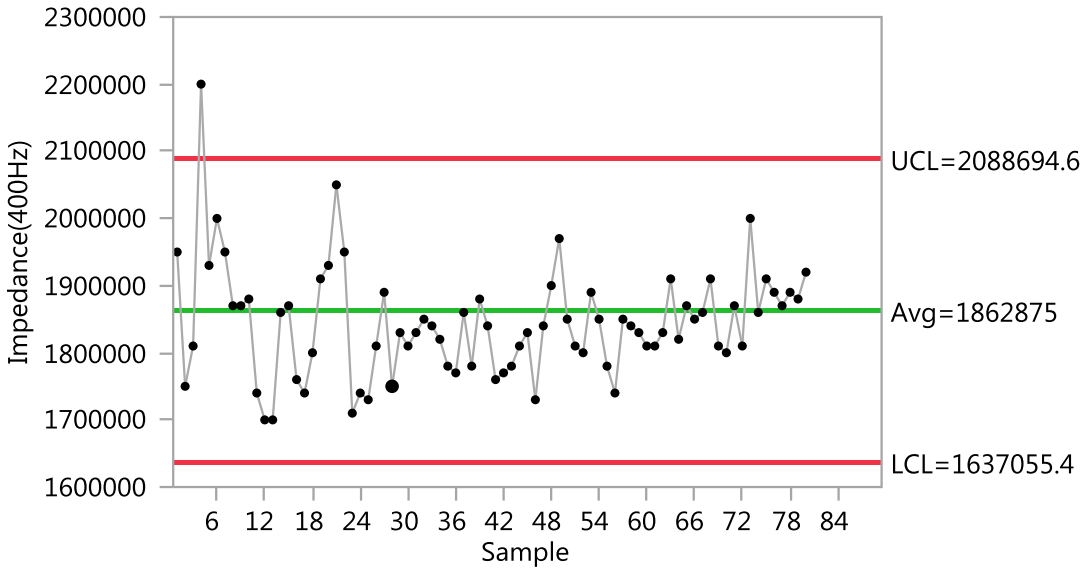

Fig. 5- 33: Individual Range (IR) chart for observing sample-by-sample variation.

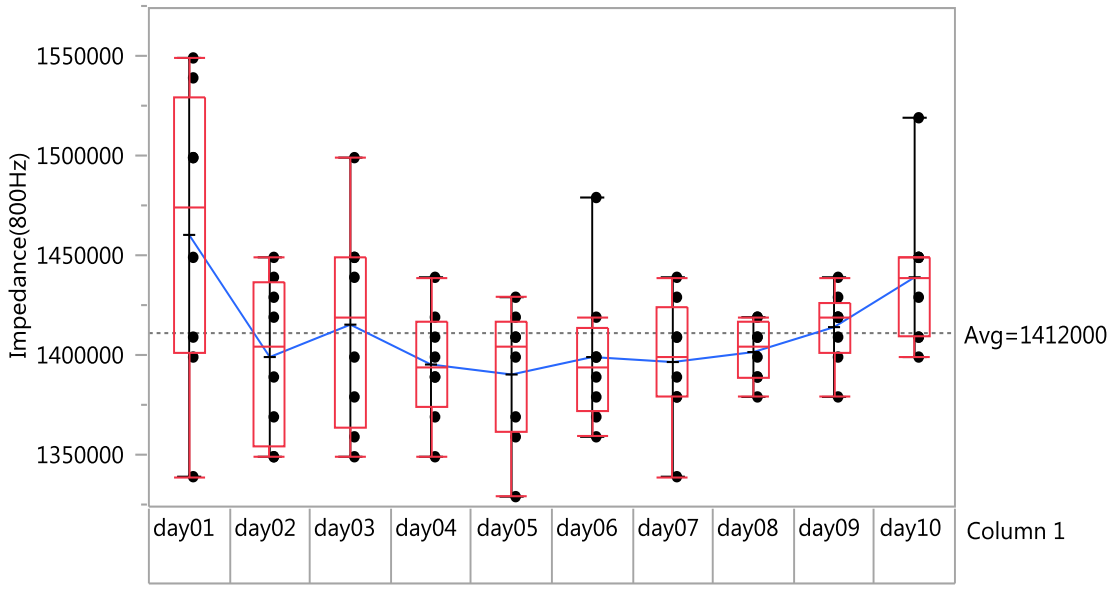

(a)

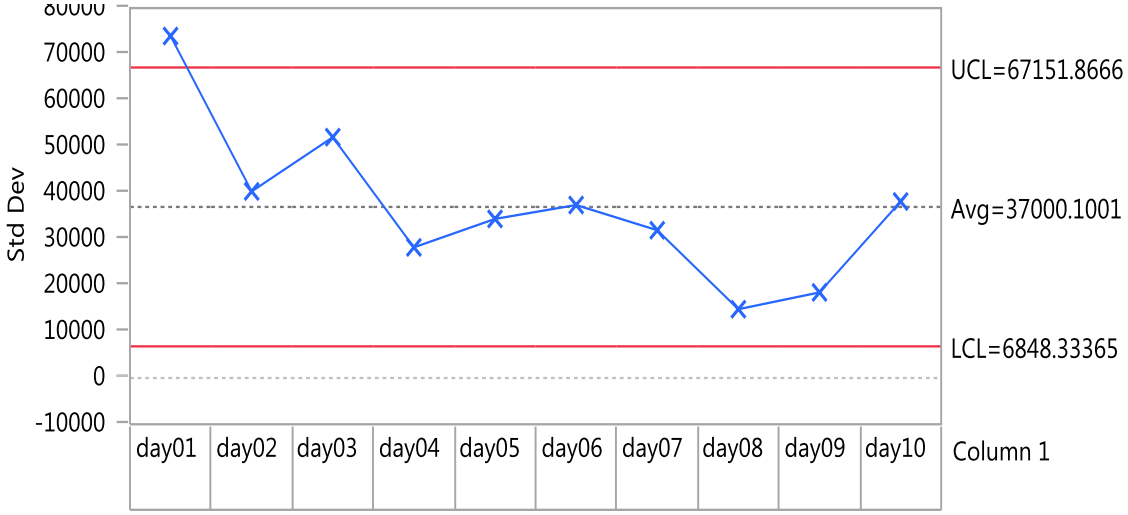

(b)

Fig. 5- 34: (a) Variability chart using JMP showing day-to-day variation in impedance (800 Hz). (b) Standard deviation calculation for each day (800 Hz).

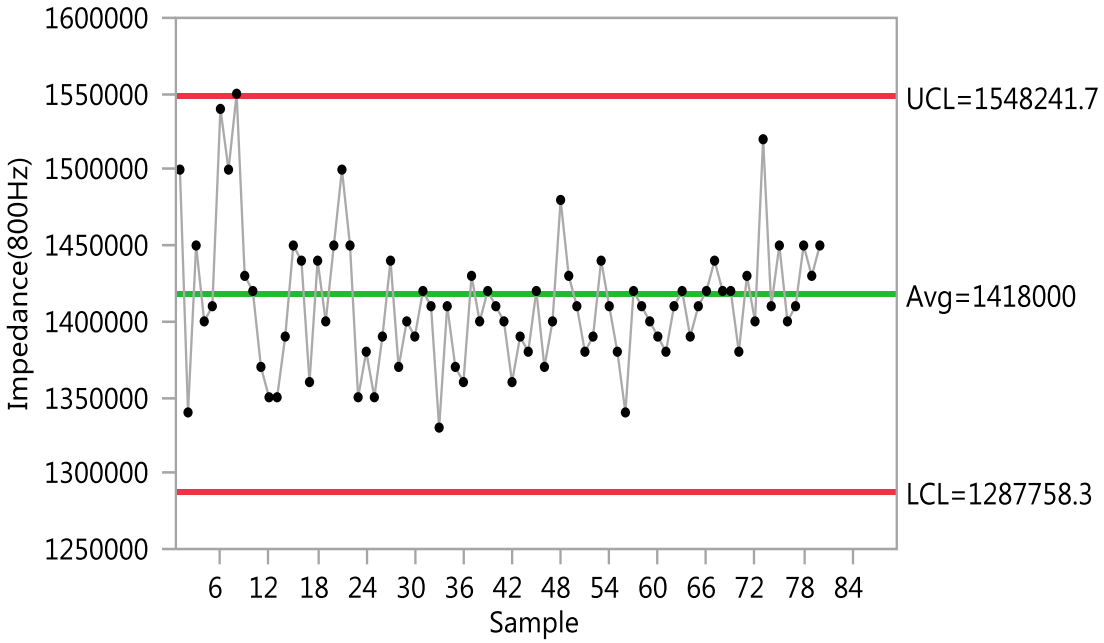

Fig. 5- 35: Individual Range (IR) chart for observing sample-by-sample variation (800 Hz).

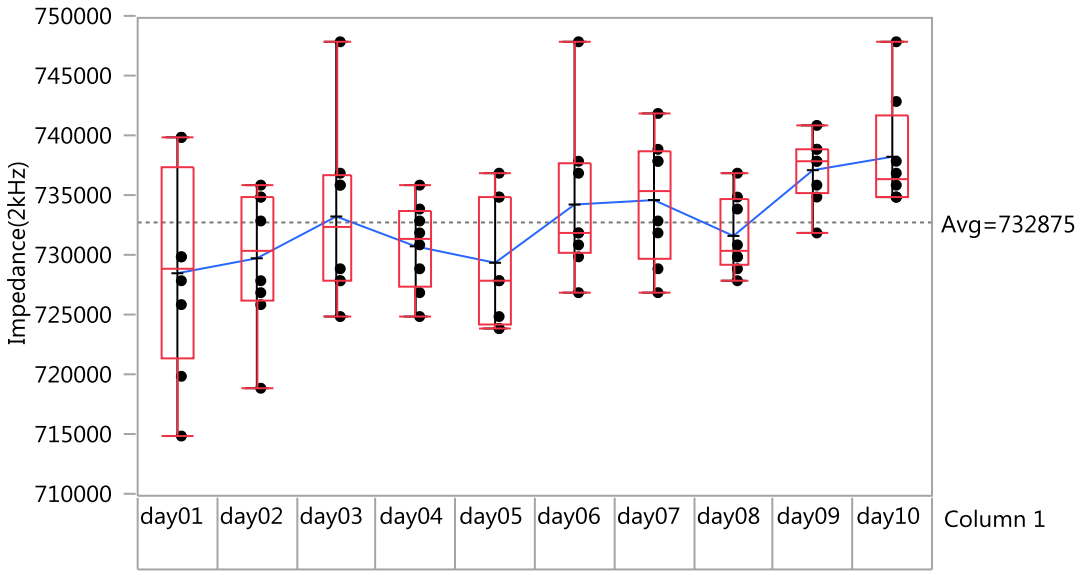

(a)

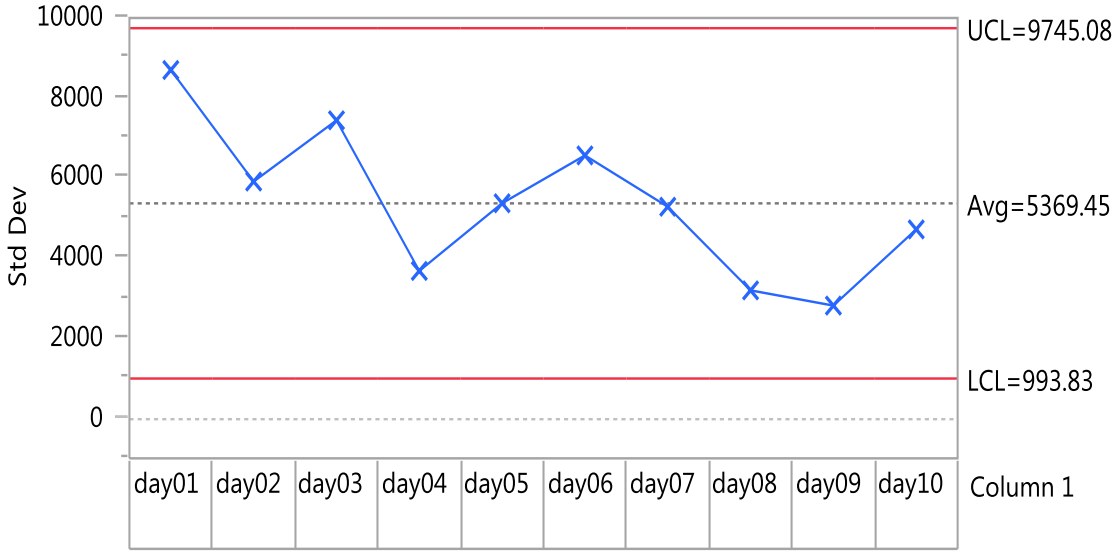

(b)

Fig. 5- 36: (a) Variability chart using JMP showing day-to-day variation in impedance (2 kHz). (b) Standard deviation calculation for each day (2 kHz).

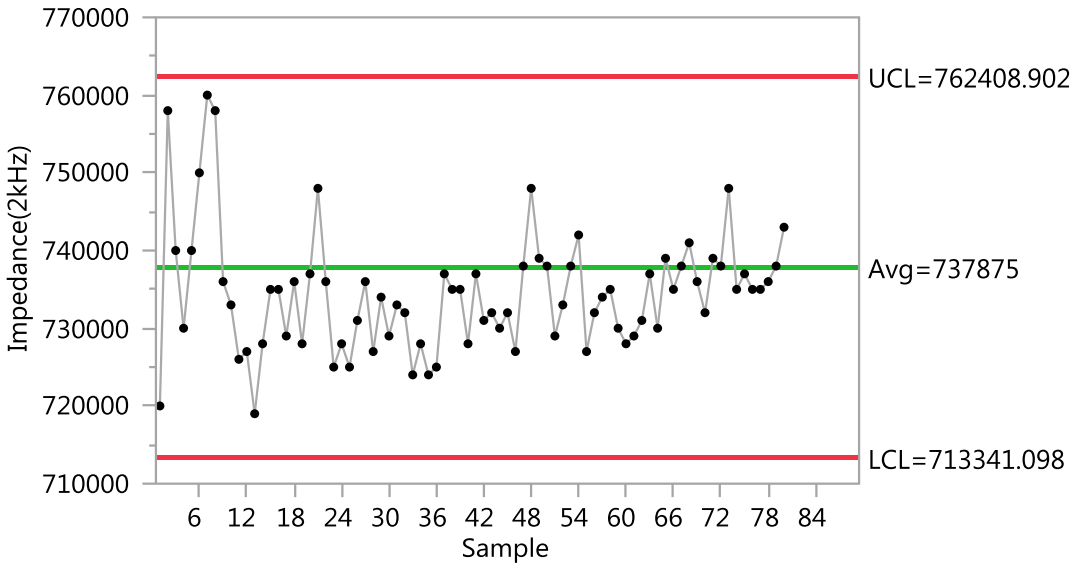

Fig. 5- 37: Individual Range (IR) chart for observing sample-by-sample variation (2 kHz).

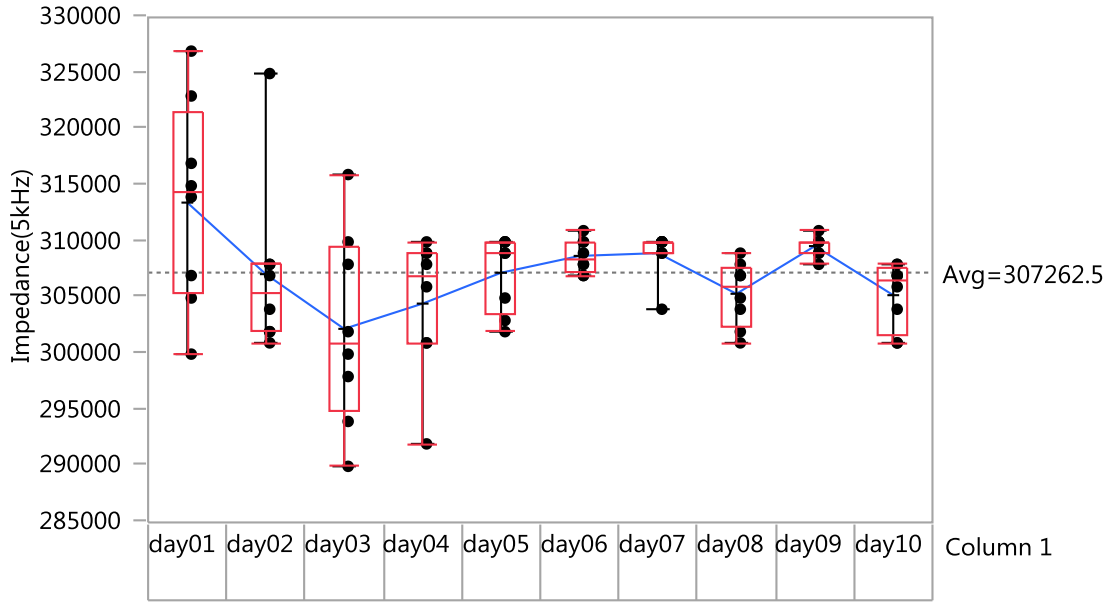

(a)

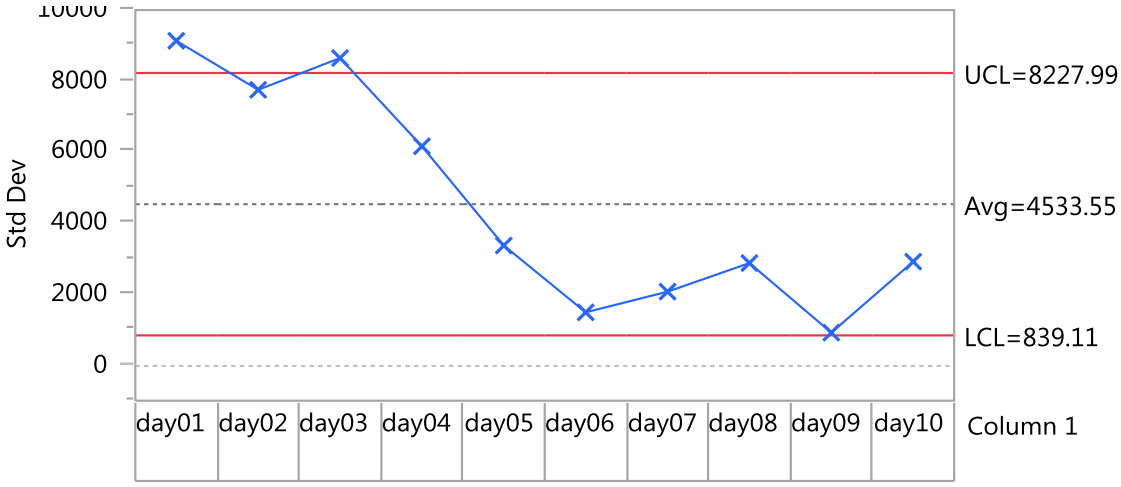

(b)

Fig. 5- 38: (a) Variability chart using JMP showing day-to-day variation in impedance (5 kHz). (b) Standard deviation calculation for each day (5 kHz).

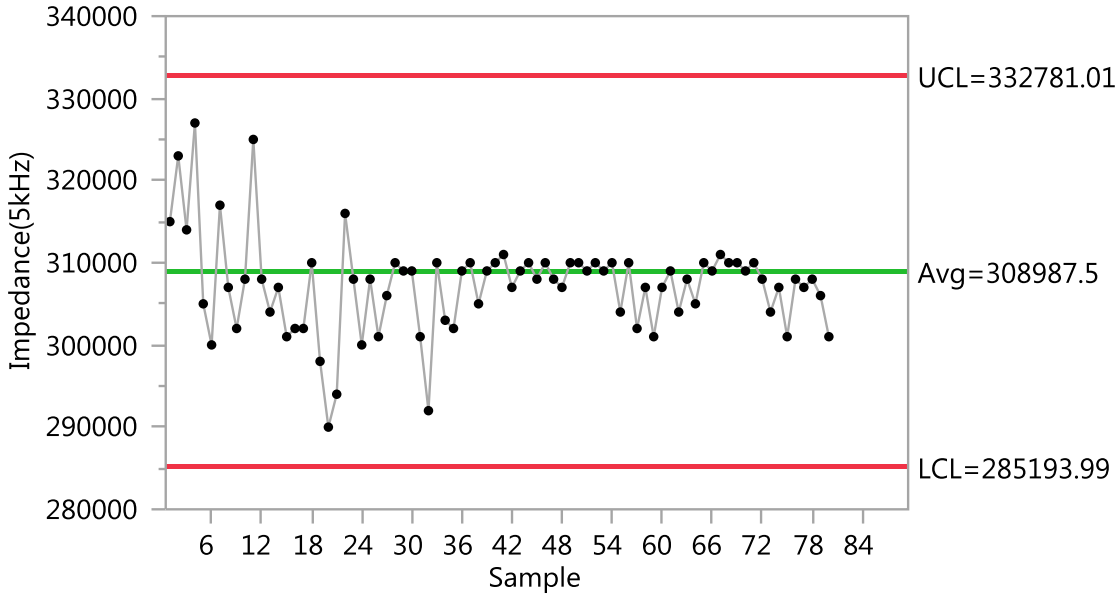

Fig. 5- 39: Individual Range (IR) chart for observing sample-by-sample variation (5 kHz).

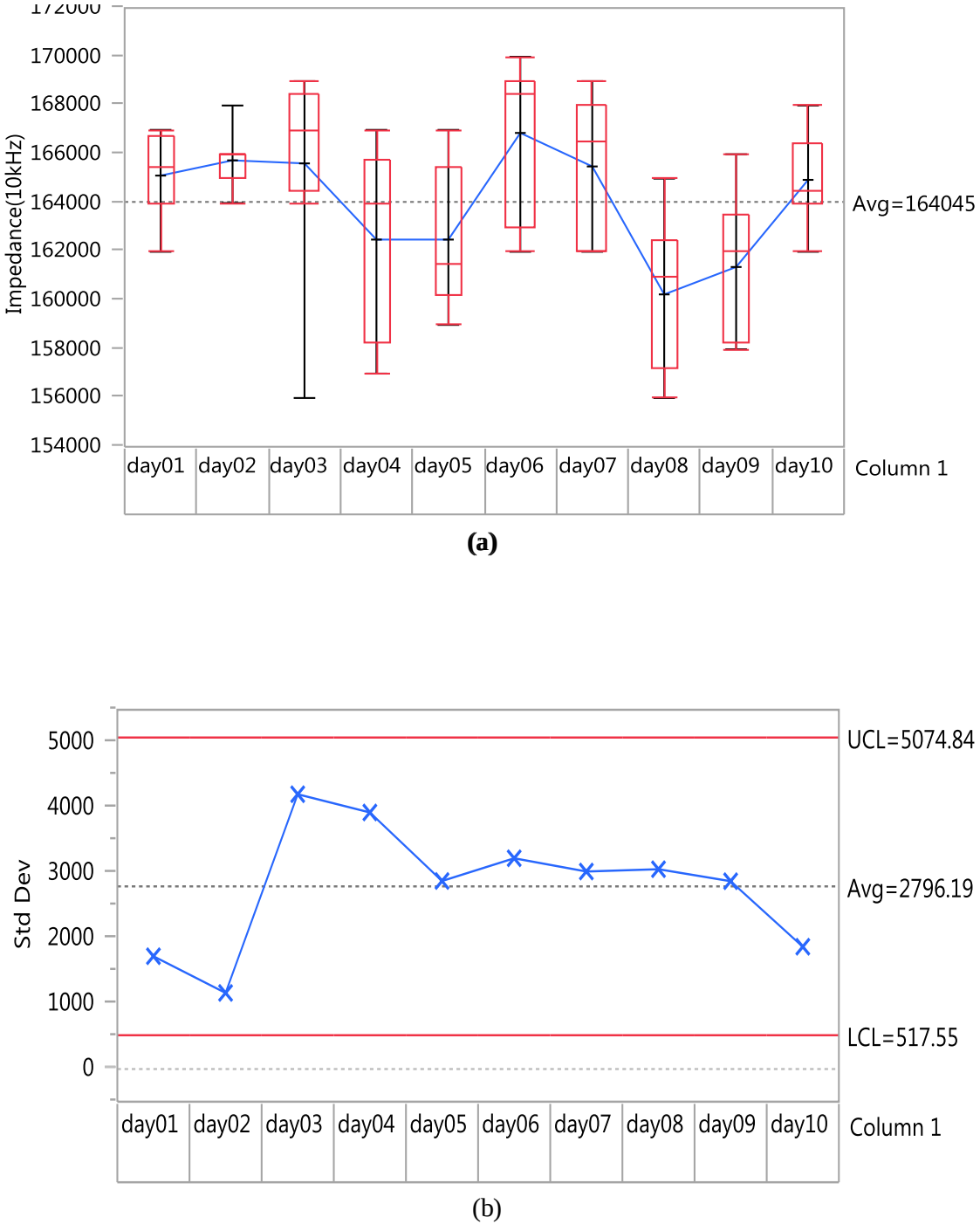

Fig. 5- 40: (a) Variability chart using JMP showing day-to-day variation in impedance (10 kHz). (b) Standard deviation calculation for each day (10 kHz).

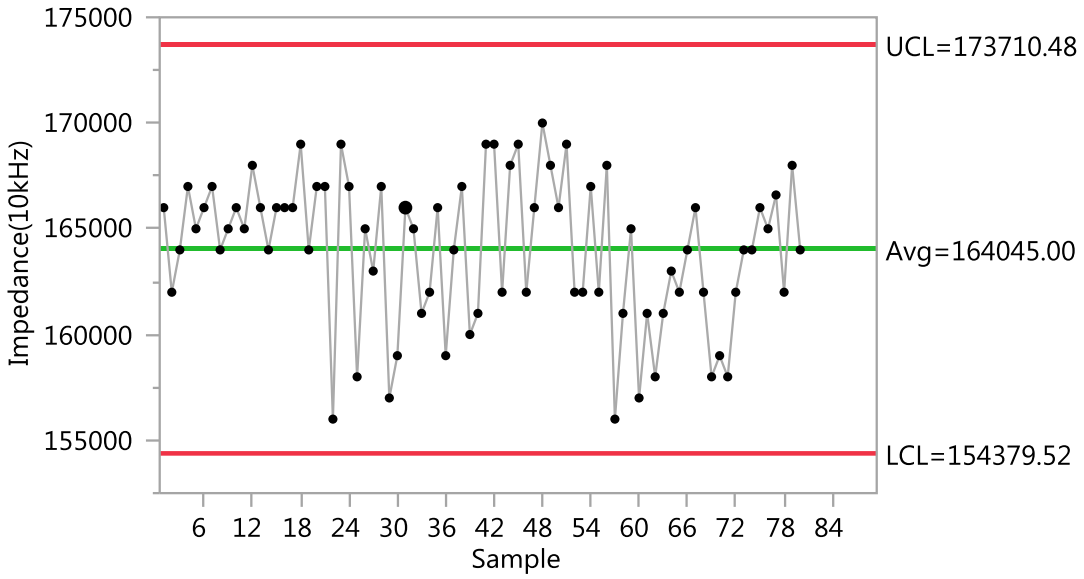

Fig. 5- 41: Individual Range (IR) chart for observing sample-by-sample variation (10 kHz).

5.6 – Failure Analysis

It is important from the manufacturing standpoint to have a process that not only facilitates high throughput, but delivers high yield results. Out of 5 probes that were tested for impedance analysis, three failed to comply with the expected trends thus giving us a 40% yield which has room for improvement. The failed probes were studied for possible reasons for the breakdown, by means of scanning electron microscopy (SEM) characterization. The observed value of impedance was very low, possibly indicating a short circuit or an infinitely large area of the conductor in contact with the electrolyte. Figure 5-46 shows micrographs of the conductor lines and probe surfaces after they were tested using the saline solution like the others in the batch. It is evident from the images that the etching process failed to clean the gold layer around the conductor line, which could be a potential reason for the breakdown of the probes in saline. The issue with the etching process can be attributed to the limited coverage in the sputter etching tool as a

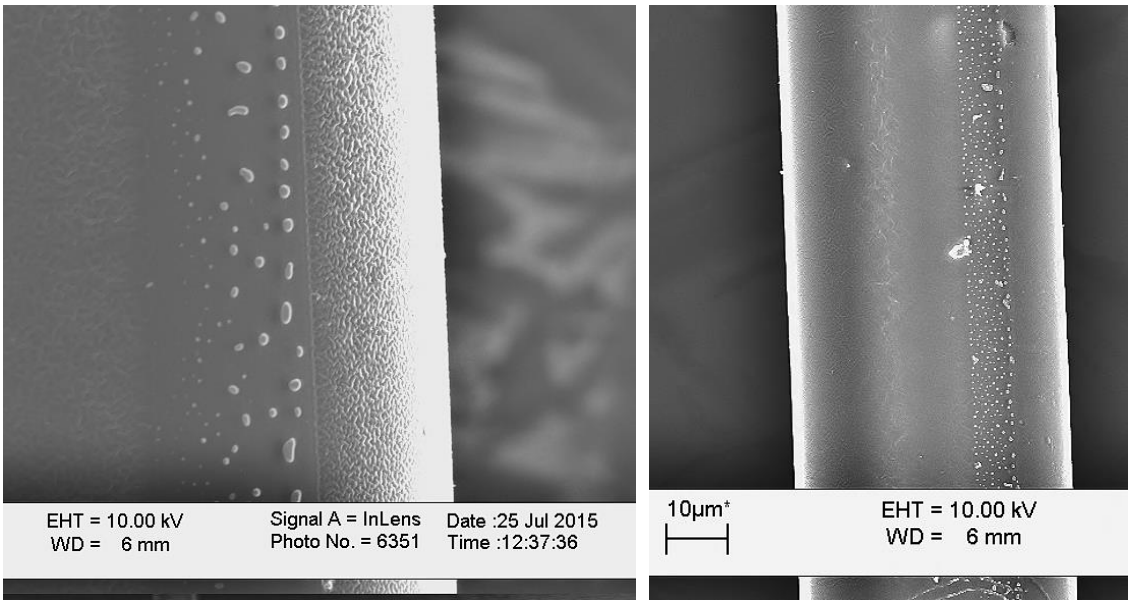

(a) (b)

Fig. 5- 42: Conductor lines and probe surface of failed probes (a) remaining gold in the surrounding area. (b) spotty conductor line due to poor etching of resist.

result of which some portions of the probe surfaces remained un-etched. In order to solve this problem of unreliable etching, we decided to adopt a new process – ion beam milling for the etching of gold and styrene. An ion beam milling tool was dxeveloped and further characterized for the etch process.

5.6.1 – Ion Beam Milling Tool and Process Development

The use of broad beam ion sources for modifying film properties has the ability to modify and reproducibility control film properties. Ion bombardment allows independent variation of individual parameters like ion energy and ion flux. Also, since the plasma is contained in the ion source, the etching environment is much simpler near the substrate. Lastly, ions are accelerated into a beam with a well-defined and controlled direction, density and energy, thus facilitating easy process and etch-profile definition. The ion

milling tool at the Nanosystem Manufacturing Center (Fig. 5-47) features a 3 cm DC filament cathode with a filament neutralizer and is powered using Ion Tech MPS-3000FC Ion Source Power Supply. A base vacuum of 10^{-8} to 10^{-7} is obtained using a dry pump

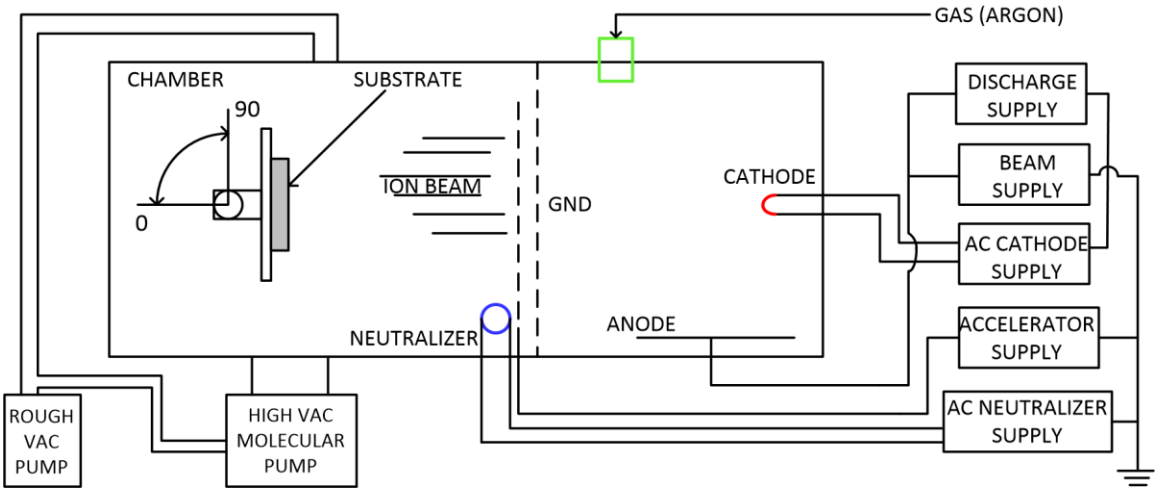

(a)

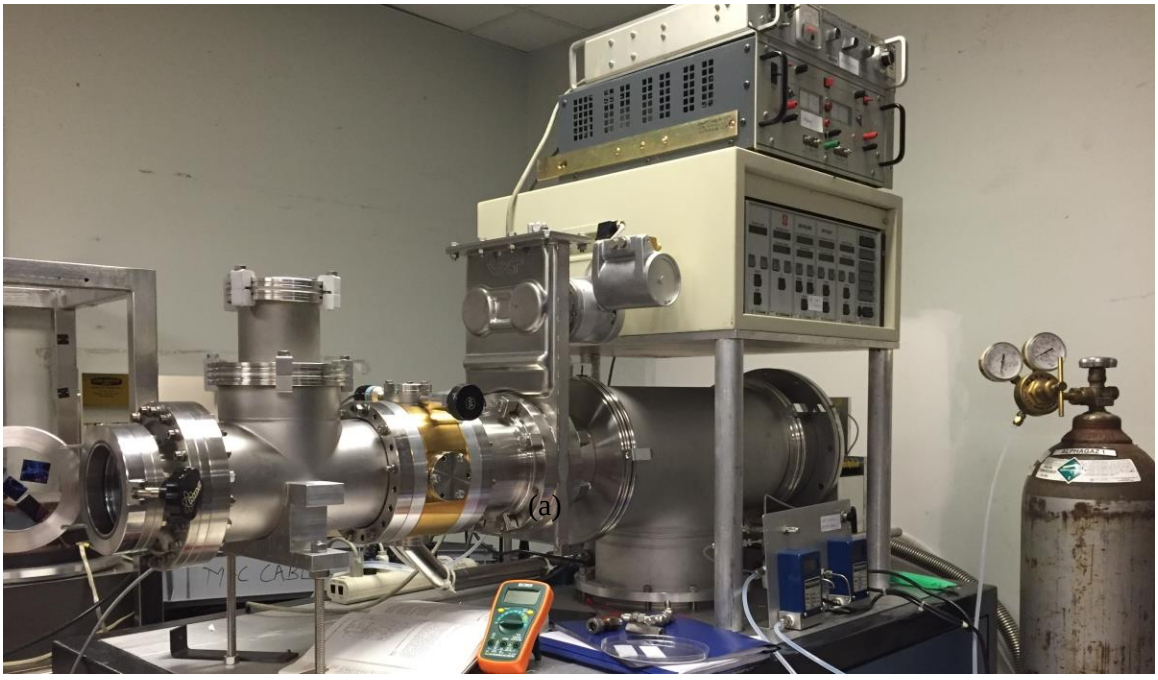

(b)

Fig. 5- 43: (a) Schematic diagram of ion mill system. (b) Physical picture of the tool.

(Ebara) and a cryogenic turbo pump. A working pressure of 10^{-5} is typical while the gas is flowing to produce the ion beam. The discharge chamber plasma within which the Argon ions are created is at a potential close to that of the anode. A magnetic field is used to contain the electrons and increase the ionization efficiency. Upon being accelerated into the ion beam using a negatively biased accelerator grid, the ions acquire an energy corresponding to the beam supply energy and correspondingly, the ion current equals the beam supply current. Electrons are introduced in the chamber in order to balance the positively charged ions by placing a neutralizer filament after the accelerator grid. The ions travel down the 1.2 m long beamline and impinge on the substrate at the areas that are unmasked and need to be etched. It is an anisotropic etching process that faithfully transfers the mask pattern onto the substrate. We characterized the ion beam milling tool with regards to etch rate for crosslinked styrene and gold. The rate obtained for styrene is 6-7 nm/minute, whereas that for gold is 10-12 nm/minute. Thus, we observed an etch selectivity of about 2:1. The obtained rates were achieved using the condition shown in Table-3. A current density of 1.1 mA/cm^2 was obtained with a beam diameter of 3″. The time taken by the etching step in the overall process flow has also been reduced by a factor of 8 due to lower pump down time in the new system.

Table 3: Operating conditions developed for ion beam milling technique.

Cathode Current (A)	Filament current (A)	Filament voltage (V)	Emission current (mA)	Accelerator voltage (V)
1.28	0.22	55	24	100

Chapter 6 – Summary and Future Scope

6.1 – Summary

In conclusion, a promising ground has been established for the manufacturing of a family of novel *optrodes,* with thin film electrode patterns on fine needle-like substrates for simultaneous optical stimulation and electrical recording from a localized region of genetically targeted neurons with millisecond temporal precision. They provide the design flexibility of planar probes in the cylindrical format required for deep brain applications. The critical requirements that have been addressed are (a) conformal thin film deposition of resist and conductor material on the substrate, (b) micron-scale alignment and patterning of fiber substrates to a stencil mask, (c) high throughput and reliable manufacturing of *optrodes,* and (d) desired contact impedance with repeated functionality and long term reproducibility.

Plasma-polymerized styrene resist has been adopted for achieving a conformal film and a pin-hole free insulation layer which was evident from the impedance characterization results. This resist when paired with ion beam proximity lithography provides the patterning capability required to fabricate integrated conductor wiring on the surface of fine optical fibers. The specially designed V-groove mask provides the desired high precision alignment of the fiber to the mask with minimal lateral shift. An advanced stencil mask technology was developed for fabricating four channel optrodes. The use of a unique fixture facilitates fabrication of higher number of probes simultaneously and seamlessly by merely being integrated with every tool in the fabrication process. Successful fabrication and *in vivo* testing of two and three-channel prototypes using V-

groove masks provides a proof-of-concept that promises the that multi-tier optrode assemblies could be efficiently manufactured and used to record from multiple neurons simultaneously. The signal to noise ratio exhibited by these optical recordings was about 7.2 for spike sorting and 3D source localization.

Impedance measurement studies consisted of different experiments where the integrity and reusability of the optrode was tested in different environments, including saline, agar gel and warm phosphate buffered saline (PBS). The results yielded evidence of excellent reliability of the optrodes even after repeated insertions in Agar gel. Moreover, by merely rinsing the probe in de-ionized water after 10-12 days of continuous immersion in saline and PBS, restored the impedance to its original value. This provides enough evidence to the fact that the insulation was solid and did not suffer from any leakage effects. In addition to the above individual measurements, the impedance was characterized statistically in order to identify variations and subtle "out of control" conditions, if any. Statistical process control studies indicated a stable process with minimal variation on a day-to-day as well as sample-by-sample basis.

6.2 – Future Work

This work features a very promising technology platform for fabricating multi-tier 4-channel optrodes with achievable reliability and desired impedance measures. The only thing that changes from one family of probes to the other is the mask technology. Masks are key to any successful probe manufacturing process. A conceptual design (Fig. 6-1) builds on v-groove technology where the micro machined fiber holder (top) is formed by two families of intersecting V-grooves anisotropically etched and the lower groove is designed to expose a 60º field on the fiber. The mask is essentially a membrane with a

fine pattern of open stencil windows. Due to this, the strength of a template mask decreases with increasing pattern density. This imposes a limit on achieving a higher pattern density.

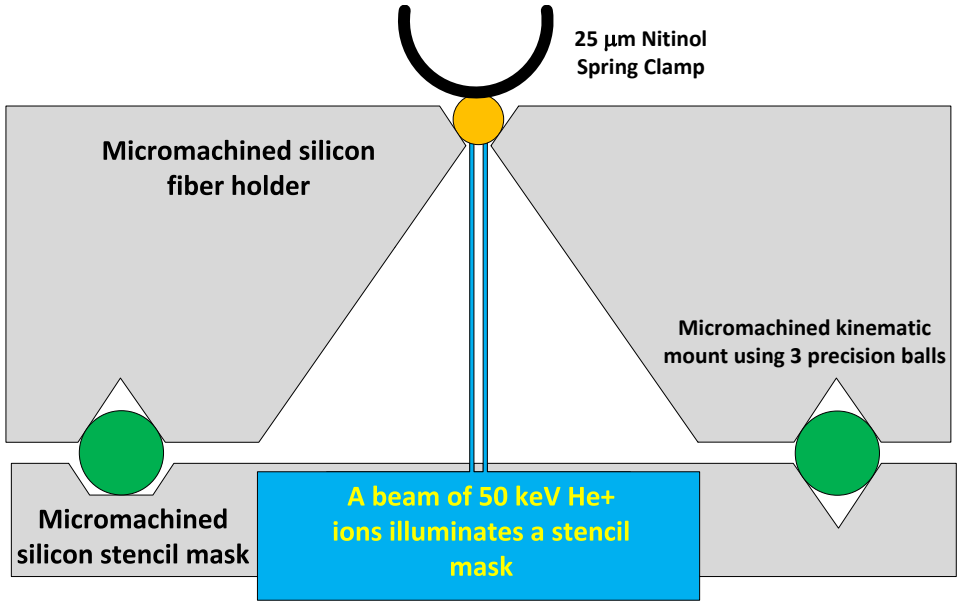

Fig. 6- 1: Conceptual drawing of fiber-holder and mask assembly.

To overcome this limitation, a lower density mask pattern can be moved over the target substrate and by superimposing the images from the individual exposures, a complex high density image can be formed. The approach[11] is to clamp the mask to the wafer setting the proximity gap with a suitable spacer, and to mechanically incline the mask/wafer stack relative to the beam as shown in Fig. 6-2 below.

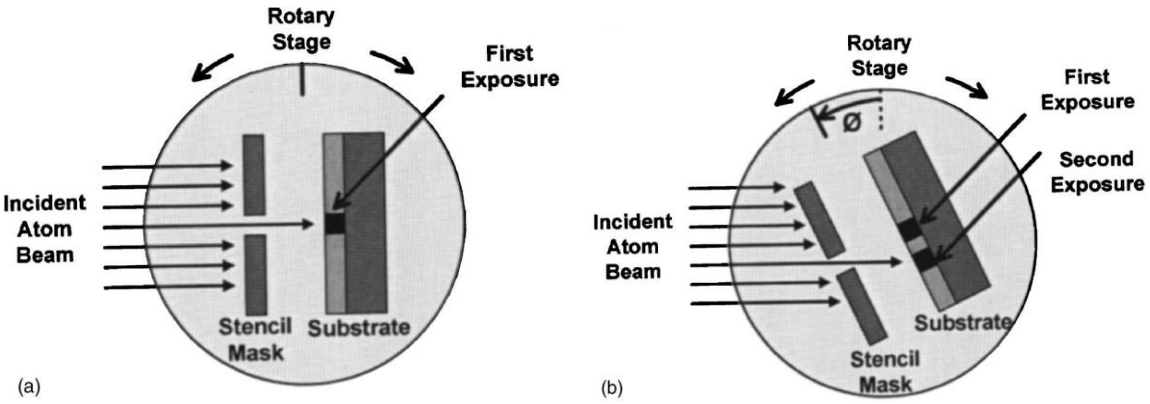

Fig. 6- 2: Concept of Nano stepping by inclining a clamped mask and substrate relative to the beam on a rotary stage.

In our case, a mask with free standing 2 μm wide bars along a 2″ long field would be incredibly floppy; the double exposure technique solves this problem. Here, instead of long bars the mask could be designed with shorter transmission windows as shown in the SAW mask picture (Fig. 6-3) which can be printed twice with a suitable offset along the rows to create continuous lines.

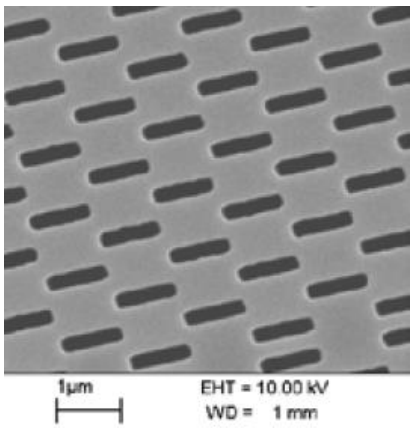

Fig. 6- 3: Silicon stencil SAW mask.

Thus, these probes can be designed (a) for sensing short and long range connections of optically stimulated neurons across cortical layers, (b) to develop low-cost high yield 2-

dimensional probe arrays to enable direct perturbation of a neural population code, map long-range connections causally, and (c) improve the insulation further by maintaining non static surroundings while probe handling.

With the ion milling technique preliminarily explored, it can replace the sputter etching process in the current process flow. The incorporation of ion beam etching will make way for an even faster manufacturing flow with additional process control.

References

[1] National Institute of Health: The BRAIN initiative (2014).

[2] B. Blause, Blausen Gallery 2014, *Journal of Medicine*, **1**(2) (2014).

[3] J. W. Papez, A Proposed Mechanism of Emotion, *Arch Neurol Pcychiatry*, **38**(4), 724–743 (1937).

[4] H. Klüver, P. Bucy, Preliminary Analysis of Functioning of the Temporal Lobes in Monkeys, *Arch. Neurol. Psychiatry*, **42**(6), 979–1000 (1939).

[5] P. D. MacLean, The Limbic System ("Visceral Brain") and Emotional Behavior, *Arch Neurol. Psychiatry*, **73**(2), 130–134 (1955).

[6] K. Deisseroth, Optogenetics, *Nature Methods*, **8**(1), 26–29 (2011).

[7] K. Deisseroth, Controlling the Brain With Light, *Scientific American*, (2010).

[8] M. A. Lebedev, M. A. Nicolelis, Brain-Machine Interfaces: Past, Present and Future, *Trends in Neuroscience*, **29**, 536–546 (2006).

[9] J.P. Donoghue, Connecting Cortex to Machine: Recent Advances in Brain Interfaces, *Nature Neuroscience*, **5**, 1085–1088 (2002).

[10] F. Mechler, J. Victor, I. Ohiorhenuan, A. Schmid, Q. Hu, Three-Dimensional

Localization of Neurons in Cortical Neural Recordings, *Journal of Neurophysiology*, **106**(2), 828 – 848 (2011).

[11] F. Mechler, J. Victor, Dipole Characterization of Single Neurons from their Extracellular Action Potentials, *Journal of Computational Neuroscience,* **32**(1), 73 – 100 (2012).

[12] A. Prasad, J. Sanchez, Quantifying Long-Term Microelectrode Array Functionality using Chronic in Vivo Impedance Testing, *Journal of Neural Engineering,* **9**(2), 026028 (2012).

[13] J. Yang, D. C. Martin, Microporous Conducting Polymers on Neural Microelectrode Arrays: I Electrochemical Deposition, *Sensors and Actuators B,* **101,** 133 – 142 (2004).

[14] J. Yang, D. C. Martin, Microporous Conducting Polymers on Neural Microelectrode Arrays: II Physical Characterization, *Sensors and Actuators A,* **113**, 204 – 211 (2004).

[15] X. Cui, J. F. Hetke, J. A. Wiler, D. J. Anderson, D. C. Martin, Electrochemical Deposition and Characterization of Conducting Polymer Polypyrrole/PSS on Multichannel Neural Probes, *Sensors and Actuators A,* **93**, 8 – 18 (2001).

[16] J-F. Huang, I-W. Sun, Fabrication and Surface Functionalization of Nanoporous Gold by Electrochemical Alloying-Dealloying of Au-Zn in an Ionic Liquid, and the Self-Assembly of L-Cysteine Monolayers, *Advanced Functional Materials,* **15**, 989 – 994 (2005).

[17] Z. Zhang, Y. Wang, Z. Qi, C. Somsen, X. Wang, C. Zhao Fabrication and Characterization of Nanoporous Gold Composites Through Chemical Dealloying of Two Phase Al-Au Alloys, *Journal of Material Chemistry,* **19**, 6042 – 6050 (2009).

[18] A. Prasad, Q-S. Xue, R. Dieme, V. Sankar, R. C. Mayrand, T. Nishida, W-J. Streit, J. C. Sanchez, Abiotic-Biotic Characterization of Pt/Ir Microelectrode Arrays in Chronic Implants, *Frontiers in Neuroengineering*, **7**(2), 1 – 15 (2014).

[19] A. Prasad, Q-S. Xue, V. Sankar, T. Nishida, T. Shaw, W-J. Streit, J. C. Sanchez Comprehensive Characterization and Failure Modes of Tungsten Microwire Arrays in Chronic Neural Implants, *Journal of Neural Engineering*, **9**(5), 056015 (2012).

[20] E. Kandel, J. Schwartz, T. Jessell, Principles of Neural Science, *Mc-Graw Hill New York* (2000).

[21] P. B. Cummings, *Pearson Education Inc* (2009).

[22] H. J. Curtis, K. S. Cole, Membrane Resting and Action Potentials from the Squid Giant Axon, *Journal of Cellular and Comparative Physiology*, **19**, 135 – 144 (1942).

[23] A. L. Hodgkin, B. Katz, The Effect of Sodium Ions on the Electrical Activity of the Giant Axon of the Squid (1949).

[24] A. L. Hodgkin, A. F. Huxley, A Quantitative Description of Membrane Current and its Application to Conduction and Excitation in Nerve, *The Journal of Physiology*, **117**(4), 500 – 544 (1952).

[25] E. T. McAdams, A. Lackermeier, J. A. McLaughlin, D. Macken, The Linear and Non-Linear Electrical Properties of the Electrode-Electrolyte Interface, *Biosensors and Bioelectronics*, **10**, 67 – 74 (1995).

[26] L. Galvani, De Viribus Electricitatis In Motu Musculari Commentarius, *Bon. Sci. Art. Inst. Acad. Comm*, **7**, 363–418 (1791).

[27] W. Rall, Electrophysiology of a Dendritic Neuron Model, *Biophys J*, **2**(2), 145-167 (1962).

[28] I. Cohen, R. Miles, Contributions of Intrinsic and Synaptic Activities to the Generation of Neuronal Discharges in In Vitro Hippocampus, *Journal of Physiology*, **524**(2), 485-502 (2000).

[29] D. A. Henze, Z. Borhegyi, J. Csicsvari, A. Mamiya, K. D. Harris, G. Buzsáki Intracellular Features Predicted by Extracellular Recordings in the Hippocampus In Vivo, *Journal of Neurophysiology*, **84**(1), 390-400 (2000).

[30] D. Oesterhelt, W. Stoeckenius, Rhodopsin-Like Protein from the Purple Membrane of Halobacterium Halobium, *Nature*, **233**, 149 – 152 (1971).

[31] A. Matsuno-Yagi, Y. Mukohata, Two Possible Roles of Bacteriorhodopsin; A Comparative Study of Strains of Halobacterium Halobium Differing in Pigmentation, *Biochemical and Biophysical Research Comm*, **78**(1), 237 – 43 (1977).

[32] D. B. Bivin, W. Stoeckenius, Photoactive Retinal Pigments in Haloalkaliphilic Bacteria, *J Gen Microbiol*, **132**(8), 2167-2177 (1986).

[33] G. Nagel, D. Ollig, M. Fuhrmann, S. Kateriya, A. M. Musti, E. Bamberg, P. Hegemann, Channelrhodopsin-1: A Light-Gated Proton Channel in Green Algae. *Science*, **296**(5577), 2395 – 8 (2002).

[33] G. Buzsáki, E. Stark, A. Berényi, D. Khodagholy, D. R. Kipke, E. Yoon, K. D. Wise, Tools for Probing Local Circuits: High-Density Silicon Probes Combined with Optogenetics, *Neuron Primer*, **86**(1), 92 – 105 (2015).

[34] N. A. Blum, B. G. Carkhuff, H. K. Charles Jr., R. L. Edwards, R. A. Meyer, Multisite Microprobes for Neural Recordings, *IEEE Transactions on Biomedical Engineering*, **38**(1), 68-74 (1991).

[35] O. J. Prohaska, F. Olcaytug, P. Pfundner, H. Dragaun, Thin-Film Multiple Electrode Probes: Possibilities and Limitations, *IEEE Transactions on Biomedical Engineering*, *BME-***33**(2), 223-229 (1986).

[36] K. L. Drake, K. D. Wise, J. Farraye, D. J. Anderson, S. L. BeMent, Performance of Planar Multisite Microprobes in Recording Extracellular Single-Unit Intracortical Activity, *IEEE Transactions on Biomedical Engineering*, **35**, 719-732 (1988).

[37] H. Eichenbaum, M. Kuperstein, Extracellular Neural Recording with Multichannel Microelectrodes, *J. Electrophysiol.Tech,* **13**, 189-209 (1986).

[38] P. K. Campbell, K. E. Jones, R. J. Huber, K. W. Horch, R. A. Normann, A Silicon-Based, Three-Dimensional Neural Interface: Manufacturing Processes for an Intracortical Electrode Array, *IEEE Transactions on Biomedical Engineering,* **38**(8), 758-768 (1991).

[39] E.S. Boyden, F. Zhang, E. Bamberg, G. Nagel, K. Deisseroth, Millisecond-timescale, Genetically Targeted Optical Control of Neural Activity, *Nature Neuroscience,* **8**, 1263–1268 (2005).

[40] V. Gradinaru, K. R. Thompson, F. Zhang, M. Mogri, K. Kay, M. B. Schneider, K. Deisseroth, Targeting and Readout Strategies for Fast Optical Neural Control in Vitro and In Vivo, *J. Neurosci.*, **27**, 14231-14238 (2007).

[41] G. Purushothaman, R. Marion, K. Li, V. A. Casagrande, Gating and Control of Primary Visual Cortex by Pulvinar, *Nature Neuroscience*, **15**(6), 905-912 (2012).

[42] G. Purushothaman, B. B. Scott, D. Bradley, An Acute Method for Multielectrode Recording from the Interior of Sulci and Other Deep Brain Areas, *Journal of Neuroscience Methods*, **53**, 86-94 (2006).

[43] Thomas Recording, (accessed September 28, 2015), Optogenetics Equipment – Thomas Recording GmbH.

[44] F. Wu, E. Stark, M. Im, I-J. Cho, E-S. Yoon, G. Buzsáki, K. D. Wise, E. Yoon, An Implantable Neural Probe with Monolithically Integrated Dielectric Waveguide and Recording Electrodes for Optogenetics Applications, *J Neural Eng.*, **10**(5), 056012 (2013).

[45] T. -I. Kim, J. G. McCall, Y. H. Jung, X. Huang, E. R. Siuda, Y. Li, J. Song, Y. M. Song, H. A. Pao, R. -H. Kim, C. Lu, S. D. Lee, I. -S. Song, G. Shin, R. Al-Hasani, S. Kim, M. P. Tan, Y. Huang, F. G. Omenetto, J. A. Rogers, M. R. Bruchas, Injectable, Cellular-Scale Optoelectronics with Applications for Wireless Optogenetics, *Science*, **340**, 211-216 (2012).

[46] K. M. Scott, J. Du, H. A. Lester, S. C. Masmanidis, Variabiltiy of Acute Extracellular Action Potential Measurements with Multisite Silicon Probes, *J Neurosci Methods*, **211**(1), 22 – 30 (2012).

[47] H. Yasuda, M. Gazicki, Biomedical Applications of Plasma Polymerization and Plasma Treatment of Polymer Surfaces, *Biomaterials*, **3**(2), 68 – 77 (1982).

[48] H. K. Yasuda, Plasma Polymerization, *Academic Press – Publisher* (2012).

[49] B. Craver, A Spatially-Modulated, High Voltage Focused Ion Beam Implantation System, *University of Houston* (2004).

[50] Ji. Qing, Maskless, Resistless Ion Beam Lithography Processes, *University of California, Berkeley* (1998).

[51] M. Gheewala, Development of Flexible Neural Probes for Stimulation and Recording in the Central Nervous System, *University of Houston, Texas* (2013).

[52] A. Jackson, J. Zimmermann, Neural Interfaces for the Brain and Spinal Cord – Restoring Motor Function, *Nature Reviews Neurology* **8**, 690 – 699 (2012).

[53] A. Geddes, Historical Evolution of Circuits Models for the Electrode-Electrolyte Interface, *Annals of Biomedical Engineering*, **25**, 1 – 14 (1997).

[54] J. C. Williams, J. A. Hippensteel, J. Dilgen, W. Shain, D. Kipke, Complex Impedance Spectroscopy for Monitoring Tissue Responses to Inserted Neural Implants, *Journal of Neural Engineering*, **4**, 410 – 423 (2007).

[55] L. Nelson, Technical Aids, *Journal of Quality Technology*, **16**(4), 238 – 239 (1984).

[56] R. Deepthi, R. Bhargavi, K. Jagadeesh, M. S. Vijaya, Rheometric Studies on Agarose Gel – A Brain Mimic Material, *SASTech Journal*, **9**, 2 (2010).

[57] X. Zhao, K. Aoki, J. Chen, T. Nishiumi, Examination of the Guoy-Chapman Theory for Double Layer Capacitance in Deionized Latex Suspensions, *Royal Society of Chemistry*, **4**, 63171 (2014).

[58] L. R. Hochberg, D. Bacher, B. Jarosiewicz, M. Y. Masse, J. D. Simeral, J. Vogel, S. Haddadin, J. Liu, S. S. Cash, P. van der Smagt, J. P. Donoghue, Reach and Grasp by People with Tetraplegia using A Neurally Controlled Robotic Arm, *Nature*, **485**, 372-375 (2010).

[59] G. Buzsak, E. Stark, A. Berenyi, D. Khodagholy, D. R. Kipke, E. Yoon, K. D. Wise. Tools for Probing Local Circuits: High-Density Silicon Probes Combined with Optogenetics, *Neuron*, **86**, 92-15 (2010).

[60] P. R. Kennedy, a Long-Term Electrode That Records from Neurites Grown Onto Its Recording Surface, *J Neurosci Methods*, **29,** 181–93 (1989).

[61] P. R. Kennedy, S. S. Mirra, R. A. Bakay, The Cone Electrode: Ultrastructural Studies Following Long-Term Recording In Rat And Monkey Cortex. *Neuroscience Letters* **142**, 89–94 (1992).

[62] P. R. Kennedy, R. A. E. Bakay, Restoration of Neural Output from A Paralyzed Patient Using A Direct Brain Connection, *NeuroReport*, 9, 1707–11 (1998).

[63] P. R. Kennedy, R. A. E. Bakay, K. Adams, J. Goldthwaite, M. Moore, Direct Control of A Computer from the Human Central Nervous System, *IEEE Trans. Rehab. Eng.*, **8,** 198-202 (2000).

[64] P. R. Kennedy, Comparing Electrodes for Use As Cortical Control Signals: Tiny Tines, Tiny Wires Or Tiny Cones on Wires: Which Is Best? *The Biomedical Engineering Handbook*. *3rd ed. Joe Brazino*, pp. 32.1–32.14 (2006).

[65] P. R. Kennedy, Reliable Neural Interface: The First Quarter Century of the Neurotrophic Electrode, *Proceedings of the 34th Annual International Conference of the IEEE EMBS San Diego, California USA*, 28 August - 1 September, pp. 3332-3335 (2012).

[66] T. D. Y. Kozai, A. S. Jaquins-Gerstl, A. L. Vazquez, A. C. Michael, X. T. Cui, Brain Tissue Responses to Neural Implants Impact Signal Sensitivity and Intervention Strategies, *ACS Chem*. *Neurosci*., **6,** 48−67 (2014).

[67] A. Prasad, Q-S. Xue, R. Dieme, V. Sankar, R. C. Mayrand, T. Nishida, W. J. Streit , J. C. Sanchez, Frontiers in Neuroengineering, **7**, Article 2:1-15 (2014).